

1107
23047
p. 193

Investigation of Advanced Counterrotation Blade Configuration Concepts for High Speed Turboprop Systems

Task 8—Cooling Flow/Heat Transfer Analysis Final Report

E.J. Hall, D.A. Topp, N.J. Heidegger, and R.A. Delaney
Allison Engine Company
Indianapolis, Indiana

N95-11901

Unclass

G3/07 0023047

September 1994

Prepared for
Lewis Research Center
Under Contract NAS3-25270

(NASA-CR-195359) INVESTIGATION OF
ADVANCED COUNTERROTATION BLADE
CONFIGURATION CONCEPTS FOR HIGH
SPEED TURBOPROP SYSTEMS. TASK 8:
COOLING FLOW/HEAT TRANSFER ANALYSIS
Final Report, Feb. 1993 - Jun. 1994
(Allison Engine Co.) 193 p



National Aeronautics and
Space Administration



Preface

This report was prepared by Edward J. Hall, David A. Topp, Nathan J. Heidegger, and Robert A. Delaney of the Allison Engine Company, Indianapolis, IN. The work was performed under NASA Contract NAS3-25270 from February, 1993 to June, 1994. The grid generation, flow code theory, and programming modifications necessary for the analysis were performed by Edward J. Hall, David A. Topp, and Nathan J. Heidegger. The Allison Program Manager for this contract was Robert A. Delaney. The NASA Project Manager was Christopher J. Miller.

Acknowledgements

The authors would like to express their appreciation to the following people who contributed to this program:

Stacey Myers, Purdue University, for her assistance in mesh generation and preliminary solution development

Eugene F. Clemens, Allison, for his assistance in mesh generation

Dr. Andrea Arnone, University of Florence, for his assistance with the use of the codes *TRAF2D*, *JERRYC*, and *TOMC*

Dr. Christopher J. Miller, NASA Lewis Research Center, for his suggestions and critical review of the program

Dr. Ali Ameri, NASA Lewis Research Center, and Dr. Okey Kwon, Allison, for their helpful discussions concerning turbulence modeling

Dr. Forrest Ames, Allison, for his insight into the physics of turbulent film cooling

The members of the NASA Lewis Research Center GVIS Lab, for their assistance in producing the animations of the 3-D computational fluid dynamics solutions

Contents

1	SUMMARY	1
2	INTRODUCTION	3
2.1	Description of the Film Cooling Problem	3
2.2	Experimental Studies	4
2.3	Computational Studies	5
2.4	Objectives of the Present Study	5
3	ADPAC08 NAVIER-STOKES NUMERICAL ALGORITHM	9
3.1	Nondimensionalization	10
3.2	3-D Navier-Stokes Equations	10
3.3	Governing Equations for Cartesian Solution	11
3.4	Fluid Properties	14
3.5	Numerical Formulation	15
3.6	Boundary Conditions	22
3.6.1	Porous Surface Boundary Condition	25
3.7	Runge-Kutta Time Integration	27
3.8	Dissipation Function	30
3.9	Turbulence Model	32
3.10	Implicit Residual Smoothing	34
3.11	Multigrid Convergence Acceleration	37
3.12	Solution Procedure	39
4	MARK II VANE CASCADE 2-D HEAT TRANSFER CALCULATIONS	41
4.1	Mark II Vane Cascade Description	41
4.2	Mark II Vane Cascade Mesh Generation	42

4.3	Mark II Vane 2-D Heat Transfer Mesh Dependence Study . . .	43
4.4	Mark II Vane 2-D Heat Transfer Operating Point Study	62
5	C3X VANE CASCADE 2-D HEAT TRANSFER CALCULATIONS	77
5.1	C3X Vane Cascade Description	77
5.2	C3X Vane Cascade Mesh Generation	78
5.3	C3X Vane 2-D Heat Transfer Mesh Dependence Study	81
5.4	C3X Vane 2-D Heat Transfer Operating Point Study	92
6	C3X VANE CASCADE 3-D HEAT TRANSFER CALCULATIONS	113
6.1	C3X Vane Cascade Description	113
6.2	C3X Vane Cascade Geometry Model	115
6.3	C3X Vane Cascade 3-D Grid Philosophy	115
6.4	C3X Vane Cascade 3-D Grid Layout	116
6.5	C3X Vane Cascade 3-D Grid Generation	116
6.6	C3X Vane Cascade 3-D Uncooled Heat Transfer Predictions .	119
6.7	C3X Vane Cascade 3-D Film-Cooled Heat Transfer Predictions	119
6.8	C3X Vane Cascade Porous Surface Boundary Condition Heat Transfer Predictions	137
7	CONCLUSIONS	149
A	Mark II Vane Cascade Mesh Generation and <i>ADPAC08</i> Input File Listing	159
B	C3X Vane Cascade Mesh Generation and <i>ADPAC08</i> Input File Listing	169

List of Figures

3.1	<i>ADPAC08</i> Cartesian Coordinate System Reference	12
3.2	<i>ADPAC08</i> 2-D Single Block Mesh Structure Illustration	16
3.3	<i>ADPAC08</i> 2-D Two Block Mesh Structure Illustration	17
3.4	<i>ADPAC08</i> 2-D Multiple Block Mesh Structure Illustration	18
3.5	Three-dimensional finite volume cell	21
3.6	2-D Mesh Block Phantom Cell Representation	23
3.7	<i>ADPAC08</i> Contiguous Mesh Block Coupling Scheme	26
3.8	<i>ADPAC08</i> Porous Wall Boundary Condition Model Schematic	28
3.9	Multigrid Mesh Coarsening Strategy and Mesh Index Relation	38
3.10	Multigrid V Cycle Strategy	40
4.1	Mark II Vane Mesh Dependence Study Frozen Turbulence Model Strategy Convergence History Comparison	47
4.2	Mark II Vane Mesh Dependence Study Frozen Turbulence Model Strategy Airfoil Surface Heat Transfer Coefficient Distribution Comparison	48
4.3	Mark II Vane Cascade Mesh Dependence Study - Mesh #1 (145x25) Mesh System and Predicted Mach Number Contours	49
4.4	Mark II Vane Cascade Mesh Dependence Study - Mesh #2 (193x33) Mesh System and Predicted Mach Number Contours	50
4.5	Mark II Vane Cascade Mesh Dependence Study - Mesh #3 (241x41) Mesh System and Predicted Mach Number Contours	51
4.6	Mark II Vane Cascade Mesh Dependence Study - Mesh #4 (385x49) Mesh System and Predicted Mach Number Contours	52
4.7	Mark II Vane Cascade Mesh Dependence Study - Mesh #5 (385x65) Mesh System and Predicted Mach Number Contours	53

4.8	Mark II Vane Cascade Mesh Dependence Study - Comparison of Predicted (Laminar Flow) and Experimental Airfoil Surface Static Pressure Ratio Distributions.	55
4.9	Mark II Vane Cascade Mesh Dependence Study - Comparison of Predicted (Laminar Flow) and Experimental Airfoil Surface Heat Transfer Coefficient Distributions.	56
4.10	Mark II Vane Cascade Mesh Dependence Study - Comparison of Predicted (Laminar Flow) Near Airfoil Surface Mesh y^+ Values.	57
4.11	Mark II Vane Cascade Mesh Dependence Study - Comparison of Predicted (Fully Turbulent Flow) and Experimental Airfoil Surface Static Pressure Ratio Distributions.	58
4.12	Mark II Vane Cascade Mesh Dependence Study - Comparison of Predicted (Fully Turbulent Flow) and Experimental Airfoil Surface Heat Transfer Coefficient Distributions.	59
4.13	Mark II Vane Cascade Mesh Dependence Study - Comparison of Predicted (Fully Turbulent Flow) Near Airfoil Surface Mesh y^+ Values.	60
4.14	Mark II Vane Cascade Mesh Dependence Study - Comparison of Predicted (Transitional Flow) and Experimental Airfoil Surface Static Pressure Ratio Distributions.	63
4.15	Mark II Vane Cascade Mesh Dependence Study - Comparison of Predicted (Transitional Flow) and Experimental Airfoil Surface Heat Transfer Coefficient Distributions.	64
4.16	Mark II Vane Cascade Mesh Dependence Study - Comparison of Predicted (Transitional Flow) Near Airfoil Surface Mesh y^+ Values.	65
4.17	Mark II Vane Cascade 193x33 2-D C-Grid Mesh System . . .	66
4.18	Mark II Vane Cascade Operating Point Study 385x49 2-D C-Grid Mesh System	67
4.19	Mark II Vane Cascade Operating Point Study 2-D C-Grid Mesh System Airfoil Surface y^+ Values	68
4.20	Comparison of Predicted and Experimental Airfoil Surface Static Pressure Ratio Distributions for Mark II Vane Cascade Operating Point Study ($M_2=0.89$).	70

4.21	Comparison of Predicted and Experimental Airfoil Surface Heat Transfer Coefficient Distributions for Mark II Vane Cascade Operating Point Study ($M_2=0.9$)	71
4.22	Comparison of Predicted and Experimental Airfoil Surface Static Pressure Ratio Distributions for Mark II Vane Cascade Operating Point Study ($M_2=1.05$)	72
4.23	Comparison of Predicted and Experimental Airfoil Surface Heat Transfer Coefficient Distributions for Mark II Vane Cascade Operating Point Study ($M_2=1.05$)	73
5.1	Comparison of Predicted and Experimental Airfoil Surface Static Pressure Distributions for the C3X Vane Cascade Illustrating Suction Surface Pressure Oscillations Due to Geometric Irregularity.	80
5.2	Comparison of Mesh Airfoil Surface Curvature for C3X Vane Cascade Illustrating Suction Surface Curvature Discontinuity.	82
5.3	Comparison of Predicted and Experimental Airfoil Surface Static Pressure Distributions for the C3X Vane Cascade Illustrating Improved Suction Surface Pressure Distribution Due to Smoothed Airfoil Surface Geometry.	83
5.4	Comparison of Mesh Airfoil Surface Curvature for C3X Vane Cascade Illustrating Improved Suction Surface Curvature Distribution.	84
5.5	C3X Vane Cascade Mesh Dependence Study - Mesh #1 (193x33) Mesh System and Predicted Mach Number Contours	86
5.6	C3X Vane Cascade Mesh Dependence Study - Mesh #2 (385x49) Mesh System and Predicted Mach Number Contours	87
5.7	C3X Vane Cascade Mesh Dependence Study - Mesh #3 (385x65) Mesh System and Predicted Mach Number Contours	88
5.8	C3X Vane Cascade Mesh Dependence Study - Mesh #4 (385x81) Mesh System and Predicted Mach Number Contours	89
5.9	C3X Vane Cascade Mesh Dependence Study - Mesh #5 (385x97) Mesh System and Predicted Mach Number Contours	90
5.10	C3X Vane Cascade Mesh Dependence Study Convergence History Comparison	93

5.11	C3X Vane Cascade Mesh Dependence Study - Comparison of Predicted (Transitional Flow) and Experimental Airfoil Surface Static Pressure Ratio Distributions.	94
5.12	C3X Vane Cascade Mesh Dependence Study - Comparison of Predicted (Transitional Flow) and Experimental Airfoil Surface Heat Transfer Coefficient Distributions.	95
5.13	C3X Vane Cascade Mesh Dependence Study - Comparison of Predicted (Transitional Flow) Near Airfoil Surface Mesh y^+ Values.	96
5.14	C3X Vane Cascade 193x33 2-D C-Grid Mesh System	97
5.15	C3X Vane Cascade Operating Point Study 497x65 2-D C-Grid Mesh System	98
5.16	C3X Vane Cascade Operating Point Study 2-D C-Grid Mesh System Airfoil Surface y^+ Values	99
5.17	C3X Vane Cascade Operating Point Study Convergence History Comparison	101
5.18	Comparison of Predicted and Experimental Airfoil Surface Static Pressure Ratio Distributions for C3X Vane Cascade Operating Point Study (Run #4400, $M_2=0.9$, $Re_2=2,000,000$) . .	102
5.19	Comparison of Predicted and Experimental Airfoil Surface Heat Transfer Coefficient Distributions for C3X Vane Cascade Operating Point Study (Run #4400, $M_2=0.9$, $Re_2=2,000,000$)	103
5.20	Comparison of Predicted and Experimental Airfoil Surface Static Pressure Ratio Distributions for C3X Vane Cascade Operating Point Study (Run #4500, $M_2=0.90$, $Re_2=2,500,000$) .	104
5.21	Comparison of Predicted and Experimental Airfoil Surface Heat Transfer Coefficient Distributions for C3X Vane Cascade Operating Point Study (Run #4500, $M_2=0.90$, $Re_2=2,500,000$)	105
5.22	Comparison of Predicted and Experimental Airfoil Surface Static Pressure Ratio Distributions for C3X Vane Cascade Operating Point Study (Run #5400, $M_2=1.05$, $Re_2=2,000,000$) .	106
5.23	Comparison of Predicted and Experimental Airfoil Surface Heat Transfer Coefficient Distributions for C3X Vane Cascade Operating Point Study (Run #5400, $M_2=1.05$, $Re_2=2,000,000$)	107
5.24	Comparison of Predicted and Experimental Airfoil Surface Static Pressure Ratio Distributions for C3X Vane Cascade Operating Point Study (Run #5500, $M_2=1.05$, $Re_2=2,500,000$) .	108

5.25	Comparison of Predicted and Experimental Airfoil Surface Heat Transfer Coefficient Distributions for C3X Vane Cascade Operating Point Study (Run #5500, $M_2=1.05$, $Re_2=2,500,000$)	109
6.1	C3X Vane With Film Cooling Holes.	114
6.2	Layout of C-grid with point assignment of film cooling holes.	117
6.3	Blade surface grid around film cooling holes.	118
6.4	Leading edge close-up of reduced 3-D mesh system for C3X turbine vane illustrating coolant hole mesh systems	121
6.5	Predicted near leading edge airfoil surface shear flow pattern for Run # 4415 of the C3X turbine vane cascade	124
6.6	Predicted Coolant Flow Particle Traces and Near Airfoil Surface Temperature Contours for Run # 4415 of the C3X turbine vane cascade	125
6.7	Predicted Coolant Flow Particle Traces and Near Airfoil Surface Temperature Contours for Run # 4435 of the C3X turbine vane cascade	126
6.8	Cooling Flow Effectiveness Degradation and Coolant Jet Lift-Off Due to Coolant Jet Secondary Flow and Hot Gas Entrainment	127
6.9	Predicted Chordwise Near Airfoil Surface Total Temperature Contours for Run # 4415 of the C3X Turbine Vane Cascade Illustrating Coolant Jet Lift-Off	128
6.10	Comparison of Predicted and Experimental Airfoil Surface Static Pressure Ratio Distributions for Run # 4415 of the C3X Turbine Vane Cascade on the Reduced Mesh (249x33x33 Airfoil Mesh)	130
6.11	Comparison of Predicted and Experimental Airfoil Surface Heat Transfer Coefficient Distributions for Run # 4415 of the C3X Turbine Vane Cascade on the Reduced Mesh (249x33x33 Airfoil Mesh)	131
6.12	Comparison of Predicted and Experimental Airfoil Surface Static Pressure Ratio Distributions for Run # 4415 of the C3X Turbine Vane Cascade on the Fine Mesh (497x65x65 Airfoil Mesh)	132

6.13	Comparison of Predicted and Experimental Airfoil Surface Heat Transfer Coefficient Distributions for Run # 4415 of the C3X Turbine Vane Cascade on the Fine Mesh (497x65x65 Airfoil Mesh)	133
6.14	Comparison of Predicted and Experimental Airfoil Surface Static Pressure Ratio Distributions for Run # 4435 of the C3X Turbine Vane Cascade on the Reduced Mesh (249x33x33 Airfoil Mesh)	134
6.15	Comparison of Predicted and Experimental Airfoil Surface Heat Transfer Coefficient Distributions for Run # 4435 of the C3X Turbine Vane Cascade on the Reduced Mesh (249x33x33 Airfoil Mesh)	135
6.16	Predicted near leading edge airfoil surface shear flow pattern for Run # 4417 of the C3X turbine vane cascade	136
6.17	Predicted Coolant Flow Particle Traces and Near Airfoil Surface Temperature Contours for Run # 4417 of the C3X turbine vane cascade	138
6.18	Predicted Coolant Flow Particle Traces and Near Airfoil Surface Temperature Contours for Run # 4437 of the C3X turbine vane cascade	139
6.19	Comparison of Predicted and Experimental Airfoil Surface Static Pressure Ratio Distributions for Run # 4417 of the C3X Turbine Vane Cascade on the Reduced Mesh (249x33x33 Airfoil Mesh)	140
6.20	Comparison of Predicted and Experimental Airfoil Surface Heat Transfer Coefficient Distributions for Run # 4417 of the C3X Turbine Vane Cascade on the Reduced Mesh (249x33x33 Airfoil Mesh)	141
6.21	Comparison of Predicted and Experimental Airfoil Surface Heat Transfer Coefficient Distributions for Run # 4417 of the C3X Turbine Vane Cascade on the Fine Mesh (497x65x65 Airfoil Mesh)	142
6.22	Comparison of Predicted and Experimental Airfoil Surface Static Pressure Ratio Distributions for Run # 4437 of the C3X Turbine Vane Cascade on the Reduced Mesh (249x33x33 Airfoil Mesh)	143

6.23	Comparison of Predicted and Experimental Airfoil Surface Heat Transfer Coefficient Distributions for Run # 4437 of the C3X Turbine Vane Cascade on the Reduced Mesh (249x33x33 Airfoil Mesh)	144
6.24	Predicted Mach Contours and Near Leading Edge Velocity Vectors for Porous Boundary Condition Analysis of Run # 4415 of the C3X Turbine Vane Cascade	146
6.25	Comparison of Predicted and Experimental Airfoil Surface Heat Transfer Coefficient Distributions for Run # 4415 of the C3X Turbine Vane Cascade Illustrating the Porous Surface Boundary Condition Model	147

List of Tables

4.1	Mark II Vane Cascade Design Parameters	42
4.2	Mark II Vane Cascade Mesh Dependence Study Mesh Parameters	46
4.3	Mark II Vane Cascade Calculation Operating Point Description	69
5.1	C3X Vane Cascade Design Parameters	78
5.2	C3X Vane Cascade Mesh Dependence Study Mesh Parameters)	91
5.3	C3X Vane Cascade Calculation Operating Point Description .	100

NOTATION

A list of the symbols used throughout this document and their definitions is provided below for convenience.

Roman Symbols

- c_p . . . gas specific heat at constant pressure
- c_v . . . gas specific heat at constant volume
- e . . . total internal energy
- i . . . first grid index of numerical solution
- j . . . second grid index of numerical solution
- k . . . third grid index of numerical solution or thermal conductivity
- n . . . rotational speed (revolutions per second) or time step level
- r . . . radius or radial coordinate
- t . . . time
- u_x . . . velocity in the Cartesian x direction

u_y ... velocity in the Cartesian y direction
 u_z ... velocity in the Cartesian z direction
 x ... Cartesian coordinate system coordinate
 y ... Cartesian coordinate system coordinate
 z ... Cartesian coordinate system coordinate
ADPAC08 ... Advanced Ducted Propfan Analysis Code Version 08
ADPOST ... ADPAC post processing program
ASCII ... American Standard Code for Information Interchange
CFL ... Courant-Freidrichs-Lewy number ($\Delta t / \Delta t_{max,stable}$)
CHGRIDV2 ... Ducted propfan grid generation code
 D ... reference length
 F ... i coordinate direction flux vector
 G ... j coordinate direction flux vector
GRIDGEN ... Multiple block general purpose mesh generation system
 H ... k coordinate direction flux vector
 J ... advance ratio ($J = U/nD$)
JERRYC ... TRAF2D Airfoil Cascade C-Mesh Generation Program
 M ... Mach number
 N ... Number of blades
 Q ... vector of conserved variables
 R ... gas constant or residual or maximum radius
 Re ... Reynolds Number
 Pr ... gas Prandtl Number
SDBLIB ... Scientific DataBase Library (binary file I/O routines)
 T ... Temperature
TOMC ... TRAF2D Airfoil Cascade C-Mesh Generation Program
 U ... Freestream velocity (units of length/time)
 V ... volume

Greek Symbols

γ ... specific heat ratio
 Δ ... calculation increment
 ρ ... density
 μ ... coefficient of viscosity
 τ ... coefficient of viscosity

Subscripts

- []₁ ... inlet value
- []₂ ... exit value
- []_{coarse} ... coarse mesh value
- []_{fine} ... fine mesh value
- []_{freestream} ... freestream value
- []_{i,j,k} ... grid point index of variable
- []_{max} ... maximum value
- []_{min} ... minimum value
- []_{nearwall} ... near wall value
- []_{non-dimensional} ... non-dimensional value
- []_{ref} ... reference value
- []_{stable} ... value implied by linear stability
- []_{total} ... total (stagnation) value
- []_{wall} ... value at the wall

Superscripts

- []⁺ ... Turbulent velocity profile coordinate
- []ⁿ ... Time step index

This Page Intentionally Left Blank

Chapter 1

SUMMARY

The overall objective of this study was to examine the aerodynamics and heat transfer characteristics of discrete site film-cooled turbine airfoils. The specific objective was to attempt to predict the three-dimensional flow about the C3X turbine vane cascade with a leading edge showerhead film-cooling arrangement. The motivation behind this work was to validate and assess the accuracy of present 3-D Navier-Stokes predictions for realistic film-cooled airfoil heat transfer predictions through comparisons with experimental data.

Several 2-D calculations were initially performed for both the Mark II and C3X turbine cascade geometries to verify the accuracy of the analysis for turbine airfoil heat transfer predictions in the absence of film-cooling. Three-dimensional calculations were performed for the C3X airfoil with film-cooling using a Cartesian coordinate system and taking advantage of the spanwise periodicity of the C3X geometry. Coolant flow was introduced into the blade passage through the use of separate mesh systems and transpiration/injection boundary conditions. The grid generation for the C3X cascade involved modeling the film-cooling holes as discrete objects in a 3-D mesh. Calculations were performed for the C3X at multiple operating points, both with and without cooling holes activated. The film-cooling flow was modeled both as injection at discrete holes, and as a uniform injection porous blade surface. Predicted results were compared with both experimental data and boundary layer code predictions.

Chapter 2

INTRODUCTION

2.1 Description of the Film Cooling Problem

Trends in thermodynamic design of gas turbine engines has traditionally led to higher and higher turbine inlet temperatures to improve overall thermodynamic efficiency. The result of this tendency is that turbine airfoils now often operate in an environment where the temperature of the primary gas flow exceeds the melting point of the surrounding metal. In order to provide adequate safety margins and to increase material life, complex airfoil cooling strategies are employed to isolate the airfoils and endwalls from the hot gas. A common technique to accomplish this goal is the use of film-cooling, wherein a layer of relatively cool gas is injected near the metal surfaces to provide a buffer layer between the hot gas and the protected surfaces. As operational temperature levels rise in modern gas turbine engines, the importance of accurately controlling turbine cooling flows presents one of the more difficult engineering challenges in the overall turbomachinery design process.

Turbine airfoil blade row flows are characterized by large temperature gradients, Mach numbers ranging from low subsonic (< 0.15) to the transonic range (> 1.0), and high levels of freestream turbulence with strong, small scale interactions between surface boundary layer convective flows, diffusive transport, and turbulent shear transport. Aerodynamic and thermal design techniques currently available to turbine airfoil designers have deficiencies which do not permit *a priori* designs which meet desired design

goals without expensive experimental development iterations. As such, the airfoil/coolant flow injection design (hole size, placement, shaping, etc) is often based on experience and/or empirical databases. Increased utilization of computational fluid dynamics (CFD) techniques in the design process for turbomachinery airfoils and flowpaths has naturally led to the use of these tools for predicting airfoil surface heat transfer and film cooling effectiveness. Unfortunately, our lack of comprehensive turbulence models capable of accurately predicting heat transfer in high Reynolds number turbulent flows has prevented widespread acceptance of CFD techniques in the heat transfer design arena. The use of CFD tools for predicting details of the primary gas path/coolant flow interaction can still be very useful for determining trends which might give the designer a better understanding of the problem, and ultimately lead to improvements in the final design.

2.2 Experimental Studies

Numerous experimental studies exist containing data involving measurements for film-cooled heat transfer. Most experimental studies involve surface measurements of heat transfer in the vicinity of a film-cooling injection site. A review of film-cooling research prior to 1970 is given by Goldstein [4]. Numerous studies have been performed to examine the effects of hole geometry, boundary layer thickness, hole and row spacing, and coolant flow/primary flow gas property variations. The works of Goldstein et al. [5], Foster and Lempard [6], and Jubran and Brown [7] to name a few, are representative of this type of work.

Data specific to turbine film cooling problems were reported by Mehendale and Han [8], who investigated the effects of mainstream turbulence on the film cooling effectiveness and heat transfer coefficient for a turbine airfoil leading edge. A large volume of data is available in a series of studies which were performed on the C3X airfoil cascade [1],[2],[3]. Airfoil surface heat transfer data were determined from experiments at realistic engine flow conditions for a baseline (no film cooling) airfoil, a modified airfoil with a leading edge showerhead film cooling arrangement [1],[2], and a third airfoil with an additional downstream array of cooling holes [3].

2.3 Computational Studies

Numerous computational approaches for film-cooling applications exist based on the boundary layer equations. These methods are useful for rapid design analysis to describe global properties of the boundary layer, but fail to capture three-dimensional variations and may not work at all for large coolant blowing ratios.

Navier-Stokes predictions of film-cooling flows related to gas turbine engine flows have only recently become feasible, and are, therefore, few in number. Yang et al. [9] attempted to predict the C3X airfoil cascade flow with film cooling on a two-dimensional basis using a time-marching Navier-Stokes solution technique. Dorney and Davis [10] performed both 2-D and 3-D flow simulations of a simplified turbine stage in the presence of a combustor hot streak. Through parametric studies, they identified a film cooling scheme to combat the problem of pressure surface hot streak migration. Garg and Gaugler [11] predicted the flow through the C3X turbine vane cascade with film cooling using a 3-D Navier Stokes solution technique. In all of these studies, no attempt was made to discretize details of the cooling holes themselves; rather, the cooling holes were modeled using boundary conditions applied to the “nearest-neighbor” mesh points from a mesh generated based on airfoil shape considerations only.

Zhou et al. [12] performed a study of film cooling from rows of cooling holes on a flat plate using a 3-D Navier-Stokes modeling technique. In this case, the circular cooling holes were modeled as square holes in a traditional rectangular Cartesian mesh. Similar calculations for film cooling on a flat plate were given by Leylek and Zerkle [13]. In this case, the computational mesh modeled the actual geometry of the experimental rig test described by Pietrzyk [14] including discrete mesh representation of the cooling holes, feed flowpath, and coolant flow plenum.

2.4 Objectives of the Present Study

At present, there are two major problems prohibiting widespread use of 3-D Navier-Stokes prediction techniques for film-cooled turbine airfoil heat transfer analysis. The first problem is related to geometry. Tools simply do not exist to permit numerical analysts (much less turbine airfoil designers) to

conveniently assign hole patterns, and generate a satisfactory mesh complete with adequate resolution of the coolant holes on the airfoil surface for use in complex 3-D numerical analysis. It may be demonstrated through pained manipulation of cumbersome general grid generation tools that it is possible to generate a suitable mesh for a given configuration, but only after extensive manipulation. Unfortunately, should a modification to the design be required, the effort to regenerate the numerical mesh is often greater than the effort to set up, compute, and post-process the solution by an order of magnitude. This problem clearly demonstrates the need for a combined computer-aided design/mesh generation capability. In addition, the actual mesh requirements for the coolant flow/airfoil flow problem have not been adequately defined, and, as such, even if adequate mesh generation tools were available, the research required to define the minimum mesh requirements for such an analysis has not, to date, been performed. The second major obstacle is the lack of comprehensive, accurate turbulence modeling procedures for high Reynolds number, high freestream turbulence turbine airfoil flows with heat transfer. Several numerical procedures have been described using high order (2 equation) turbulence models to predict turbine airfoil flows with heat transfer ([18], for example) and in nearly every case, the turbulence model is observed to be deficient, whether it be in the prediction of near wall turbulent flow behavior, transition, or the failure to accurately capture the jet flow/wall bounded shear layer interaction.

The numerical study described in this report is an attempt to address the problems of mesh definition and resolution for the prediction of discrete site film-cooled turbine airfoils. No attempt is made to conjure up a turbulence model capable of reproducing a limited amount of experimental data. Instead, a simple, proven turbulence modeling scheme is employed, and the focus is shifted to examining the mesh requirements for detailed analysis of the general turbine airfoil film cooling problem. To this end, detailed Navier-Stokes predictions of a realistic turbine airfoil design with a showerhead film cooling scheme were performed with emphasis on examining the mesh generation difficulties and resolution requirements for the cooling holes, and examining details of the flow structure resulting from the coolant flow/primary flow interaction.

This study represents one of the first attempts at predicting fine scale details of the aerodynamic and heat transfer characteristics resulting from the primary gas flow/coolant flow interaction of realistic gas turbine en-

gine turbine airfoils. The approach in this paper was to develop an analysis which possesses all the capabilities necessary to accurately solve this complex problem short of the advanced turbulence modeling necessary to accurately predict the true *levels* of the turbine airfoil heat transfer problem. The analytical tool used in this analysis is a 3-D Navier-Stokes analysis code referred to as *ADPAC08*. In the first section which follows this introduction, the theoretical basis and numerical implementation of the *ADPAC08* code are described in detail. Next, a series of 2-D aerodynamic/heat transfer calculations are performed for two non-cooled planar cascades representative of turbine airfoil blade rows. These calculations serve to quantify the accuracy of the present analysis for heat transfer predictions, and several mesh studies are included to determine a minimum mesh requirement for the general turbine airfoil heat transfer analysis problem. Finally, a series of 3-D viscous flow calculations are performed for a planar turbine airfoil cascade employing a leading edge showerhead film cooling scheme.

Chapter 3

ADPAC08 NAVIER-STOKES NUMERICAL ALGORITHM

Aerodynamic/heat transfer predictions for the film-cooled turbine airfoils described in this study were obtained using the *ADPAC08* analysis. The *ADPAC08* code is a general purpose turbomachinery aerodynamic design analysis which has undergone extensive development, testing, and verification [30], [25], [22], [24]. There is also extensive documentation available for the *ADPAC08* program [26], [27], [28]. Briefly, the *ADPAC08* analysis utilizes a finite volume, explicit multigrid Runge-Kutta time-marching solution algorithm to solve a time-dependent form of the 3-D Reynolds-Averaged Navier-Stokes equations. A relatively standard Baldwin-Lomax [23] turbulence model was incorporated to compute the turbulent shear stresses. The code employs a multiple-blocked mesh discretization which provides extreme flexibility for analyzing complex geometries. The block gridding technique enables the coupling of complex, multiple-region domains with common grid interface boundaries through specialized boundary condition procedures. The *ADPAC08* analysis has been successfully utilized to predict both the steady state and time-dependent aerodynamic interactions occurring in modern multistage compressors and turbines.

In this chapter, the governing equations and computational model applied for this study in the *ADPAC08* are described. In some cases, additional capabilities are available in the *ADPAC08* program, and these are described further in References [22], [28]. The definitions of the pertinent variables used in this chapter may be found in the Nomenclature.

3.1 Nondimensionalization

To simplify the implementation of the numerical solution, all variables are nondimensionalized by reference values as follows:

$$\begin{aligned}
 z &= \frac{\tilde{z}}{L_{ref}}, & r &= \frac{\tilde{r}}{L_{ref}}, & v_x &= \frac{\tilde{v}_x}{v_{ref}}, & v_y &= \frac{\tilde{v}_y}{v_{ref}}, & v_z &= \frac{\tilde{v}_z}{v_{ref}} \\
 p &= \frac{\tilde{p}}{p_{ref}}, & \mu &= \frac{\tilde{\mu}}{\mu_{ref}}, & c_p &= \frac{\tilde{c}_p}{R_{ref}}, & c_v &= \frac{\tilde{c}_v}{R_{ref}}, & k &= \frac{\tilde{k}}{k_{ref}} \\
 T &= \frac{\tilde{T}}{T_{ref}}, & \rho &= \frac{\tilde{\rho}}{\rho_{ref}}, & & & & & &
 \end{aligned} \tag{3.1}$$

The reference quantities are defined as follows:

- L_{ref} is a constant user-defined length scale
- p_{ref} is normally the inlet total pressure (user-defined)
- ρ_{ref} is the freestream or inlet total density ($\rho_{ref} = p_{ref} / R_{ref} / T_{ref}$)
- a_{ref} is determined by $\sqrt{\gamma R_{ref} T_{ref}}$
- v_{ref} is determined from the freestream total acoustic velocity as $v_{ref} = \frac{a_{ref}}{\sqrt{\gamma}}$
- μ_{ref} is determined from the other factors as: $\mu_{ref} = \rho_{ref} v_{ref} L_{ref}$
- k_{ref} is the freestream thermal conductivity (extracted from user-defined parameters such as γ and Prandtl number)
- R_{ref} is the freestream gas constant (user-defined)
- T_{ref} is normally the inlet total temperature (user-defined)

3.2 3-D Navier-Stokes Equations

The *ADPAC08* numerical solution procedure is based on an integral representation of the strong conservation law form of the Navier-Stokes equations expressed in either a cylindrical or Cartesian coordinate system. User input determines which solution scheme is selected, and can be varied on a block by block basis. The Cartesian form of the equations are presented below

since all of the calculations performed in this study utilized the Cartesian solution scheme. Details of the corresponding cylindrical solution scheme are available in References [25], and [22]. The Euler equations may be derived as a subset of the Navier-Stokes equations by neglecting viscous dissipation and thermal conductivity terms (i.e. - μ and $k = 0$).

3.3 Governing Equations for Cartesian Solution

Integration of the differential form of the Navier-Stokes equations over a finite control volume yields the following set of equations:

$$\int \frac{\partial}{\partial t}(Q)dV + L_{inv}(Q) = L_{vis}(Q) \quad (3.2)$$

where:

$$L_{inv}(Q) = \int_{dA} [\bar{F}_{inv}dA_x + \bar{G}_{inv}dA_y + \bar{H}_{inv}dA_z] \quad (3.3)$$

and:

$$L_{vis}(Q) = \int_{dA} [\bar{F}_{vis}dA_x + \bar{G}_{vis}dA_y + \bar{H}_{vis}dA_z] \quad (3.4)$$

The inviscid (convective) and viscous (diffusive) flux contributions are expressed separately by the operators L_{inv} and L_{vis} , respectively.

The vector of dependent variables Q is defined as:

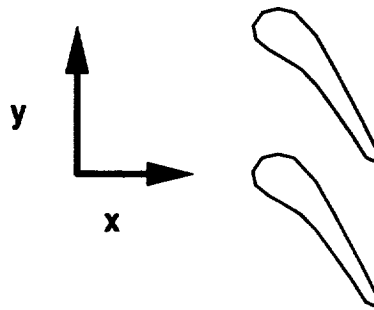
$$Q = \begin{bmatrix} \rho \\ \rho v_x \\ \rho v_y \\ \rho v_z \\ \rho e_t \end{bmatrix} \quad (3.5)$$

where the velocity components v_x , v_y , and v_z are the absolute velocity components in the x , y , and z coordinate directions, respectively (see e.g. - Fig. 3.1). The total internal energy is defined as:

$$e_t = \frac{p}{(\gamma - 1)\rho} + \frac{1}{2}(v_x^2 + v_y^2 + v_z^2) \quad (3.6)$$

ADPAC08 Cartesian Coordinate System Reference

2-D Turbine Vane Calculations



3-D Turbine Vane Calculations

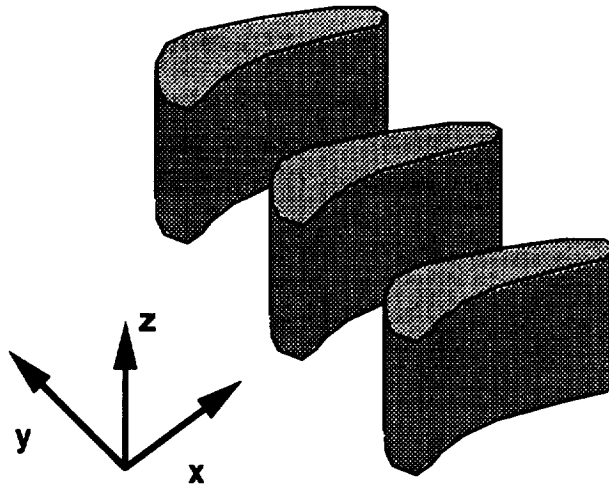


Figure 3.1: *ADPAC08* Cartesian Coordinate System Reference

The individual flux functions are defined as:

$$F_{inv} = \begin{bmatrix} \rho v_x \\ \rho v_x^2 + p \\ \rho v_x v_y \\ \rho v_x v_z \\ \rho v_x H \end{bmatrix}, \quad G_{inv} = \begin{bmatrix} \rho v_y \\ \rho v_x v_y \\ \rho v_y^2 + p \\ \rho v_y v_z \\ \rho v_y H \end{bmatrix}, \quad H_{inv} = \begin{bmatrix} \rho v_z \\ \rho v_x v_z \\ \rho v_y v_z \\ (\rho v_z^2 + p) \\ \rho v_z H \end{bmatrix} \quad (3.7)$$

$$F_{vis} = \begin{bmatrix} 0 \\ \tau_{xx} \\ \tau_{xy} \\ \tau_{xz} \\ q_x \end{bmatrix}, \quad G_{vis} = \begin{bmatrix} 0 \\ \tau_{yx} \\ \tau_{yy} \\ \tau_{yz} \\ q_y \end{bmatrix}, \quad H_{vis} = \begin{bmatrix} 0 \\ \tau_{zx} \\ \tau_{zy} \\ \tau_{zz} \\ q_z \end{bmatrix}, \quad (3.8)$$

$$\begin{aligned} \bar{F} &= F(\bar{Q}), & \bar{G} &= G(\bar{Q}), & \bar{H} &= H(\bar{Q}) \\ \bar{F}_v &= F_v(\bar{Q}), & \bar{G}_v &= G_v(\bar{Q}), & \bar{H}_v &= H_v(\bar{Q}) \end{aligned} \quad (3.9)$$

The total enthalpy, H , is related to the total energy by:

$$H = e_t + \frac{p}{\rho} \quad (3.10)$$

The viscous stress terms may be expressed as:

$$\tau_{xx} = 2\mu \left(\frac{\partial v_x}{\partial x} \right) + \lambda_v \nabla \cdot \vec{V}, \quad (3.11)$$

$$\tau_{xy} = \mu \left[\left(\frac{\partial v_y}{\partial x} \right) + \left(\frac{\partial v_x}{\partial y} \right) \right], \quad (3.12)$$

$$\tau_{xz} = 2\mu \left[\left(\frac{\partial v_y}{\partial z} \right) + \left(\frac{\partial v_z}{\partial x} \right) \right], \quad (3.13)$$

$$\tau_{yy} = 2\mu \left(\frac{\partial v_y}{\partial y} \right) + \lambda_v \nabla \cdot \vec{V} \quad (3.14)$$

$$\tau_{yz} = 2\mu \left[\left(\frac{\partial v_y}{\partial z} \right) + \left(\frac{\partial v_z}{\partial y} \right) \right], \quad (3.15)$$

$$\tau_{zz} = 2\mu \left(\frac{\partial v_z}{\partial z} \right) + \lambda_v \nabla \cdot \vec{V} \quad (3.16)$$

$$q_x = v_x \tau_{xx} + v_y \tau_{xy} + v_z \tau_{xz} + k \frac{\partial T}{\partial x} \quad (3.17)$$

$$q_y = v_x \tau_{yx} + v_y \tau_{yy} + v_z \tau_{yz} + k \frac{\partial T}{\partial y} \quad (3.18)$$

$$q_z = v_x \tau_{zx} + v_y \tau_{zy} + v_z \tau_{zz} + k \frac{\partial T}{\partial z} \quad (3.19)$$

where μ is the first coefficient of viscosity, λ_v is the second coefficient of viscosity, and:

$$\nabla \cdot \vec{V} = \frac{\partial v_x}{\partial x} + \frac{\partial v_y}{\partial y} + \frac{\partial v_z}{\partial z} \quad (3.20)$$

The remaining viscous stress terms are defined through the identities:

$$\tau_{yx} = \tau_{xy}, \quad (3.21)$$

$$\tau_{zy} = \tau_{yz}, \quad (3.22)$$

$$\tau_{zx} = \tau_{xz}, \quad (3.23)$$

Transition of the *ADPAC08* code from a cylindrical coordinate system solver to a Cartesian coordinate system solver was accomplished through the use of an input trigger variable. When activated, the trigger selects the appropriate calculations of cell areas, volumes, and fluxes to be consistent with the governing Cartesian equations. In addition, the cylindrical coordinate system source term is eliminated for Cartesian solutions. The modified *ADPAC08* code retains both the cylindrical and Cartesian coordinate solution capabilities.

The governing equations for the 2-D flow problems discussed in the following chapters may be similarly derived from the 3-D equations by eliminating the z-momentum equation and assuming that the z velocity, v_z is zero.

3.4 Fluid Properties

The working fluid is assumed to be air acting as a perfect gas, thus the ideal gas equation of state has been used. Fluid properties such as specific heats,

specific heat ratio, and Prandtl number are assumed to be constant. The fluid viscosity is derived from the Sutherland (see e.g. [35]) formula:

$$\mu = C_1 \frac{(T)^{\frac{3}{2}}}{T + C_2} \quad (3.24)$$

The so-called second coefficient of viscosity λ_v is fixed according to:

$$\lambda_v = -\frac{2}{3}\mu \quad (3.25)$$

The thermal conductivity is determined from the viscosity and the definition of the Prandtl number as:

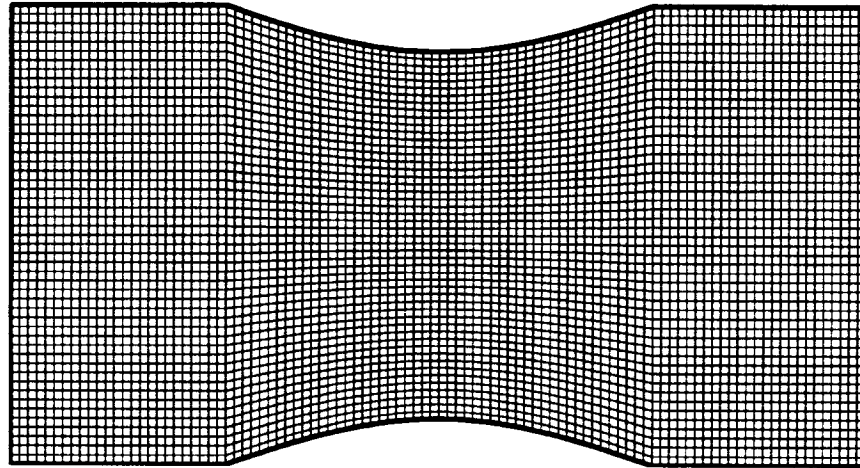
$$k = \frac{c_p \mu}{Pr} \quad (3.26)$$

3.5 Numerical Formulation

The discrete numerical solution is developed from the integral governing equations derived in the previous sections by employing a finite volume solution procedure. This procedure closely follows the basic scheme described by Jameson [37]. In order to appreciate and utilize the features of the *AD-PAC08* solution system, the concept of a multiple blocked grid system must be fully understood. It is expected that the reader possesses at least some understanding of the concepts of computational fluid dynamics (CFD), so the use of a numerical grid to discretize a flow domain should not be foreign. Many CFD analyses rely on a single structured ordering of grid points upon which the numerical solution is performed (the authors are aware of a growing number of unstructured grid solution techniques as well, but resist the temptation to mention them in this discussion). Multiple blocked grid systems are different only in that several structured grid systems are used in harmony to generate the numerical solution. The domain of interest is subdivided into one or more structured arrays of hexahedral cells. Each array of cells is referred to as a “block”, and the overall scheme is referred to as a multiple blocked mesh solver as a result of the ability to manage more than one block. This concept is illustrated graphically in two dimensions for the flow through a nozzle in Figures 3.2-3.4.

ADPAC-AOACR 2-D Single Block Mesh Structure Illustration

Physical Domain



Computational Domain

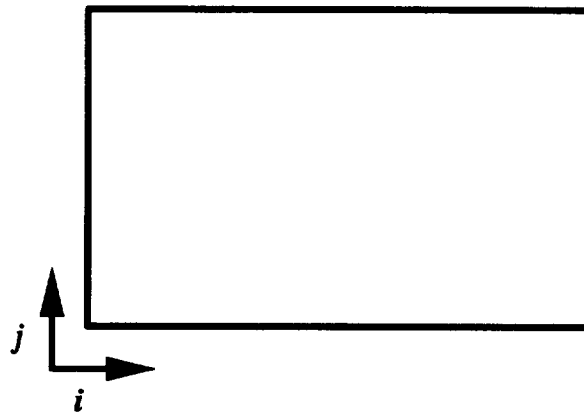


Figure 3.2: *ADPAC08* 2-D Single Block Mesh Structure Illustration

ADPAC-AOACR 2-D Two Block Mesh Structure Illustration

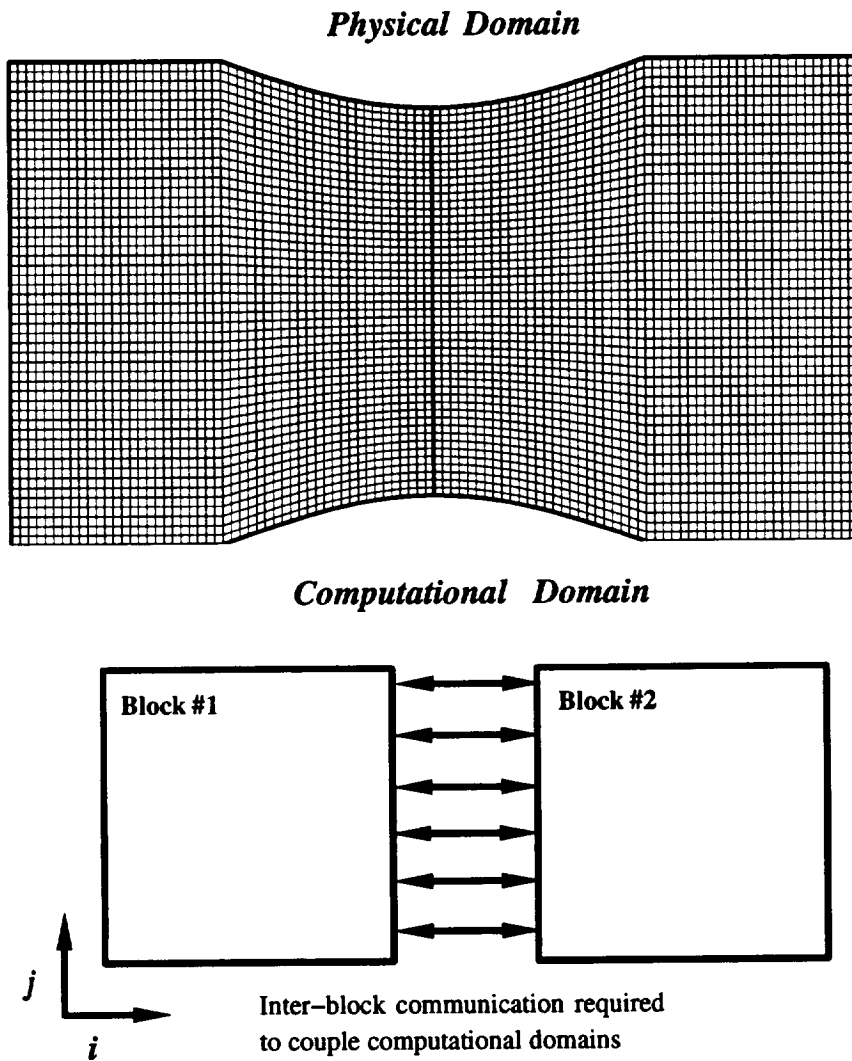
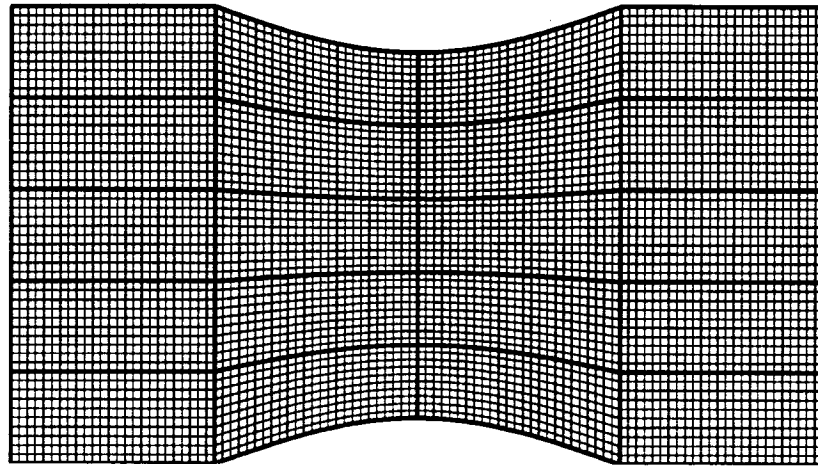


Figure 3.3: ADPAC08 2-D Two Block Mesh Structure Illustration

ADPAC-AOACR 2-D Multiple Block Mesh Structure Illustration
Physical Domain



Computational Domain

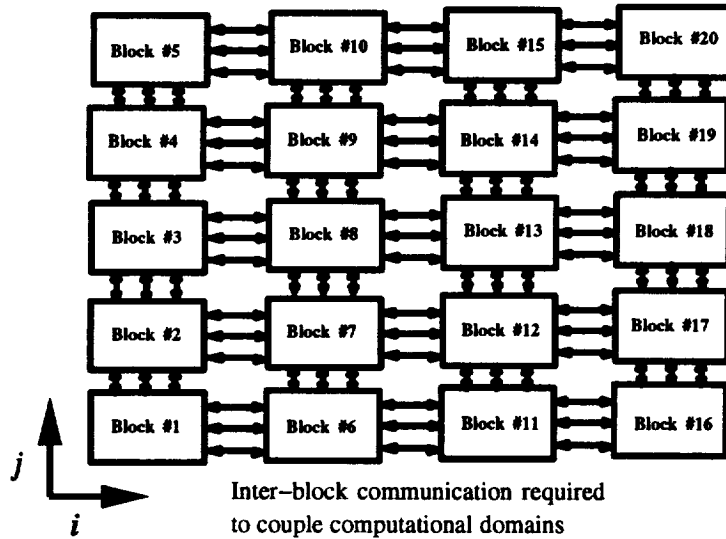


Figure 3.4: *ADPAC08* 2-D Multiple Block Mesh Structure Illustration

The grid system in Figure 3.2 employs a single structured ordering, resulting in a single computational space to contend with. The mesh system in Figure 3.3 is comprised of two, separate structured grid blocks, and consequently, the numerical solution consists of two unique computational domains. In theory, the nozzle flowpath could be subdivided into any number of domains employing structured grid blocks resulting in an identical number of computational domains to contend with, as shown in the 20 block decomposition illustrated in Figure 3.4. The complicating factor in this domain decomposition approach is that the numerical solution must provide a means for the isolated computational domains to communicate with each other in order to satisfy the conservation laws governing the desired aerodynamic solution. Hence, as the number of subdomains used to complete the aerodynamic solution grows larger, the number of inter-domain communication paths increases in a corresponding manner. (It should be noted that this domain decomposition/communication overhead relationship is also a key concept in parallel processing for large scale computations, and thus, the *ADPAC08* code appears to be a viable candidate for parallelization via the natural domain decomposition division afforded by the multiple-blocked grid data structure.) Clearly, it is often not possible to generate a single structured grid to encompass the domain of interest without sacrificing grid quality, and therefore, a multiple blocked grid system has significant advantages.

The *ADPAC08* code was developed to utilize the multiple blocked grid concept to full extent by permitting an arbitrary number of structured grid blocks with user specifiable communication paths between blocks. The inter-block communication paths are implemented as a series of boundary conditions on each block which, in some cases, communicate flow information from one block to another. The advantages of the multiple-block solution concept are exploited in the calculations presented in Chapter 4 as a means of treating complicated geometries with multiple blade rows of varying blade number, and to exploit computational enhancements such as multigrid.

The solution for each mesh block in a multiple-blocked grid is computed identically, and therefore the numerical approach is described for a single mesh block. In any given mesh block, the numerical grid is used to define a set of hexahedral cells, the vertices of which are defined by the eight surrounding mesh points. This construction is illustrated in Figure 3.5.

The cell face surface area normal vector components dA_x , dA_y , and dA_z

are calculated using the cross product of the diagonals defined by the four vertices of the given face, and the cell volume is determined by a procedure outlined by Hung and Kordulla [36] for generalized nonorthogonal cells. The integral relations expressed by the governing equations are determined for each cell by approximating the area-integrated convective and diffusive fluxes with a representative value along each cell face, and by approximating the volume-integrated terms with a representative cell volume weighted value. The discrete numerical approximation to the governing equation then becomes

$$\begin{aligned}
Vol \frac{Q_{i,j,k}^{n+1} - Q_{i,j,k}^n}{\Delta t} &= (F_{inv}(\bar{Q})_{i+1,j,k} - F_{inv}(\bar{Q})_{i,j,k}) \\
&+ G_{inv}(\bar{Q})_{i,j+1,k} - G_{inv}(\bar{Q})_{i,j,k} \\
&+ H_{inv}(\bar{Q})_{i,j,k+1} - H_{inv}(\bar{Q})_{i,j,k} \\
&+ F_{vis}(\bar{Q})_{i+1,j,k} - F_{vis}(\bar{Q})_{i,j,k} \\
&+ G_{vis}(\bar{Q})_{i,j+1,k} - G_{vis}(\bar{Q})_{i,j,k} \\
&+ H_{vis}(\bar{Q})_{i,j,k+1} - H_{vis}(\bar{Q})_{i,j,k} \\
&+ Vol K + D_{i,j,k}(\bar{Q})
\end{aligned} \tag{3.27}$$

Here, i, j, k represents the local cell indices in the structured cell array, Vol is the local cell volume, Δt is the calculation time interval, and $D_{i,j,k}$ is an artificial numerical dissipation function which is added to the governing equations to aid numerical stability, and to eliminate spurious numerical oscillations in the vicinity of flow discontinuities such as shock waves. Following the algorithm defined by Jameson [37], it is convenient to store the flow variables as a representative value for the interior of each cell, and thus the scheme is referred to as cell-centered. The discrete convective fluxes are constructed by using a representative value of the flow variables \bar{Q} which is determined by an algebraic average of the values of Q in the cells lying on either side of the local cell face. Viscous stress terms and thermal conduction terms are constructed by applying a generalized coordinate transformation to the governing equations as follows:

$$\xi = \xi(x, y, z), \quad \eta = \eta(x, y, z), \quad \zeta = \zeta(x, y, z) \tag{3.28}$$

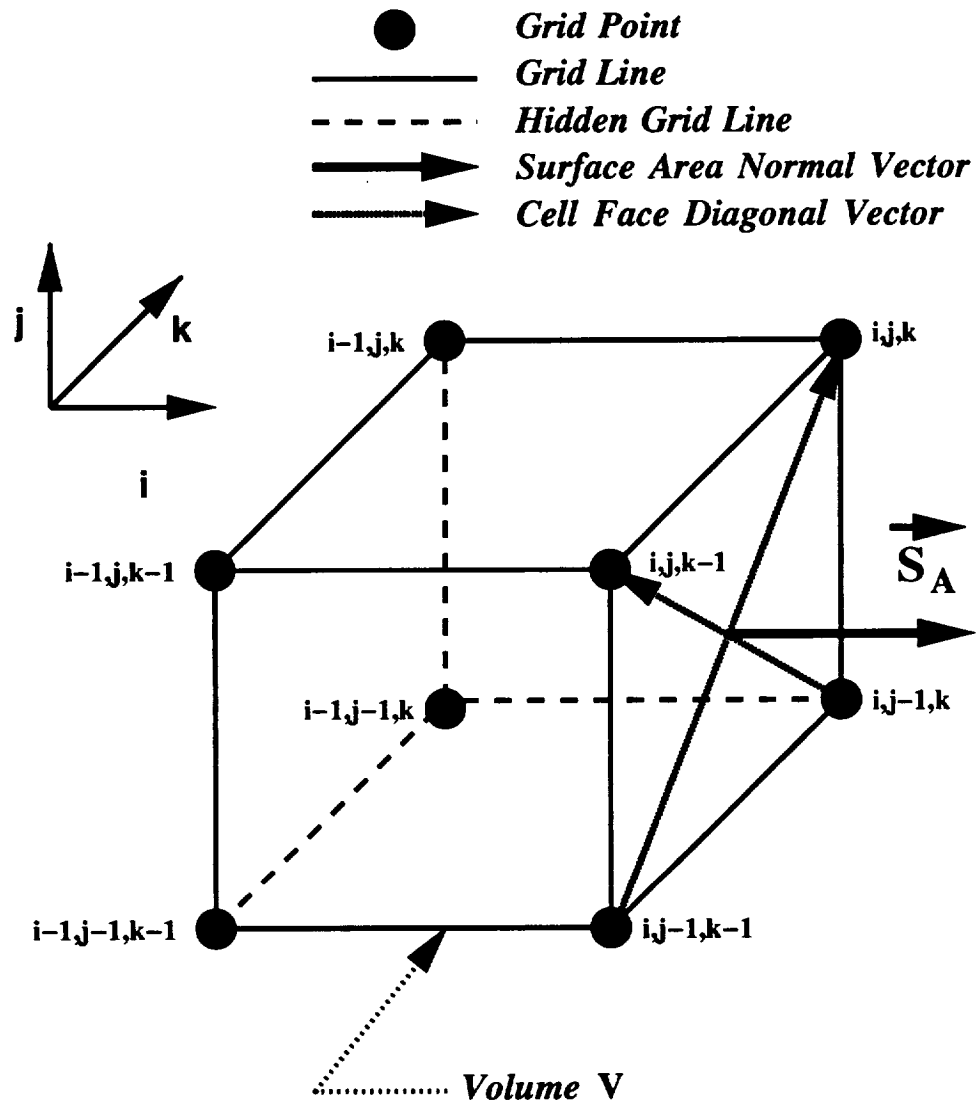


Figure 3.5: Three-dimensional finite volume cell

The chain rule may then be used to expand the various derivatives in the viscous stresses as:

$$\frac{\partial}{\partial x} = \frac{\partial \xi}{\partial x} \frac{\partial}{\partial \xi} + \frac{\partial \eta}{\partial x} \frac{\partial}{\partial \eta} + \frac{\partial \zeta}{\partial x} \frac{\partial}{\partial \zeta}, \quad (3.29)$$

$$\frac{\partial}{\partial y} = \frac{\partial \xi}{\partial y} \frac{\partial}{\partial \xi} + \frac{\partial \eta}{\partial y} \frac{\partial}{\partial \eta} + \frac{\partial \zeta}{\partial y} \frac{\partial}{\partial \zeta}, \quad (3.30)$$

$$\frac{\partial}{\partial z} = \frac{\partial \xi}{\partial z} \frac{\partial}{\partial \xi} + \frac{\partial \eta}{\partial z} \frac{\partial}{\partial \eta} + \frac{\partial \zeta}{\partial z} \frac{\partial}{\partial \zeta}, \quad (3.31)$$

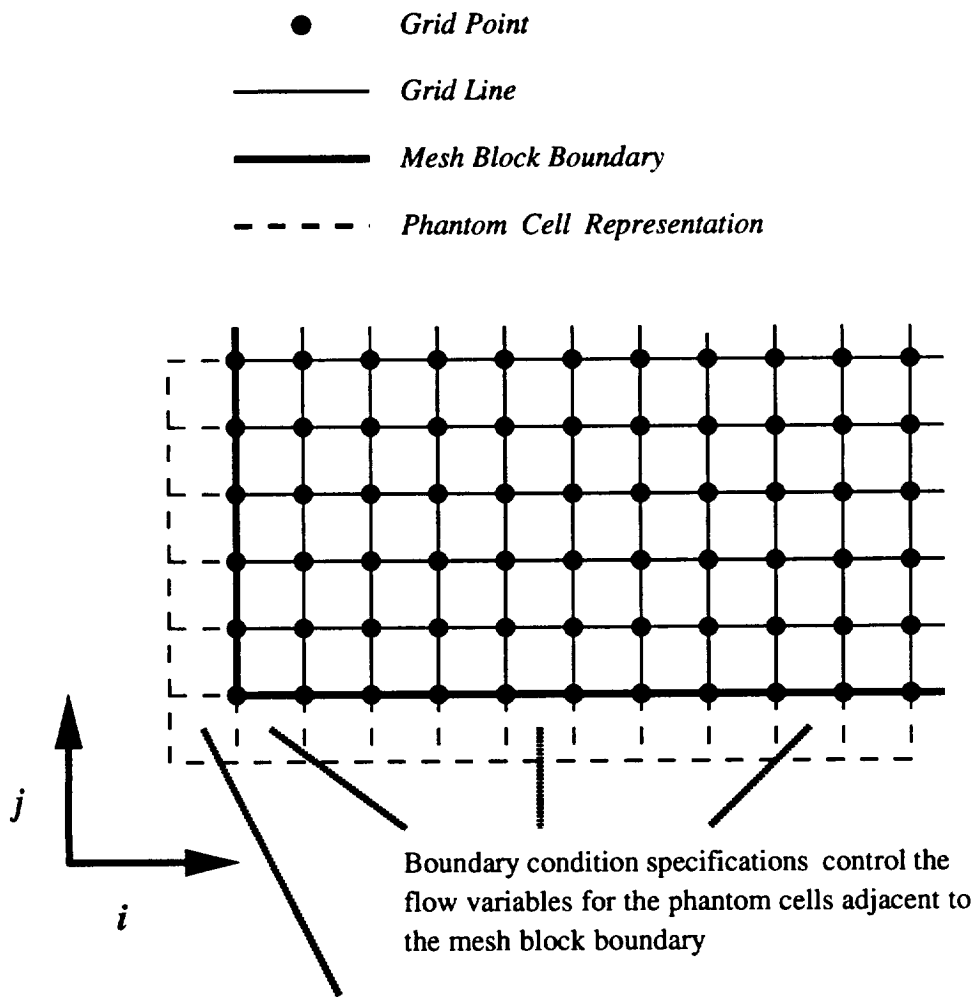
The transformed derivatives may now be easily calculated by differencing the variables in computational space (i corresponds to the ξ direction, j corresponds to the η direction, and k corresponds to the ζ direction); and utilizing the appropriate identities for the metric differences (see e.g. [35]).

3.6 Boundary Conditions

In this section, the various boundary conditions utilized in this study as part of the *ADPAC08* analysis are described. Before describing the individual boundary conditions, it may be useful to describe how the boundary conditions are imposed in the discrete numerical solution. Finite volume solution algorithms such as the *ADPAC08* program typically employ the concept of a phantom cell to impose boundary conditions on the external faces of a particular mesh block. This concept is illustrated graphically for a 2-D mesh representation in Figure 3.6.

A phantom cell is a fictitious neighboring cell located outside the extent of a mesh which is utilized in the application of boundary conditions on the outer boundaries of a mesh block. Since flow variables cannot be directly specified at a mesh surface in a finite volume solution (the flow variables are calculated and stored at cell centers), the boundary data specified in the phantom cells are utilized to control the flux condition at the cell faces of the outer boundary of the mesh block, and, in turn, satisfy a particular boundary condition. All *ADPAC08* boundary condition specifications provide data values for phantom cells to implement a particular mathematical boundary condition on the mesh. Another advantage of the phantom cell approach is

2-D Mesh Block Phantom Cell Representation



"Corner" phantom cells cannot be controlled through boundary conditions, but must be updated to accurately compute grid point averaged values

Figure 3.6: 2-D Mesh Block Phantom Cell Representation

that it permits unmodified application of the interior point scheme at near boundary cells.

Inflow and exit boundary conditions are applied numerically using characteristic theory. A one-dimensional isentropic system of equations is utilized to derive the following characteristic equations at an axial inflow/outflow boundary:

$$\frac{\partial C^-}{\partial t} - (v_x - a) \frac{\partial C^-}{\partial x} = 0, \quad (3.32)$$

$$\frac{\partial C^+}{\partial t} + (v_x + a) \frac{\partial C^+}{\partial x} = 0 \quad (3.33)$$

where:

$$C^- = v_x - \frac{2a}{\gamma - 1}, \quad C^+ = v_x + \frac{2a}{\gamma - 1} \quad (3.34)$$

For subsonic normal inflow, the upstream running invariant C^- is extrapolated to the inlet, and along with the equation of state, specified total pressure, total temperature, and flow angles the flow variables at the boundary may be determined. For turbomachinery based flow calculations, the flow angles are representative of the spanwise flow and the pitchwise (blade-to-blade) flow.

Outflow boundaries require a specification of the exit static pressure. In this case, the downstream running invariant C^+ is used to update the phantom cells at the exit boundary. Velocity components parallel to the cell face are extrapolated to the phantom cell from the neighboring interior cells.

It should be mentioned that all of the characteristic boundary schemes utilize a local rotated coordinate system which is normal to the bounding cell face.

All solid surfaces must satisfy the no slip boundary condition for viscous flows:

$$v_x = 0, \quad v_y = 0, \quad v_z = 0 \quad (3.35)$$

No convective flux through the boundary (an impermeable surface) is permitted. The phantom cell velocity components are thus constructed to ensure that the cell face average velocities used in the convective flux calculation are identically zero. The phantom cell pressure is simply extrapolated based on the boundary layer flow concept $dp/dn = 0$. The phantom cell density or temperature is imposed by assuming either an adiabatic surface $dT/dn = 0$

or a specified surface temperature, which suggests that the phantom cell temperature must be properly constructed to satisfy the appropriate average temperature along the surface.

For the multiple-block scheme, the solution is performed on a single grid block at a time. Special boundary conditions along block boundaries are therefore required to provide some transport of information between blocks. This transport may be accomplished through one of four types of procedures in the *ADPAC08* code. Each procedure applies to a different type of mesh construction and flow environment, and details of each approach are given in Reference [22]. For neighboring mesh blocks which have coincident mesh points along the interface separating the two blocks (as used in this study), a simple direct specification of the phantom cell data based on the near boundary cell data from the neighboring block has been used successfully. This concept is illustrated graphically in Figure 3.7. Each phantom cell in the block of interest has a direct correspondance with a near boundary cell in the neighboring mesh block, and the block coupling is achieved numerically by simply assigning the value of the corresponding cell in the neighboring block to the phantom cell of the block of interest. This procedure essentially duplicates the interior point solution scheme for the near boundary cells, and uniformly enforces the conservation principles implied by the governing equations.

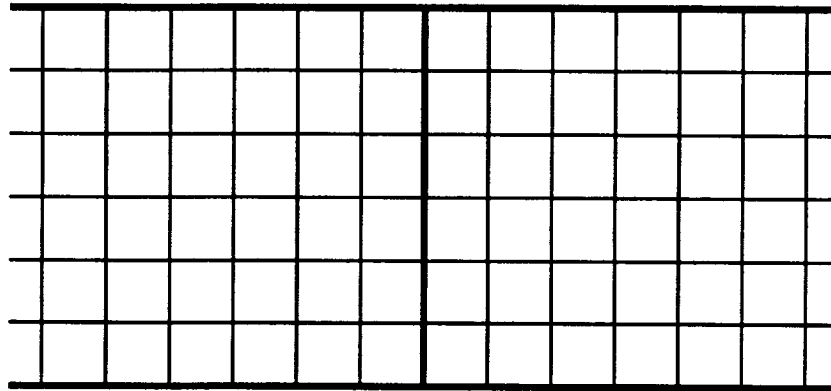
Some final comments concerning boundaries are in order at this point. Artificial damping is applied at the block boundaries by prescribing zero dissipation flux along block boundaries to maintain the global conservative nature of the solution for each mesh block. Fourth order dissipation fluxes at near boundary cells are computed using a modified one-sided differencing scheme. Implicit residual smoothing is applied at the block boundary by imposing a zero residual gradient (i.e. $(dR/dz) = 0.0$) condition at the boundary.

3.6.1 Porous Surface Boundary Condition

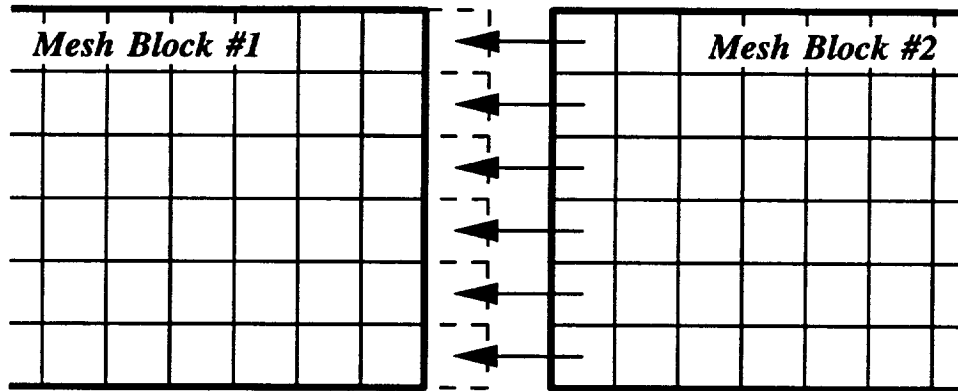
Discrete modeling of injection holes for actual gas turbine engine hardware is extremely difficult due to the large numbers of cooling holes present (often greater than 100) on even moderately high temperature applications. The problem of modeling engine hardware therefore requires some simplification

Contiguous Mesh Block Interface Boundary Coupling Scheme

Mesh Block Structure



*Phantom cell data values for mesh block#1
are determined by corresponding near-boundary
data in mesh block #2*



- Block Boundary
- Mesh Line
- Phantom Cell Representation
- Phantom Cell Data Path

Figure 3.7: ADPAC08 Contiguous Mesh Block Coupling Scheme

of the overall simulation process. To satisfy this objective, a porous surface boundary condition model was developed to permit evaluation of film-cooled engine hardware without the problems associated with modeling the individual injection sites. The porous boundary model assumes that the injection sites are relatively large in number and relatively small in scale when compared to the overall aerodynamic scale (such as airfoil span or chord), and that their influence on the flow can be modeled as a continuum across the surface of interest. This scheme is illustrated graphically in Figure 3.8. The introduction of cooling flow and the mixing which occurs at the discrete injection sites are modeled by imposing the injected flow uniformly across the region of interest and adjusting for the influence of the solid wall portion which separates adjacent injection sites. The model utilizes both the solid wall and inflow boundary conditions described above to define separate contributions due to the injection and separating solid walls, respectively. These contributions are then combined algebraically based on the relative areas associated with the injection holes and separating wall, respectively.

3.7 Runge-Kutta Time Integration

The time-stepping scheme used to advance the discrete numerical representation of the governing equations is a multistage Runge-Kutta integration. An m stage Runge-Kutta integration for the discretized equations is expressed as:

$$\begin{aligned}
 Q_1 &= Q^n - \alpha_1 \Delta t [L(Q^n) + D(Q^n)], \\
 Q_2 &= Q^n - \alpha_2 \Delta t [L(Q_1) + D(Q^n)], \\
 Q_3 &= Q^n - \alpha_3 \Delta t [L(Q_2) + D(Q^n)], \\
 Q_4 &= Q^n - \alpha_4 \Delta t [L(Q_3) + D(Q^n)], \\
 &\dots \\
 &\dots \\
 Q_m &= Q^n - \alpha_m \Delta t [L(Q_{m-1}) + D(Q^n)], \\
 Q^{n+1} &= Q_m
 \end{aligned} \tag{3.36}$$

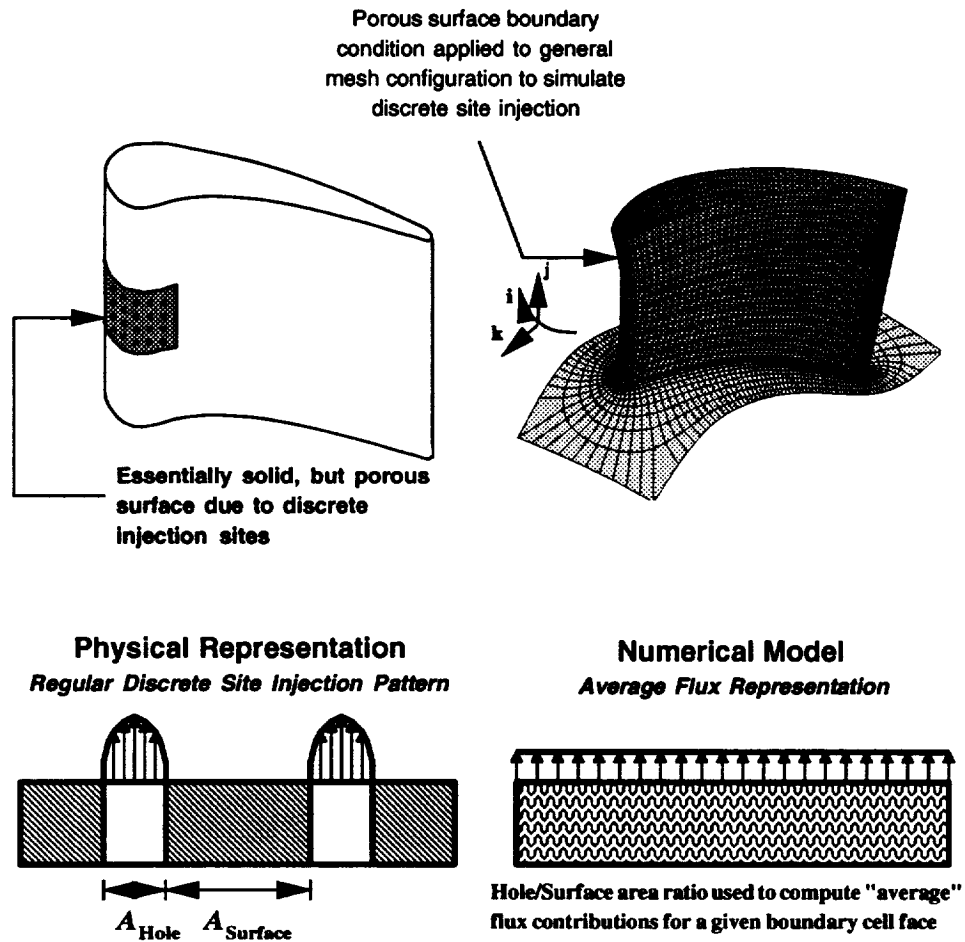


Figure 3.8: *ADPAC08* Porous Wall Boundary Condition Model Schematic

where:

$$L(Q) = L_{inv}(Q) - L_{vis}(Q) \quad (3.37)$$

For simplicity, viscous flux contributions to the discretized equations are only calculated for the first stage, and the values are frozen for the remaining stages. This reduces the overall computational effort and does not appear to significantly alter the solution. It is also generally not necessary to recompute the added numerical dissipation terms during each stage. Three different multistage Runge-Kutta schemes (2 four-stage schemes, and 1 five-stage scheme) are available in the *ADPAC08* code, but only the four-stage time-marching scheme described below was utilized for the calculations presented in this report.

The coefficients for the four stage Runge-Kutta time-marching scheme employed in this study are listed below;

$$\alpha_1 = \frac{1}{8}, \quad \alpha_2 = \frac{1}{4}, \quad \alpha_3 = \frac{1}{2}, \quad \alpha_4 = 1 \quad (3.38)$$

A linear stability analysis of the four stage Runge-Kutta time-stepping scheme utilized during this study indicate that the scheme is stable for all calculation time increments δt which satisfy the stability criteria $CFL \leq 2\sqrt{2}$. Based on convection constraints alone, the *CFL* number may be defined in a one-dimensional manner as:

$$CFL = \frac{\Delta t}{\frac{|v_x|+a}{\Delta x}} \quad (3.39)$$

In practice, the calculation time interval must also include restrictions resulting from diffusion phenomena. The time step used in the numerical calculation results from both convective and diffusive considerations and is calculated as:

$$\Delta t = CFL \left(\frac{1.0}{\lambda_i + \lambda_j + \lambda_k + \nu_i + \nu_j + \nu_k} \right) \quad (3.40)$$

where the convective and diffusive coordinate wave speeds (λ and ν , respectively) are defined as:

$$\lambda_i = Vol / (\vec{V} \cdot \vec{S}_i + a) \quad (3.41)$$

$$\nu_i = \frac{\rho Vol^2}{C_{\Delta t}(S^2)\mu} \quad (3.42)$$

The factor $C_{\Delta t}$ is a “safety factor” of sorts, which must be imposed as a result of the limitations of the linear stability constraints for a set of equations which are truly nonlinear. This factor was determined through numerical experimentation and normally ranges from 2.5-7.5.

For steady state flow calculations, an acceleration technique known as local time stepping is used to enhance convergence to the steady-state solution. Local time stepping utilizes the maximum allowable time increment at each point during the course of the solution. While this destroys the physical nature of the transient solution, the steady-state solution is unaffected and can be obtained in fewer iterations of the time-stepping scheme. For unsteady flow calculations, of course, a uniform value of the time step Δt must be used at every grid point to maintain the time-accuracy of the solution. Other convergence enhancements such as implicit residual smoothing and multigrid (described in later sections) are also applied for steady flow calculations.

3.8 Dissipation Function

In order to prevent odd-even decoupling of the numerical solution, nonphysical oscillations near shock waves, and to obtain rapid convergence for steady state solutions, artificial dissipative terms are added to the discrete numerical representation of the governing equations. The added dissipation model is based on the combined works of Jameson et al. [37], Martinelli [29], and Swanson et al. [38]. A blend of fourth and second differences is used to provide a third order background dissipation in smooth flow regions and first order dissipation near discontinuities. The discrete equation dissipative function is given by:

$$D_{i,j,k}(Q) = (D_i^2 - D_i^4 + D_j^2 - D_j^4 + D_k^2 - D_k^4)Q_{i,j,k} \quad (3.43)$$

The second and fourth order dissipation operators are determined by

$$D_\xi^2 Q_{i,j,k} = \nabla_\xi((\bar{\lambda}_\xi)_{i+\frac{1}{2}} \epsilon_{i+\frac{1}{2},j,k}^2) \Delta_\xi Q_{i,j,k} \quad (3.44)$$

$$D_\xi^4 Q_{i,j,k} = \nabla_\xi((\bar{\lambda}_\xi)_{i+\frac{1}{2}} \epsilon_{i+\frac{1}{2},j,k}^4) \Delta_\xi \nabla_\xi \Delta_\xi Q_{i,j,k} \quad (3.45)$$

where Δ_ξ and ∇_ξ are forward and backward difference operators in the ξ direction. In order to avoid excessively large levels of dissipation for cells with

large aspect ratios, and to maintain the damping properties of the scheme, a variable scaling of the dissipative terms is employed which is an extension of the two dimensional scheme given by Martinelli [29]. The scaling factor is defined as a function of the spectral radius of the Jacobian matrices associated with the ξ , η , and ζ directions and provides a scaling mechanism for varying cell aspect ratios through the following scheme:

$$(\bar{\lambda}_\xi)_{i+\frac{1}{2},j,k} = (\lambda_\xi)_{i+\frac{1}{2},j,k} \Phi_{i+\frac{1}{2},j,k} \quad (3.46)$$

The function Φ controls the relative importance of dissipation in the three coordinate directions as:

$$\Phi_{i+\frac{1}{2},j,k} = 1 + \max \left(\left(\frac{(\lambda_\eta)_{i+\frac{1}{2},j,k}}{(\lambda_\xi)_{i+\frac{1}{2},j,k}} \right)^\alpha, \left(\frac{(\lambda_\zeta)_{i+\frac{1}{2},j,k}}{(\lambda_\xi)_{i+\frac{1}{2},j,k}} \right)^\alpha \right) \quad (3.47)$$

The directional eigenvalue scaling functions are defined by:

$$(\lambda_\xi)_{i+\frac{1}{2},j,k} = U_{i+\frac{1}{2},j,k} (S_\xi)_{i+\frac{1}{2},j,k} + c(S_\xi)_{i+\frac{1}{2},j,k} \quad (3.48)$$

$$(\lambda_\eta)_{i+\frac{1}{2},j,k} = U_{i+\frac{1}{2},j,k} (S_\eta)_{i+\frac{1}{2},j,k} + c(S_\eta)_{i+\frac{1}{2},j,k} \quad (3.49)$$

$$(\lambda_\zeta)_{i+\frac{1}{2},j,k} = U_{i+\frac{1}{2},j,k} (S_\zeta)_{i+\frac{1}{2},j,k} + c(S_\zeta)_{i+\frac{1}{2},j,k} \quad (3.50)$$

The use of the maximum function in the definition of Φ is important for grids where λ_η/λ_ξ and $\lambda_\zeta/\lambda_\xi$ are very large and of the same order of magnitude. In this case, if these ratios are summed rather than taking the maximum, the dissipation can become too large, resulting in degraded solution accuracy and poor convergence. Because three-dimensional solution grids tend to exhibit large variations in the cell aspect ratio, there is less freedom in the choice of the parameter α for this scheme, and a value of 0.5 was found to provide a robust scheme.

The coefficients in the dissipation operator use the solution pressure as a sensor for the presence of shock waves in the solution and are defined as:

$$\epsilon_{i+\frac{1}{2},j,k}^2 = \kappa^2 \max(\nu_{i-1,j,k}, \nu_{i,j,k}, \nu_{i+1,j,k}, \nu_{i+2,j,k}) \quad (3.51)$$

$$\nu_{i,j,k} = \frac{|(p_{i-1,j,k} - 2p_{i,j,k} + p_{i+1,j,k}))|}{(p_{i-1,j,k} + 2p_{i,j,k} + p_{i+1,j,k})} \quad (3.52)$$

$$\epsilon_{i+\frac{1}{2},j,k}^4 = \max(0, \kappa^4 - \epsilon_{i+\frac{1}{2},j,k}^2) \quad (3.53)$$

where κ^2, κ^4 are user-defined constants. Typical values for these variables are

$$\kappa^2 = \frac{1}{2} \quad \kappa^4 = \frac{1}{64} \quad (3.54)$$

The dissipation operators in the η and ζ directions are defined in a similar manner.

3.9 Turbulence Model

As a result of computer limitations regarding storage and execution speed, the effects of turbulence are introduced through an appropriate turbulence model and solutions are performed on a numerical grid designed to capture the macroscopic (rather than the microscopic) behavior of the flow. A relatively standard version of the Baldwin-Lomax [23] turbulence model was adopted for this analysis. This model is computationally efficient, and has been successfully applied to a wide range of geometries and flow conditions.

The effects of turbulence are introduced into the numerical scheme by utilizing the Boussinesq approximation (see e.g. [35]), resulting in an effective calculation viscosity defined as:

$$\mu_{effective} = \mu_{laminar} + \mu_{turbulent} \quad (3.55)$$

The simulation is therefore performed using an effective viscosity which combines the effects of the physical (laminar) viscosity and the effects of turbulence through the turbulence model and the turbulent viscosity $\mu_{turbulent}$.

The Baldwin-Lomax model specifies that the turbulent viscosity be based on an inner and outer layer of the boundary layer flow region as:

$$\mu_{turbulent} = \begin{cases} (\mu_{turbulent})_{inner}, & y \leq y_{crossover} \\ (\mu_{turbulent})_{outer}, & y > y_{crossover} \end{cases} \quad (3.56)$$

where y is the normal distance to the nearest wall, and $y_{crossover}$ is the smallest value of y at which values from the inner and outer models are equal. The inner and outer model turbulent viscosities are defined as:

$$(\mu_{turb})_{inner} = \rho l^2 |\omega| \quad (3.57)$$

$$(\mu_{turb})_{outer} = KC_{cp}\rho F_{wake}F_{kleb}y \quad (3.58)$$

Here, the term l is the Van Driest damping factor

$$l = ky(1 - e^{(-y^+/A^+)}) \quad (3.59)$$

ω is the vorticity magnitude, F_{wake} is defined as:

$$F_{wake} = y_{max}F_{max} \quad (3.60)$$

where the quantities y_{max} , F_{max} are determined from the function

$$F(y) = y|\omega|[1 - e^{(-y^+/A^+)})] \quad (3.61)$$

The term y^+ is defined as

$$y\sqrt{\frac{\rho|\omega|}{\mu_{laminar}}} \quad (3.62)$$

The quantity F_{MAX} is the maximum value of $F(y)$ that occurs in a profile, and y_{MAX} is the value of y at which it occurs. The determination of F_{MAX} and y_{MAX} is perhaps the most difficult aspect of this model for three-dimensional flows. The profile of $F(y)$ versus y can have several local maximums, and it is often difficult to establish which values should be used. In this case, F_{MAX} is taken as the maximum value of $F(y)$ between a y^+ value of 350.0 and 1000.0. The function F_{kleb} is the Klebanoff intermittency factor given by

$$F_{kleb}(y) = [1 + 5.5(\frac{C_{kleb}y}{y_{max}})^6]^{-1} \quad (3.63)$$

and the remainder of the terms are constants defined as:

$$A^+ = 26,$$

$$C_{cp} = 1.6,$$

$$C_{kleb} = 0.3,$$

$$k = 0.4,$$

$$K = 0.0168 \quad (3.64)$$

In practice, the turbulent viscosity is limited such that it never exceeds 1000.0 times the laminar viscosity.

The turbulent flow thermal conductivity term is also treated as the combination of a laminar and turbulent quantity as:

$$k_{effective} = k_{laminar} + k_{turbulent} \quad (3.65)$$

For turbulent flows, the turbulent thermal conductivity $k_{turbulent}$ is determined from a turbulent Prandtl number $Pr_{turbulent}$ such that

$$Pr_{turbulent} = \frac{c_p \mu_{turbulent}}{k_{turbulent}} \quad (3.66)$$

The turbulent Prandtl number is normally chosen to have a value of 0.9.

In order to properly utilize this turbulence model, a fairly large number of grid cells must be present in the boundary layer flow region, and, perhaps of greater importance, the spacing of the first grid cell off of a wall should be small enough to accurately account for the inner “law of the wall” turbulent boundary layer profile region. Unfortunately, this constraint is often not satisfied due to grid-induced problems or excessive computational costs. In this report, special attention was given to the problems associated with grid refinement and the resulting effects on predicted heat transfer.

Practical applications of the Baldwin-Lomax model for three-dimensional viscous flow must be made with the limitations of the model in mind. The Baldwin-Lomax model was designed for the prediction of wall bounded turbulent shear layers, and is not likely to be well suited for flows with massive separations or large vortical structures. There are, unfortunately, a number of applications for turbomachinery where this model is likely to be invalid, although for turbine airfoils, the boundary layers typically experience a favorable pressure gradient and the model is more likely to be valid in this case. In general, however, turbulence modeling is likely to be an area requiring improvement in the future.

3.10 Implicit Residual Smoothing

The stability range of the basic time-stepping scheme can be extended using implicit smoothing of the residuals. This technique was described by Hollanders et al. [39] for the Lax-Wendroff scheme and later developed by Jameson [37] for the Runge-Kutta scheme. Since an unsteady flow calculation for a given geometry and grid is likely to be computationally more

expensive than a similar steady flow calculation, it would be advantageous to utilize this acceleration technique for time-dependent flow calculations as well. In recent calculations for two dimensional unsteady flows, Jorgensen and Chima [40] demonstrated that a variant of the implicit residual smoothing technique could be incorporated into a time-accurate explicit method to permit the use of larger calculation time increments without adversely affecting the results of the unsteady calculation. The implementation of this residual smoothing scheme reduced the CPU time for their calculation by a factor of five. This so-called time-accurate implicit residual smoothing operator was then also demonstrated by Rao and Delaney [41] for a similar two-dimensional unsteady calculation. Although this “time-accurate” implicit residual smoothing scheme is not developed theoretically to accurately provide the unsteady solution, it can be demonstrated that errors introduced through this residual smoothing process are very local in nature, and are generally not greater than the discretization error.

The standard implicit residual smoothing operator can be written as:

$$(1 - \epsilon_\xi \Delta_\xi \nabla_\xi)(1 - \epsilon_\eta \Delta_\eta \nabla_\eta)(1 - \epsilon_\zeta \Delta_\zeta \nabla_\zeta) \bar{R}_m = R_m \quad (3.67)$$

where the residual R_m is defined as:

$$R_m = \alpha_m \frac{\Delta t}{V} (Q_m - D_m), \quad m = 1, mstages \quad (3.68)$$

for each of the m stages in the Runge-Kutta multistage scheme. Here Q_m is the sum of the convective and diffusive terms, D_m the total dissipation at stage m , and \bar{R}_m the final (smoothed) residual at stage m .

The smoothing reduction is applied sequentially in each coordinate direction as:

$$\begin{aligned} R_m^* &= (1 - \epsilon_\xi \Delta_\xi \nabla_\xi)^{-1} R_m \\ R_m^{**} &= (1 - \epsilon_\eta \Delta_\eta \nabla_\eta)^{-1} R_m^* \\ R_m^{***} &= (1 - \epsilon_\zeta \Delta_\zeta \nabla_\zeta)^{-1} R_m^{**} \\ \bar{R}_m &= R_m^{***} \end{aligned} \quad (3.69)$$

where each of the first three steps above requires the inversion of a scalar tridiagonal matrix. The application of the residual smoothing operator varies with the type of Runge-Kutta time marching scheme selected. The full four

and five stage time-marching schemes utilize residual smoothing at each stage of the Runge-Kutta integration. The reduced four stage scheme employs residual smoothing at the second and fourth stages only.

The use of constant coefficients (ϵ) in the implicit treatment has proven to be useful, even for meshes with high aspect ratio cells, provided additional support such as enthalpy damping (see [37]) is introduced. Unfortunately, the use of enthalpy damping, which assumes a constant total enthalpy throughout the flowfield, cannot be used for an unsteady flow, and many steady flows where the total enthalpy may vary. It has been shown that the need for enthalpy damping can be eliminated by using variable coefficients in the implicit treatment which account for the variation of the cell aspect ratio. Martinelli [29] derived a functional form for the variable coefficients for two-dimensional flows which are functions of characteristic wave speeds. In this study, the three-dimensional extension described by Radespiel et al. [38] is utilized, and is expressed as:

$$\epsilon_{\xi} = \max \left(0, \frac{1}{4} \left[\frac{CFL}{CFL_{max}} \frac{1 + \max(r_{\eta\xi}^{\alpha} r_{\zeta\xi}^{\alpha})}{1 + \max(r_{\eta\xi} r_{\zeta\xi})} \right]^2 - 1 \right) \quad (3.70)$$

$$\epsilon_{\eta} = \max \left(0, \frac{1}{4} \left[\frac{CFL}{CFL_{max}} \frac{1 + \max(r_{\xi\eta}^{\alpha} r_{\zeta\eta}^{\alpha})}{1 + \max(r_{\xi\eta} r_{\zeta\eta})} \right]^2 - 1 \right) \quad (3.71)$$

$$\epsilon_{\zeta} = \max \left(0, \frac{1}{4} \left[\frac{CFL}{CFL_{max}} \frac{1 + \max(r_{\eta\zeta}^{\alpha} r_{\xi\zeta}^{\alpha})}{1 + \max(r_{\eta\zeta} r_{\xi\zeta})} \right]^2 - 1 \right) \quad (3.72)$$

CFL represents the local value of the CFL number based on the calculation time increment Δt , and CFL_{max} represents the maximum stable value of the CFL number permitted by the unmodified scheme (normally, in practice, this is chosen as 2.5 for a four stage scheme and 3.5 for a five stage scheme, although linear stability analysis suggests that $2\sqrt{2}$, and 3.75 are the theoretical limits for the four and five stage schemes, respectively). From this formulation it is obvious then that the residual smoothing operator is only applied in those regions where the local CFL number exceeds the stability-limited value. In this approach, the residual operator coefficient becomes zero at points where the local CFL number is less than that required by stability, and the influence of the smoothing is only locally applied to those regions exceeding the stability limit. Practical experience involving unsteady flow calculations suggests that for a constant time increment, the majority

of the flowfield utilizes CFL numbers less than the stability-limited value to maintain a reasonable level of accuracy. Local smoothing is therefore typically required only in regions of small grid spacing, where the stability-limited time step is very small. Numerical tests both with and without the time-accurate implicit residual smoothing operator for the flows of interest in this study were found to produce essentially identical results, while the time-accurate residual smoothing resulted in a decrease in CPU time by a factor of 2-3. In practice, the actual limit on the calculation CFL number were determined to be roughly twice the values specified for CFL_{max} , above.

3.11 Multigrid Convergence Acceleration

Multigrid (not to be confused with a multiple blocked grid!) is a numerical solution technique which attempts to accelerate the convergence of an iterative process (such as a steady flow prediction using a time-marching scheme) by computing corrections to the solution on coarser meshes and propagating these changes to the fine mesh through interpolation. This operation may be recursively applied to several coarsenings of the original mesh to effectively enhance the overall convergence. In the present multigrid application, coarse meshes are derived from the preceding finer mesh by eliminating every other mesh line in each coordinate direction as shown in Figure 3.9. As a result, the number of multigrid levels (coarse mesh divisions) is controlled by the mesh size, and, in the case of the *ADPAC08* code, also by the indices of the embedded mesh boundaries (such as blade leading and trailing edges, etc.) (see Figure 3.9). These restrictions suggest that mesh blocks should be constructed such that the internal boundaries and overall size coincide with numbers which are compatible with the multigrid solution procedure (i.e., the mesh size should be 1 greater than any number which can be divided by 2 several times and remain whole numbers: e.g. 9, 17, 33, 65 etc.)

The multigrid procedure is applied in a V-cycle as shown in Figure 3.10, whereby the fine mesh solution is initially “injected” into the next coarser mesh, the appropriate forcing functions are then calculated based on the differences between the calculated coarse mesh residual and the residual which results from a summation of the fine mesh residuals for the coarse mesh cell, and the solution is advanced on the coarse mesh. This sequence is repeated on each successively coarser mesh until the coarsest mesh is reached. At

Multigrid Mesh Level Decomposition

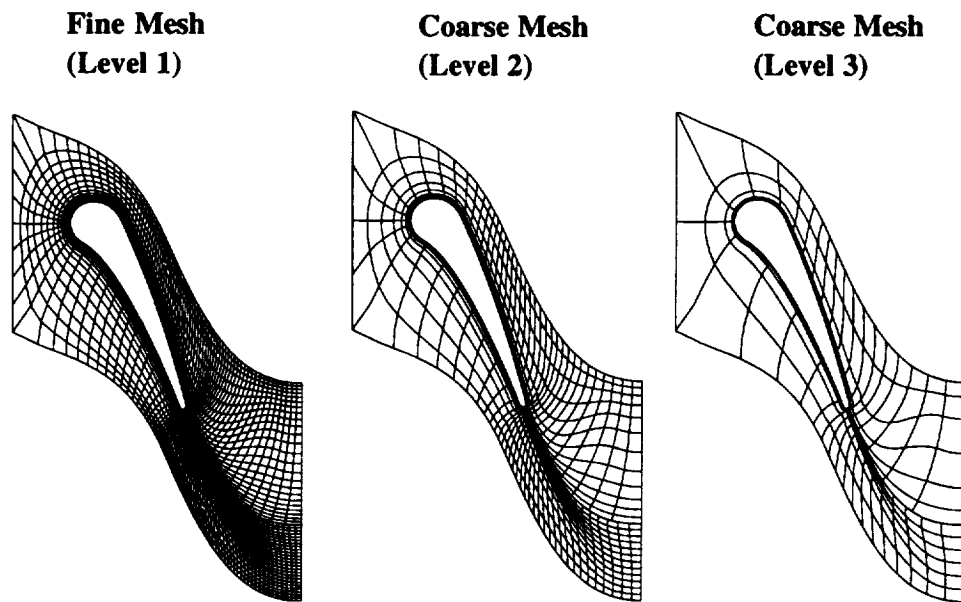


Figure 3.9: Multigrid Mesh Coarsening Strategy and Mesh Index Relation

this point, the correction to the solution ($Q_{i,j,k}^{n+1} - Q_{i,j,k}^n$) is interpolated to the next finer mesh, a new solution is defined on that mesh, and the interpolation of corrections is applied sequentially until the finest mesh is reached. Following a concept suggested by Swanson et al. [38], it is sometimes desirable to smooth the final corrections on the finest mesh to reduce the effects of oscillations induced by the interpolation process. A constant coefficient implementation of the implicit residual smoothing scheme described in Section 3.5 is used for this purpose. The value of the smoothing constant is normally taken to be 0.2.

A second multigrid concept which should be discussed is the so-called “full” multigrid startup procedure. The “full” multigrid method is used to initialize a solution by first computing the flow on a coarse mesh, performing several time-marching iterations on that mesh (which, by the way could be multigrid iterations if successively coarser meshes are available), and then interpolating the solution at that point to the next finer mesh, and repeating the entire process until the finest mesh level is reached. The intent here is to generate a reasonably approximate solution on the coarser meshes before undergoing the expense of the fine mesh multigrid cycles. Again, the “full” multigrid technique only applies to starting up a solution.

3.12 Solution Procedure

The overall solution procedure begins by defining a set of initial data, and advancing the solution from that point forward in time until the desired solution (steady state, time-periodic, or finite time interval) has been reached. Initial data is normally specified as a uniform flow, or may be read in as a “restart” of a previous existing solution. Normally, for steady flow calculations, the “full” multigrid startup procedure is utilized to accelerate convergence by initializing the solution on a coarse mesh before incurring the expense of fine mesh iterations. Steady state solutions are normally deemed converged when the average residual R has been reduced by a factor of 10^{-3} , or when the residual has ceased to be reduced. It is possible that for some steady flow calculations, the solution is truly unsteady (i.e. - vortex shedding behind a circular cylinder) and in these cases the residual may not be reduced beyond a certain limit.

Multigrid V-Cycle Strategy

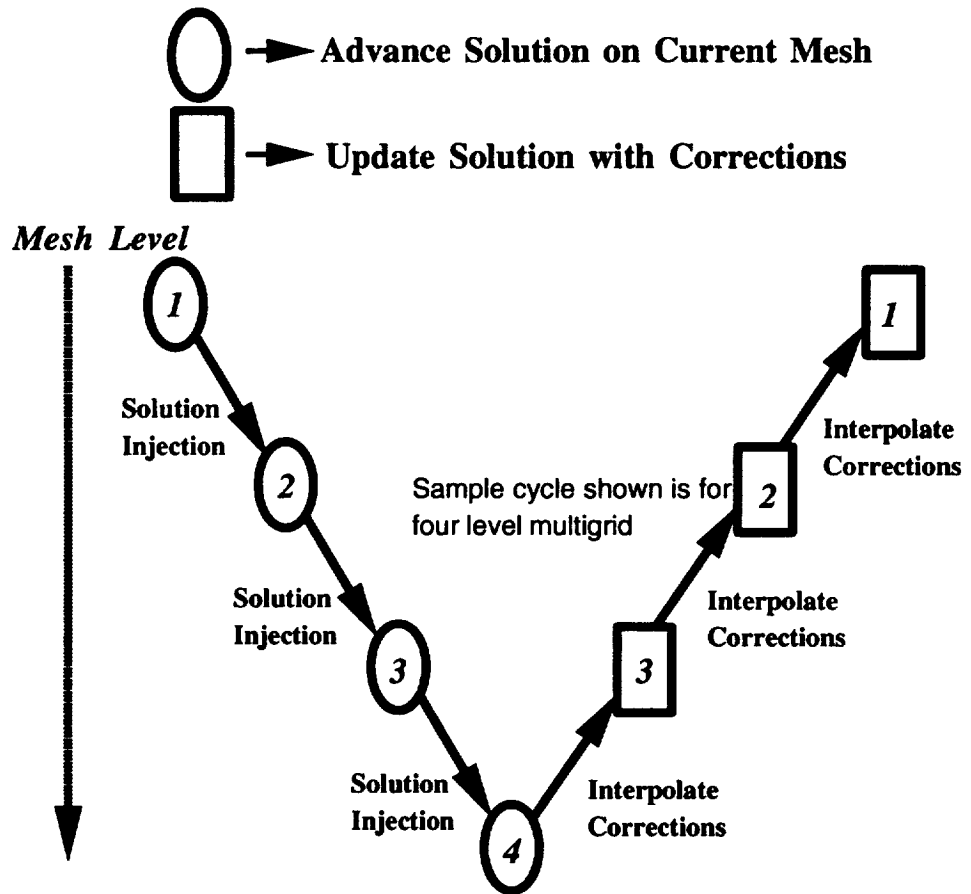


Figure 3.10: Multigrid V Cycle Strategy

Chapter 4

MARK II VANE CASCADE 2-D HEAT TRANSFER CALCULATIONS

In order to assess the accuracy of the *ADPAC08* analysis of turbine vane heat transfer, and to provide some measure of the effect of geometry on solution behavior, several preliminary 2-D calculations were performed for the Mark II vane cascade described in Reference [1]. This airfoil has been tested extensively through both experimental measurements and through numerical analysis [1].

4.1 Mark II Vane Cascade Description

The Mark II design is characteristic of an advanced first stage core turbine. The experimental data used for this preliminary set of comparisons were derived from Reference [1]. Experimental data were taken for two different exit Mach numbers (0.9 and 1.05) in a linear cascade facility. A complete description of the cascade facility and test procedure and data reduction are given in Reference [1]. Details of the Mark II vane design are given in Table 4.1.

An interesting feature of this test case is that at the exit flow Mach numbers tested, a strong normal shock forms on the suction surface of the airfoil at approximately 40% axial chord. This feature contributes to the robust-

Mark II Vane Cascade Design Parameters

Setting Angle	63.69 degrees
Air Exit Angle	70.96 degrees
Throat	1.568 inches
Vane Height	3.000 inches
Vane Spacing	5.108 inches
Suction Surface Arc	6.274 inches
Pressure Surface Arc	5.098 inches
True Chord	5.363 inches
Axial Chord	2.698 inches

Table 4.1: Mark II Vane Cascade Design Parameters

ness of the Navier-Stokes solution approach (as opposed to a boundary layer code) in that heat transfer in the shock-induced separation and subsequent reattachment regions can be accurately predicted whereas pressure-gradient specification boundary layer schemes will fail due to the singularity of the equations for these flow conditions.

4.2 Mark II Vane Cascade Mesh Generation

The *ADPAC08* analysis was applied to the Mark II vane during this preliminary study to predict both aerodynamic and heat transfer performance. The calculations were performed using 2-D C-type meshes generated using the *JERRYC/TOMC* mesh generation system developed for the *TRAF2D* [15] code, and are similar in construction to the 3-D mesh which was generated for the 3-D discrete site film-cooling calculations for the C3X airfoil described later in this report. An illustration of the C-type mesh is given in Figure 4.3.

The C-grid generated by the *JERRYC/TOMC* combination has a non-contiguous mesh connection along the approximate wake centerline extending from the vane trailing edge. This mesh boundary is handled by the **TRAF**

boundary procedure in the *ADPAC08* code. The *datajc* and *airfoil.dat* files used by the *JERRYC* mesh generation code for the finest mesh (Mesh #5) are listed in Appendix A. The corresponding *ADPAC08* input file and boundary data file for the calculation of the Mark II airfoil are also given in Appendix A for reference.

4.3 Mark II Vane 2-D Heat Transfer Mesh Dependence Study

In order to quantify the effects of mesh density on predicted aerodynamic and heat transfer performance, a mesh dependence study was performed for the Mark II vane geometry. A series of five meshes with increasing mesh density were analyzed at identical flow conditions, and predicted airfoil surface static pressure distributions and heat transfer coefficient distributions were compared to determine the minimum mesh density required for mesh-independent heat transfer results. This minimum mesh density was then later applied to predict additional flow cases for the Mark II airfoil cascade. The flow conditions selected for this study correspond to Run 4321 of the Mark II airfoil described in Reference [1]. The exit Mach number is 0.89, inlet total pressure and total temperature were 38.33 psia and 1389 degrees R, respectively.

A common measure of mesh integrity for heat transfer predictions is the near wall value of y^+ defined as:

$$y^+ = \frac{y(|\tau_{wall}|/\rho_{wall})^{\frac{1}{2}}}{\nu_{wall}}$$

where y is the distance from the wall to the first mesh point off the wall, ρ_{wall} is the density at the wall, τ_{wall} is the wall shear stress, and ν_{wall} is the kinematic viscosity at the wall. Most studies recommend a near wall mesh spacing resulting in a y^+ value of 3.0 or less in order to place at least one mesh point in the laminar sublayer of the boundary layer flow. This restriction is necessary to accurately predict near wall flow characteristics such as skin friction and heat transfer. In each of the results presented below, detailed measures of the mesh refinement are given in the form of near airfoil surface mesh y^+ plots.

Predicted airfoil surface heat transfer coefficients were determined by the following first order approximation

$$h_{surface} = \frac{-k(T_{nearwall} - T_{wall})}{\Delta n(T_{total, freestream} - T_{wall})}$$

where $h_{surface}$ is the airfoil surface heat transfer coefficient, k is the fluid thermal conductivity, T_{wall} and $T_{nearwall}$ are the fluid static temperatures at the wall and the first mesh point off the wall, respectively, $T_{total, freestream}$ is the freestream total temperature, and Δn is the distance between the wall and the first mesh point off the wall (the mesh is assumed to be normal to the wall at the airfoil surface). The fluid thermal conductivity is evaluated from a constant value of the Prandtl number defined as

$$Pr = \frac{c_p \mu}{k} = 0.69$$

where c_p is the specific heat at constant pressure, and μ is the fluid viscosity evaluated using the Sutherland formula [35]. The value of 0.69 for the Prandtl number was selected from a chart of Prandtl number versus temperature for air [16] evaluated at the average of the fluid total and wall temperatures. All presented heat transfer values are normalized by a reference value of 200 BTU/hr/ft²/F.

Details of the five meshes employed in the mesh dependence study are presented in Table 4.2. The first four meshes were designed to increase both the number of normal (mesh lines around the airfoil) and the number of contour (mesh lines away from the airfoil) mesh lines used in the C-type mesh. The fifth mesh increased the number of contour mesh lines only. Each increase in the number of contour mesh lines was accompanied by a reduction in the minimum spacing employed between adjacent contours at the airfoil surface. Graphical illustrations of the five mesh systems are presented in Figures 4.3-4.7 along with the predicted Mach number contours for a transitional flow. Each mesh was generated such that 3 levels of multigrid were available to the *ADPAC08* during execution. Each run for all five meshes were performed by using the full multigrid initialization procedure, using 100 iterations on each coarse mesh level, followed by 300 iterations on the fine mesh.

Preliminary computations indicated that for the coarser meshes, the solution convergence normally encountered a limit cycle after 100 fine mesh

iterations due to numerical “noise” in the turbulence model. The source of the turbulence model “noise” was traced to the calculation of the y_{max} parameter associated with the F_{max} parameter in the outer portion of the Baldwin-Lomax turbulence model (see Section 3.5). During the evaluation of the turbulence model, a discrete search is performed along the grid lines extending normal to the airfoil surface to determine the computational cell with the maximum value of $F(y)$ in the turbulent boundary layer. The distance from the airfoil surface where $F(y)$ peaks, y_{max} , is then used in the evaluation of the turbulent viscosity for the outer portion of the Baldwin Lomax turbulence model. During the course of the time-marching solution, the actual mesh cell where $F(y)$ peaks occasionally varies from one mesh index to the next (perhaps occurring at $j=11$ at one iteration and then at $j=12$ at the next iteration). This change results in a finite “jump” in the value of y_{max} since y_{max} is not a continuous function, but is represented by the discrete values associated with the mesh. This “jumping” from iteration to iteration in the value of y_{max} was the direct cause of the turbulence model “noise” which caused the limit cycle in the overall solution convergence. This limit cycle normally centered around a log10 RMS residual level of -6.5 to -7.5, which is normally considered to be a converged solution. It was desirable to analyze the effect of convergence level on predicted airfoil surface heat transfer, and it was therefore important to be able to achieve solutions at lower convergence levels. To counter this problem, a strategy was adopted whereby the turbulent viscosity was “frozen” after 150 fine mesh iterations, resulting in overall convergence levels a full order of magnitude lower than those achievable when the turbulence parameters were updated at every iteration. The effect on convergence for this procedure is illustrated in Figure 4.1. This figure compares the convergence history behavior for two calculations at the same operating condition. The first calculation utilized the standard approach whereby the turbulence model is updated at every iteration throughout the calculation. The second calculation employs the frozen turbulence modeling scheme described above. The limit cycle associated with the standard turbulence model application is clearly present after approximately 370 total iterations (200 on coarse meshes + 160 on the fine mesh). Freezing the turbulent viscosity after 150 fine mesh iterations (350 total iterations) results in a continuous decline in the solution convergence to a log10 RMS value below -8.5. No discernable difference was observed between the standard turbulence model approach (limit cycle convergence)

Mark II Vane Cascade Mesh Dependence Study Mesh Geometric Parameters

Mesh	Size	Normal Mesh Spacing at Airfoil Surface ¹	# Pts. S.S.	# Pts. P.S.	#Pts. Wake	#Pts. Inlet
Mesh #1	145x25	0.000250	48	24	24	8
Mesh #2	193x33	0.000100	64	32	32	8
Mesh #3	289x41	0.000050	96	48	48	16
Mesh #4	385x49	0.000025	128	64	64	16
Mesh #5	385x65	0.000010	128	64	64	16

1 – normalized by airfoil axial chord

Table 4.2: Mark II Vane Cascade Mesh Dependence Study Mesh Parameters

results and the frozen turbulence model results for heat transfer coefficient as demonstrated in Figure 4.2. This figure compares the predicted airfoil surface heat transfer coefficient distributions for the two calculations described above. The differences between the two heat transfer coefficient distributions are so slight that it was concluded that the distributions were essentially independent of convergence at this log₁₀ RMS residual level. Although the turbulence model limit cycle was evident *only* in the coarser meshes, the frozen turbulence model strategy was adopted for all of the calculations in the Mark II mesh dependence study.

The following paragraphs describe results from the Mark II vane cascade mesh dependence study. The *ADPAC08* analysis was applied to the Mark II cascade in three different modes for each of the 5 meshes. The first mode was based on purely laminar flow, the second on fully turbulent flow, and the third was based on transitional flow calculations. The purpose of the fully laminar and fully turbulent flow calculations was to pinpoint the accuracy of the calculation in the laminar flow region (near the leading edge) and to demonstrate the requirement for accurate transition modeling for turbine airfoil heat transfer analysis.

**Mark II Airfoil Cascade (uncooled, $M_{exit}=0.89, Re1.56E6$)
 ADPAC 2-D Aerodynamic Analysis-Frozen Turbulence Model Strategy
 Convergence History (193x33 Mesh)**

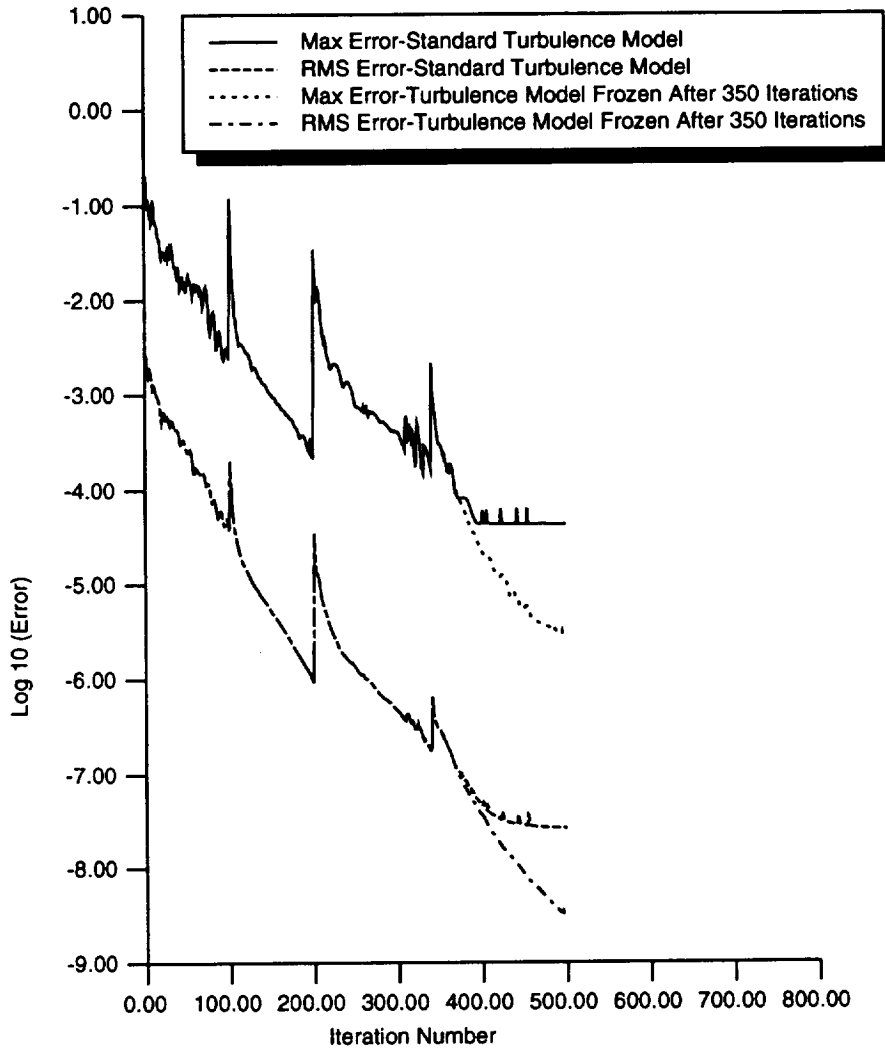


Figure 4.1: Mark II Vane Mesh Dependence Study Frozen Turbulence Model Strategy Convergence History Comparison

**Mark II Airfoil Cascade (uncooled, $Mach=0.89, Re_2=1.56E6$)
 ADPAC 2-D Aerodynamic Analysis--Frozen Turbulence Model Strategy
 Airfoil Heat Transfer Coefficient Distribution ($h_o=200 BTU/hr/sqft/F$)**

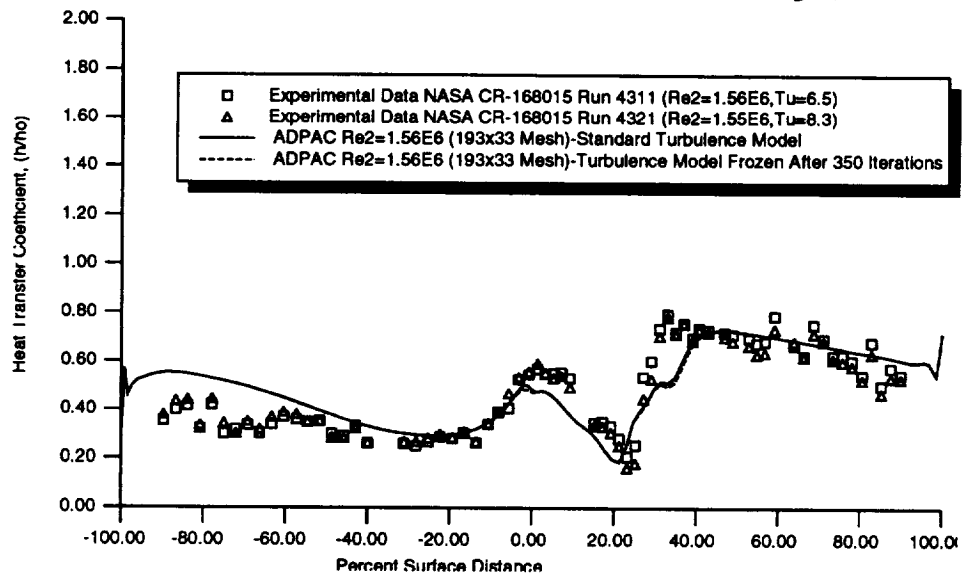


Figure 4.2: Mark II Vane Mesh Dependence Study Frozen Turbulence Model Strategy Airfoil Surface Heat Transfer Coefficient Distribution Comparison

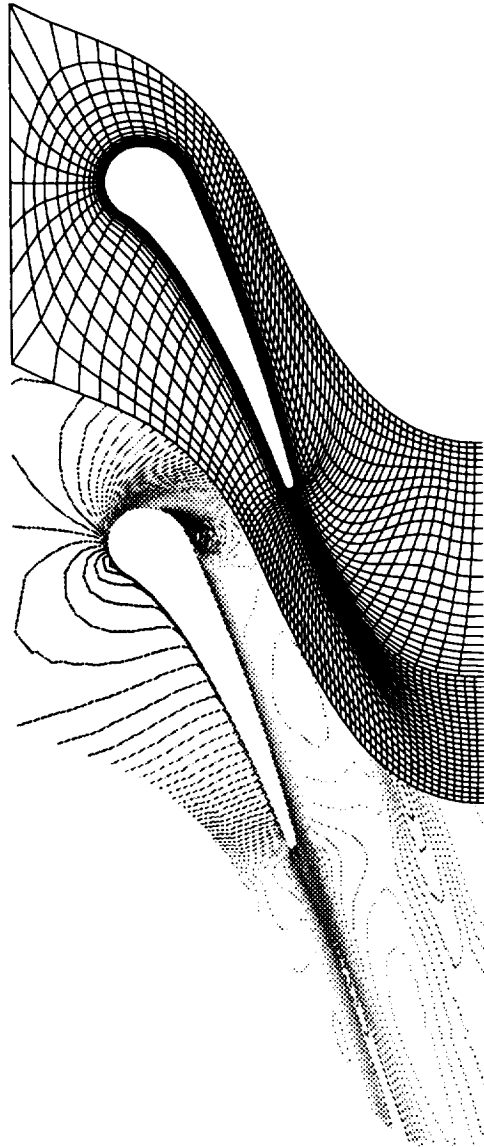


Figure 4.3: Mark II Vane Cascade Mesh Dependence Study - Mesh #1 (145x25) Mesh System and Predicted Mach Number Contours

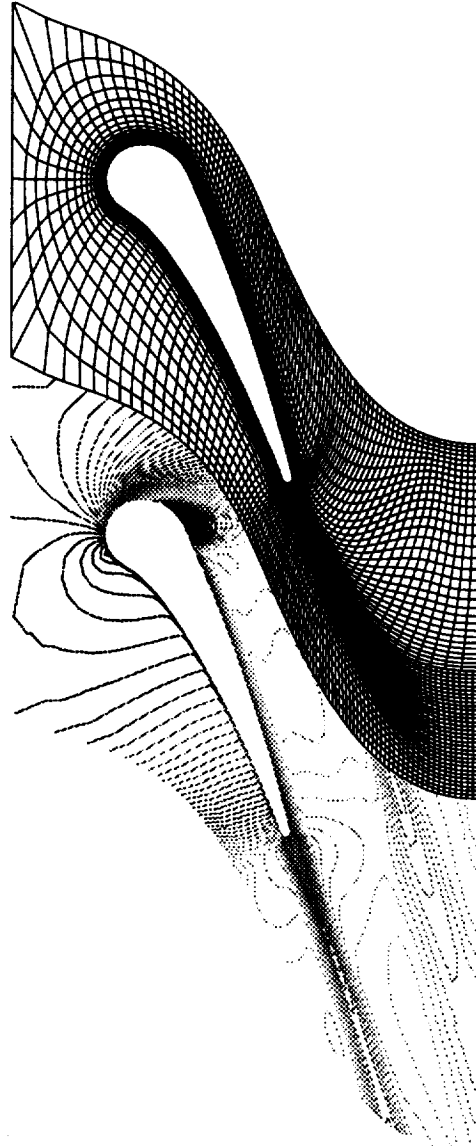
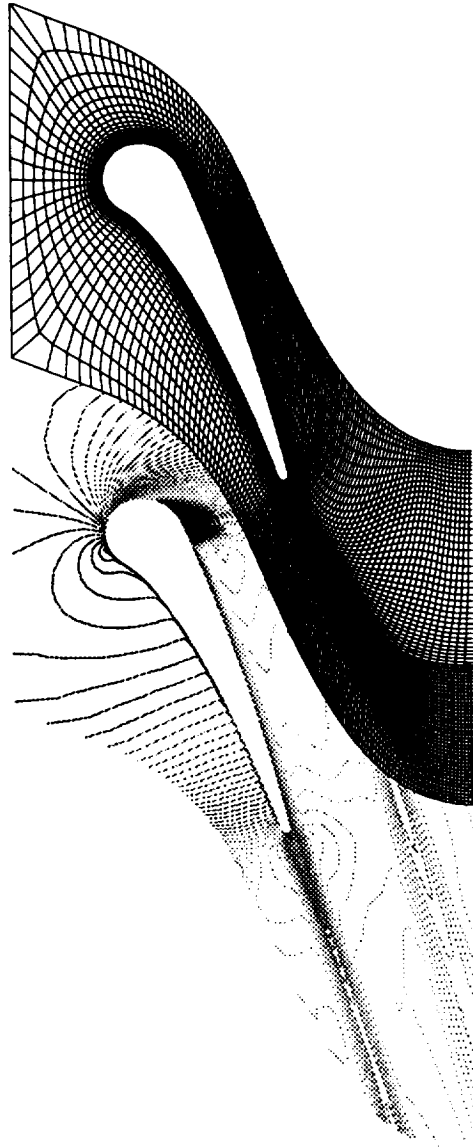


Figure 4.4: Mark II Vane Cascade Mesh Dependence Study - Mesh #2 (193x33) Mesh System and Predicted Mach Number Contours



**Figure 4.5: Mark II Vane Cascade Mesh Dependence Study - Mesh #3
(241x41) Mesh System and Predicted Mach Number Contours**



Figure 4.6: Mark II Vane Cascade Mesh Dependence Study - Mesh #4 (385x49) Mesh System and Predicted Mach Number Contours

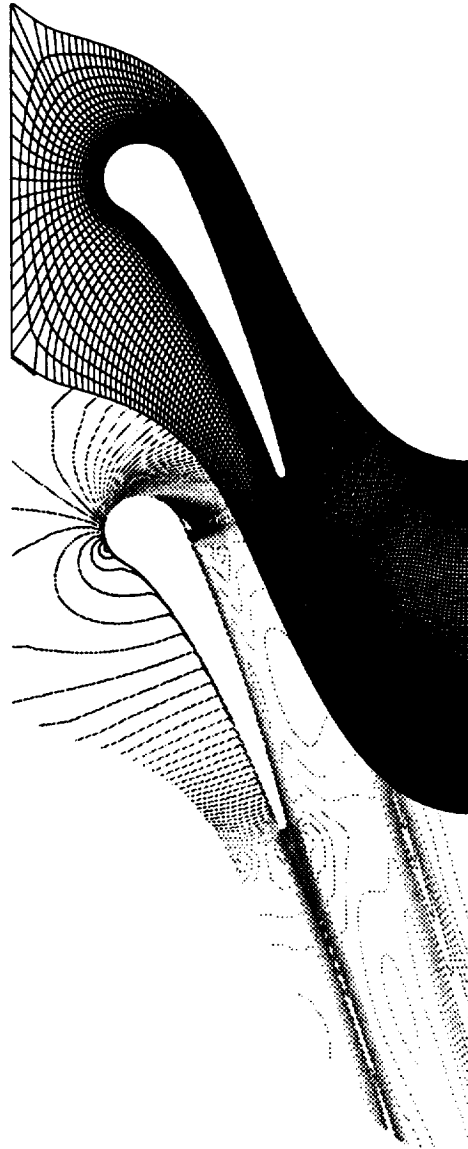


Figure 4.7: Mark II Vane Cascade Mesh Dependence Study - Mesh #5 (385x65) Mesh System and Predicted Mach Number Contours

Comparisons of the predicted and experimental airfoil surface static pressure ratio distributions for the laminar flow calculations are given in Figure 4.8 for the 5 meshes generated for the mesh dependence study. The strong shock on the suction surface causes massive separation for the laminar flow analysis, and these results are not particularly realistic or useful, but are reported here for completeness. Similar comparisons of the predicted and experimental airfoil surface heat transfer coefficient distributions for the laminar flow calculation is given in Figure 4.9. The interesting feature here is that good agreement with the experimental data was observed near the stagnation point (ostensibly because the flow is laminar there), and over a portion of the pressure surface of the airfoil. It will later be shown that while the laminar flow solution somewhat underpredicts heat transfer on the airfoil pressure surface, the fully turbulent and transitional flow solutions overpredict the pressure surface heat transfer coefficients, which indicates the presence of an unusual state of transition on the airfoil pressure surface. The resulting near airfoil surface y^+ distributions for the laminar flow calculations on the five meshes are compared in Figure 4.10.

Comparisons of the predicted and experimental airfoil surface static pressure ratio distributions for the fully turbulent flow calculations are given in Figure 4.11 for the 5 meshes generated for the mesh dependence study. In this case, the flow remains essentially attached downstream of the strong shock on the suction surface and the predicted pressure distributions are in excellent agreement with the experimental measurements. Discrepancies between the various predictions are discussed further in the section dealing with the transitional flow predictions below. A comparison of the fully turbulent predicted and experimental airfoil surface heat transfer coefficient distributions is given in Figure 4.12. Now the interesting feature is that the calculated stagnation region and pressure surface heat transfer coefficient distributions are overpredicted by the fully turbulent analysis, and, to a lesser extent, on the suction surface. The resulting near airfoil surface y^+ distributions for the fully turbulent flow calculations on the five meshes are compared in Figure 4.13.

Calculations based on transitional flow for the Mark II vane cascade employed the C-type mesh turbulence modeling scheme described in Section 3.5. The pressure surface was treated as fully turbulent, while the suction surface assumed a natural transition based on a Baldwin and Lomax [23] transition parameter (C_μ) value of 14.0. Predicted Mach number contours

**Mark II Cascade Run (uncooled, $M_{exit}=0.89, Re_2=1.56E6$)
ADPAC 2-D Aerodynamic Analysis Mesh Dependence Study (Laminar Flow)
Airfoil Surface Static Pressure Ratio Distribution**

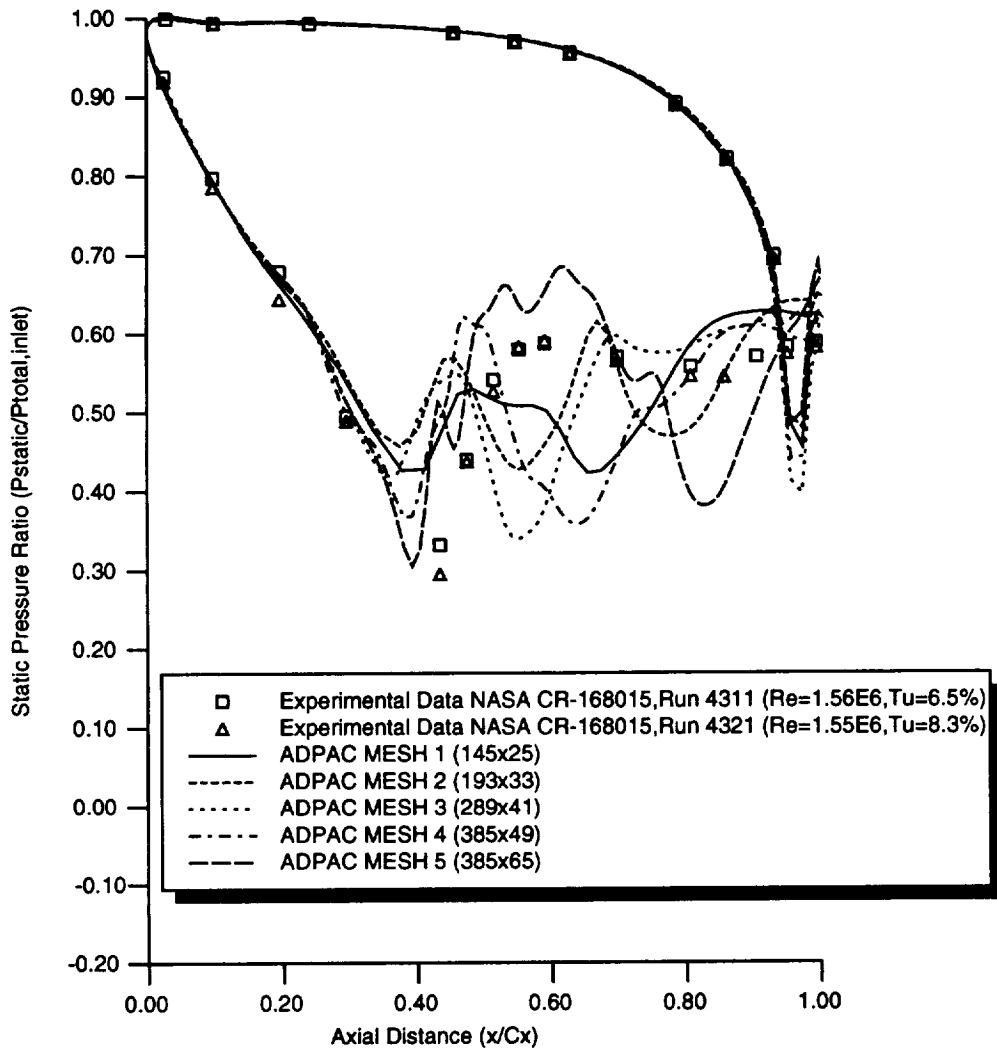


Figure 4.8: Mark II Vane Cascade Mesh Dependence Study - Comparison of Predicted (Laminar Flow) and Experimental Airfoil Surface Static Pressure Ratio Distributions.

Mark II Airfoil Cascade (uncooled, $M_{exit}=0.89, Re_2=1.56E6$)
ADPAC 2-D Aerodynamic Analysis Mesh Dependence Study (Laminar Flow)
Airfoil Heat Transfer Coefficient Distribution ($h_o=200BTU/hr/sqft/F$)

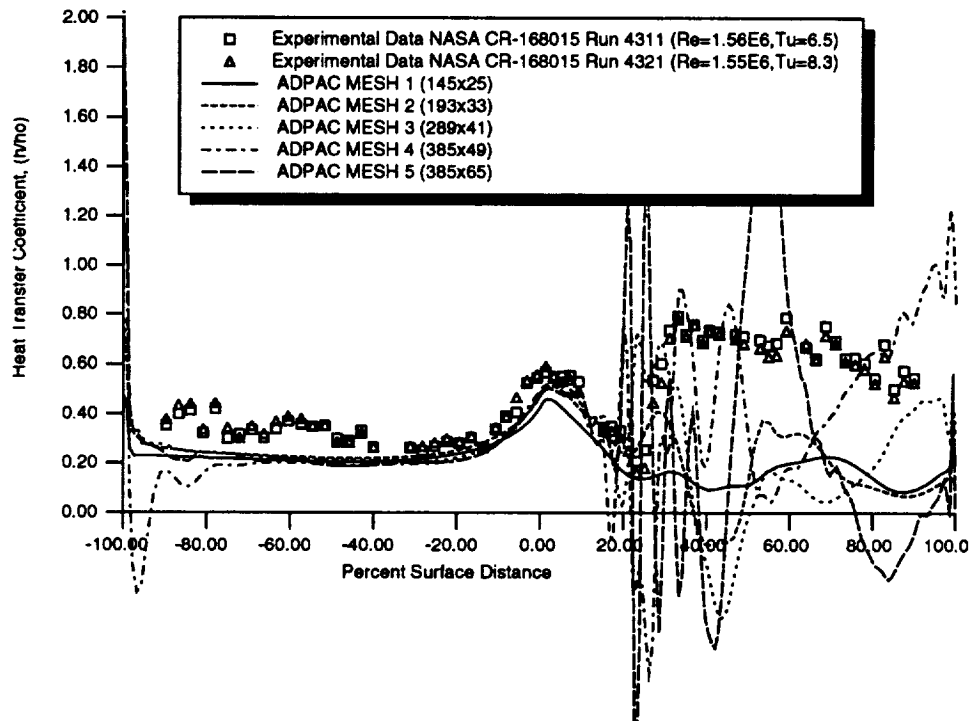


Figure 4.9: Mark II Vane Cascade Mesh Dependence Study - Comparison of Predicted (Laminar Flow) and Experimental Airfoil Surface Heat Transfer Coefficient Distributions.

*Mark II Airfoil Cascade Run 15 (uncooled, $M_{exit}=0.89, Re_2=1.56E6$)
 ADPAC 2-D Aerodynamic Analysis Mesh Dependence Study (Laminar Flow)
 Near Airfoil Surface Mesh y^+ Value*

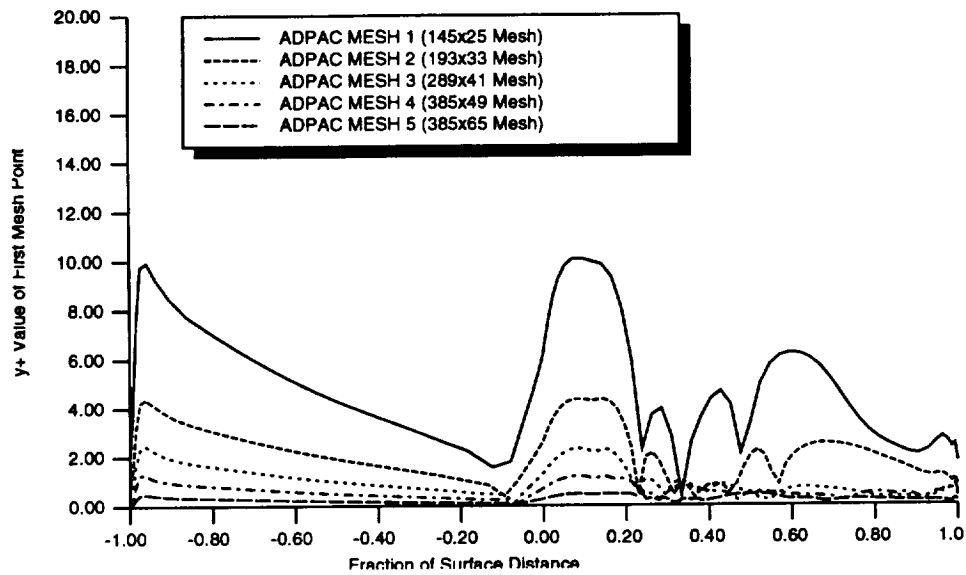


Figure 4.10: Mark II Vane Cascade Mesh Dependence Study - Comparison of Predicted (Laminar Flow) Near Airfoil Surface Mesh y^+ Values.

**Mark II Cascade Run (uncooled, $M_{exit}=0.89, Re_2=1.56E6$)
 ADPAC 2-D Aerodynamic Analysis Mesh Dependence Study (Fully Turbulent Flow)
 Airfoil Surface Static Pressure Ratio Distribution**

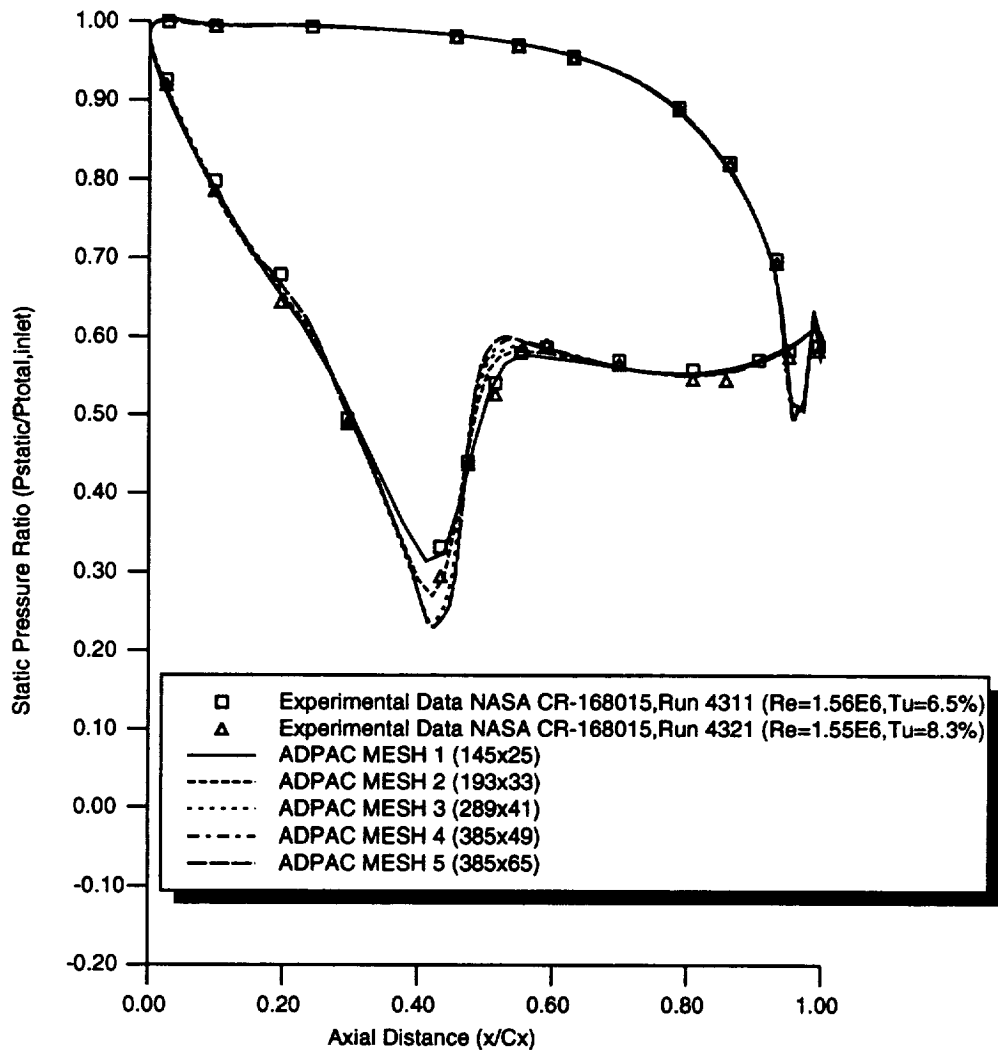


Figure 4.11: Mark II Vane Cascade Mesh Dependence Study - Comparison of Predicted (Fully Turbulent Flow) and Experimental Airfoil Surface Static Pressure Ratio Distributions.

*Mark II Airfoil Cascade (uncooled, $M_{exit}=0.89, Re_2=1.56E6$)
 ADPAC 2-D Aerodynamic Analysis Mesh Dependence Study (Fully Turbulent Flow)
 Airfoil Heat Transfer Coefficient Distribution ($h_o=200\text{BTU/hr/sqft/F}$)*

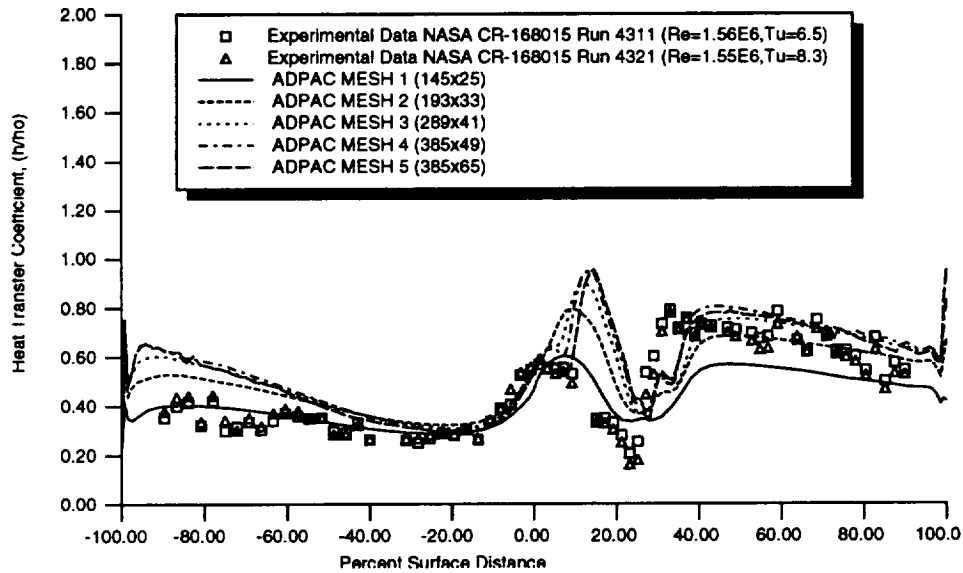


Figure 4.12: Mark II Vane Cascade Mesh Dependence Study - Comparison of Predicted (Fully Turbulent Flow) and Experimental Airfoil Surface Heat Transfer Coefficient Distributions.

*Mark II Airfoil Cascade Run 15 (uncooled, $Mach=0.89, Re=1.56E6$)
 ADPAC 2-D Aerodynamic Analysis Mesh Dependence Study (Fully Turbulent Flow)
 Near Airfoil Surface Mesh y^+ Value*

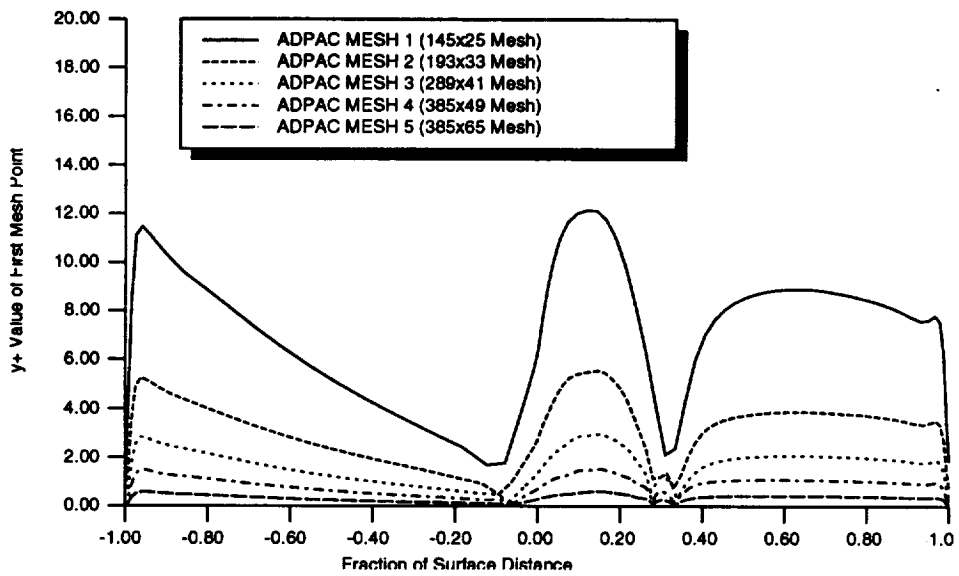


Figure 4.13: Mark II Vane Cascade Mesh Dependence Study - Comparison of Predicted (Fully Turbulent Flow) Near Airfoil Surface Mesh y^+ Values.

for each of the five meshes used in the mesh dependence study are presented in Figures 4.3-4.7, respectively. Details of the suction surface shock, rapid acceleration on the pressure surface, and wake flow may be compared as the mesh is refined. In particular, the sharpness of the shock is visually improved by streamwise mesh refinement. Comparisons of the predicted and experimental airfoil surface static pressure ratio distributions for the transitional flow calculations is given in Figure 4.14 for the 5 meshes generated for the mesh dependence study. Again, the flow remains essentially attached downstream of the strong shock on the suction surface and the predicted pressure distributions are in excellent agreement with the experimental measurements for every mesh. However, the presence of the normal shock on the suction surface of the airfoil causes some differences in the vicinity of the shock for the first four meshes considered in the mesh dependence study. These differences are clearly displayed in the vicinity of the minimum pressure on the airfoil which exists just upstream of the shock. Increasing the streamwise spatial resolution along the surface of the airfoil results in a finer representation of this shock, and true mesh independence was not achieved in the present set of meshes due to this behavior. (Note that Mesh #4 and #5 appear to be in good agreement because only the normal distribution of mesh points was altered to obtain Mesh #5 from Mesh #4.) Comparisons of the transitional predicted and experimental airfoil surface heat transfer coefficient distributions are given in Figure 4.15. In the *ADPAC08* transitional calculation, transition was only permitted on the suction surface of the airfoil. Initial calculations using the Baldwin-Lomax transition strategy described in Section 3.5 for the pressure surface of the airfoil indicated that transition would normally occur at approximately 20% axial chord on the pressure surface, but then the flow would relaminarize farther downstream due to the rather strong favorable pressure gradient. This relaminarization is clearly not indicated in the experimentally-derived heat transfer coefficients, and as a result of the relatively unknown state of transition on the pressure surface, the flow was simply treated as fully turbulent from the leading edge to the trailing edge on the pressure side of the airfoil. As a result, the pressure surface predictions are generally higher than the experimental data over most of the pressure surface. It appears that the heat transfer predictions from Mesh #3, #4, and #5, are very nearly mesh independent, and this observation ultimately led to the conclusions regarding mesh independent heat transfer predictions described in the next paragraph.

The near airfoil surface y^+ distributions for the transitional flow calculations on the five meshes are compared in Figure 4.16. For heat transfer applications, it is normally recommended that a minimum y^+ value of 3.0 or less be maintained for the near airfoil surface mesh to achieve accurate heat transfer results. From this study, it appears that Meshes #3, #4, and #5 satisfy this criteria, and the predicted heat transfer results would appear to confirm the accuracy of this measure.

4.4 Mark II Vane 2-D Heat Transfer Operating Point Study

Following the mesh dependence study, two mesh systems were constructed and evaluated for four different cascade operating points for the Mark II cascade. The coarsest mesh system used was the 193x33 mesh illustrated in Figure 4.17. This mesh incorporates 97 points about the airfoil and has a near wall mesh spacing of 10^{-4} inches. A finer mesh (385x49) was also generated and is illustrated in Figure 4.18. This mesh utilizes 193 points about the airfoil and has a near wall mesh spacing of 1.0×10^{-5} inches. Results from the mesh dependence study suggest that near airfoil mesh y^+ values of 3.0 or less are required to establish the mesh independence of the numerical solution. For comparison, the computed near airfoil surface mesh distributions of y^+ for the two meshes previously described for the Mark II airfoil are plotted in Figure 4.19 for a flow Mach number of 0.9, and exit flow Reynolds number of 1,550,000. The finer mesh clearly satisfies the $y^+ < 3$ criteria over the entire airfoil surface, while the coarser mesh does not. It is therefore expected that the results for the finer mesh are probably representative of the mesh independent result.

The cascade operating points used in the comparisons for the Mark II vane are given in Table 4.3. The Mark II results are categorized based on the exit Mach number (either 0.9 or 1.05). Calculations for the 0.9 exit Mach number case were performed for two Reynolds numbers (1,550,000 and 2,500,000) as shown in Table 4.3. Similarly, two Reynolds numbers (2,000,000 and 2,500,000) were also computed for the 1.05 Mach number flow. The *ADPAC08* convergence history for the coarse mesh (193x33) calculation is available in Figure 4.1 for the 0.9 Mach number, 1,550,000 Reynolds number

**Mark II Cascade Run (Uncooled, $M_{exit}=0.89, Re_2=1.55E6$)
 ADPAC 2-D Aerodynamic Analysis Mesh Dependence Study (Transitional Flow)
 Airfoil Surface Static Pressure Ratio Distribution**

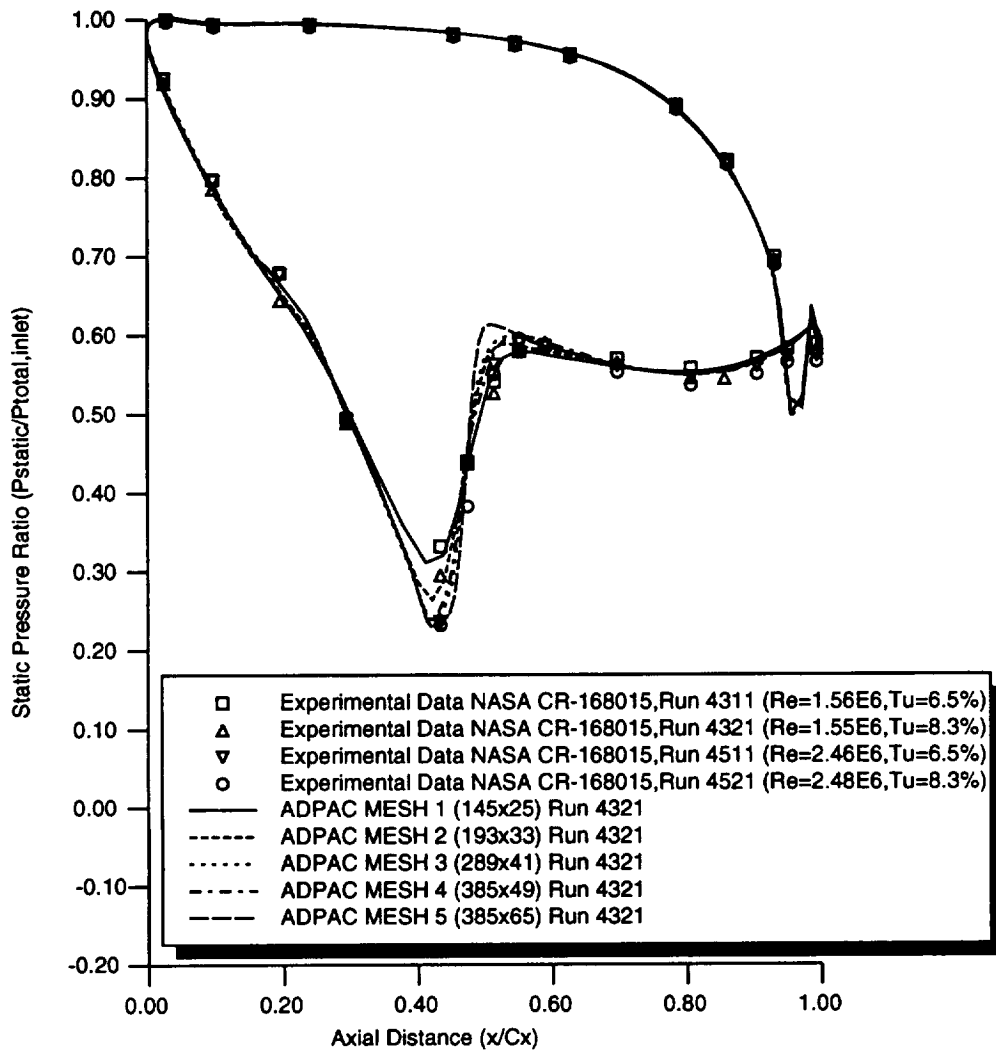


Figure 4.14: Mark II Vane Cascade Mesh Dependence Study - Comparison of Predicted (Transitional Flow) and Experimental Airfoil Surface Static Pressure Ratio Distributions.

Mark II Airfoil Cascade (Uncooled, $Mach=0.89, Re=1.56E6$)
ADPAC 2-D Aerodynamic Analysis Mesh Dependence Study (Transitional Flow)
Airfoil Heat Transfer Coefficient Distribution ($h_o=200 BTU/hr/sqft/F$)

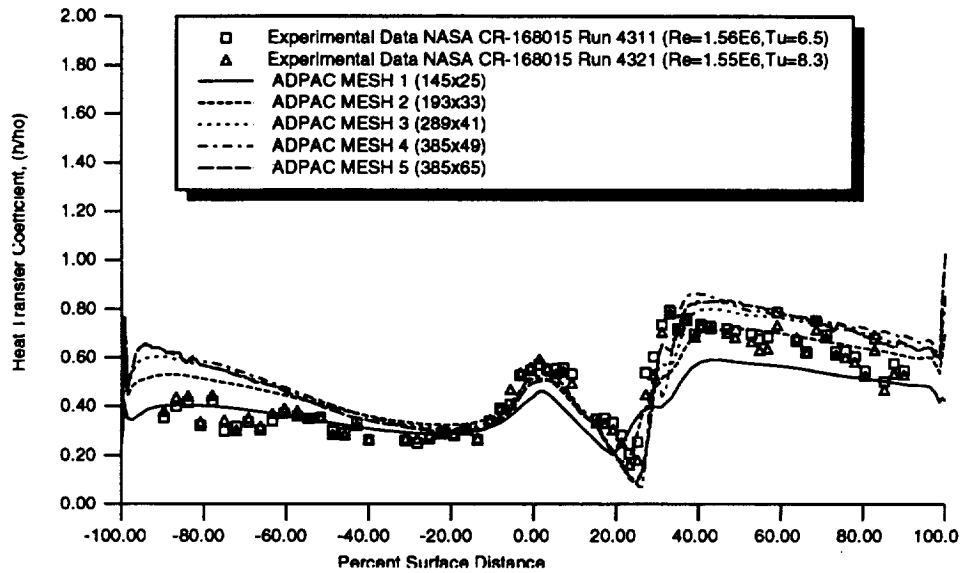


Figure 4.15: Mark II Vane Cascade Mesh Dependence Study - Comparison of Predicted (Transitional Flow) and Experimental Airfoil Surface Heat Transfer Coefficient Distributions.

*Mark II Airfoil Cascade (Uncooled, $M_{exit}=0.89, Re_2=1.56E6$)
 ADPAC 2-D Aerodynamic Analysis Mesh Dependence Study (Transitional Flow)
 Near Airfoil Surface Mesh y^+ Value*

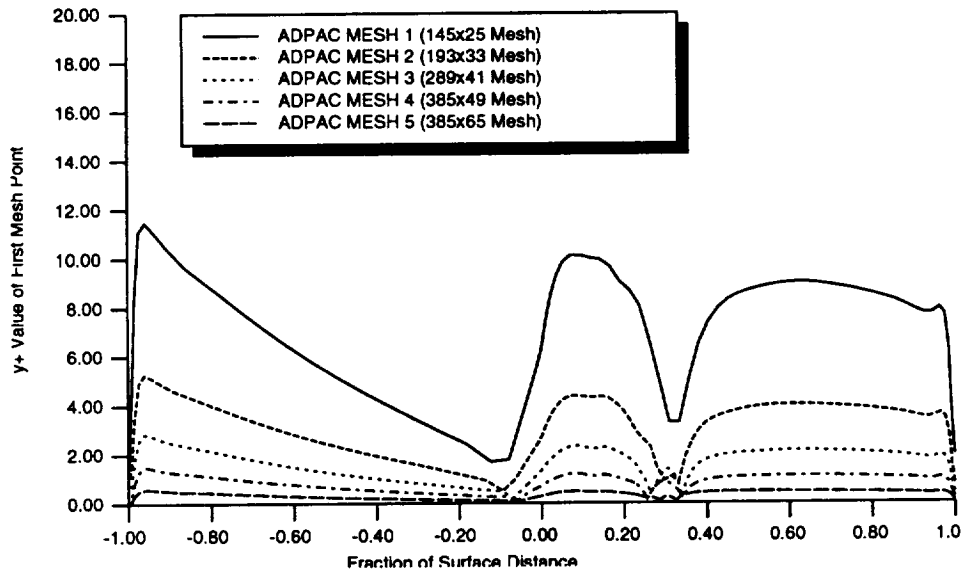


Figure 4.16: Mark II Vane Cascade Mesh Dependence Study - Comparison of Predicted (Transitional Flow) Near Airfoil Surface Mesh y^+ Values.

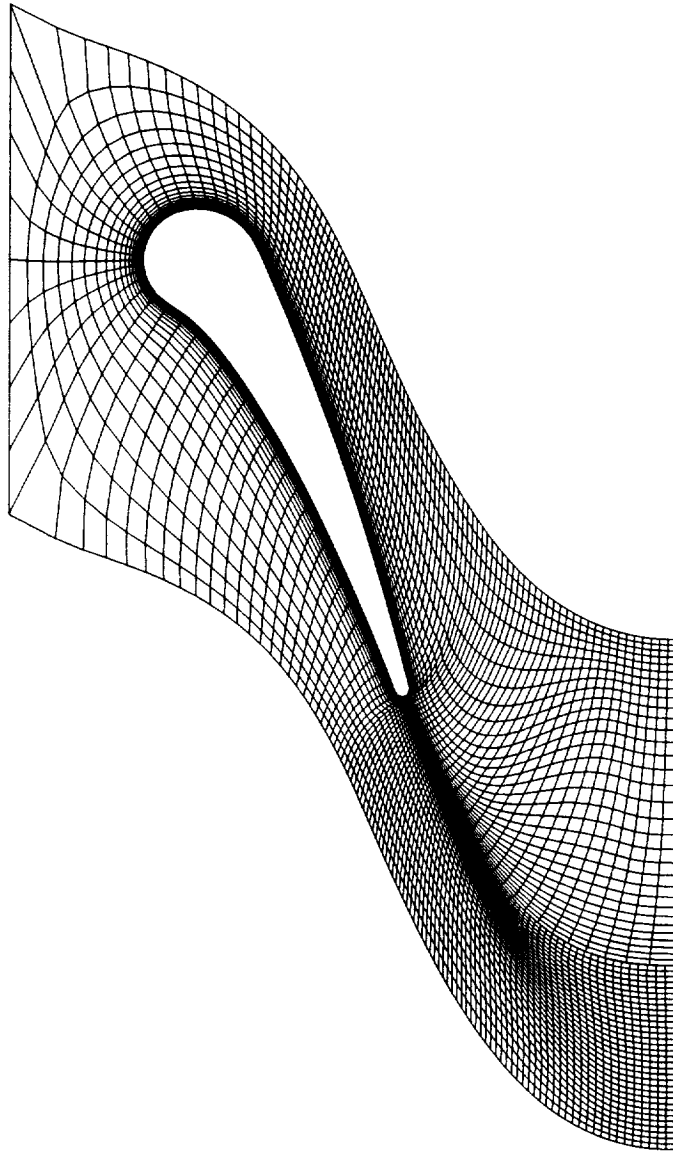


Figure 4.17: Mark II Vane Cascade 193x33 2-D C-Grid Mesh System

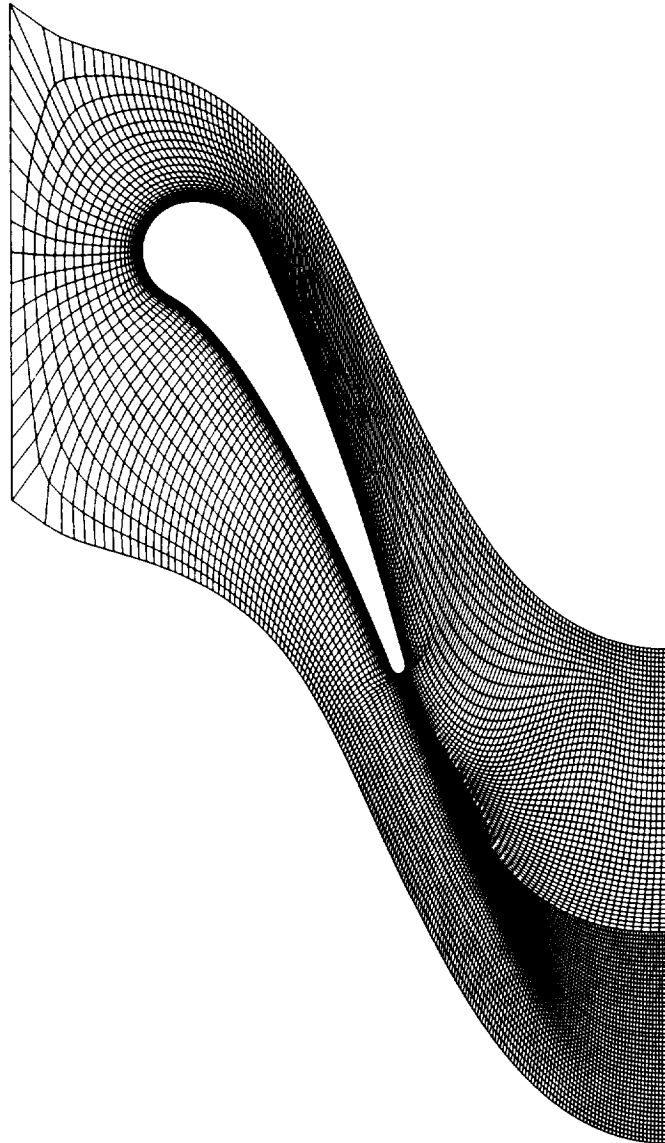


Figure 4.18: Mark II Vane Cascade Operating Point Study 385x49 2-D C-Grid Mesh System

*Mark II Airfoil Cascade (uncooled, $Mach=0.89, Re1.56E6$)
ADPAC 2-D Aerodynamic Analysis
Near Airfoil Surface Mesh y^+ Value*

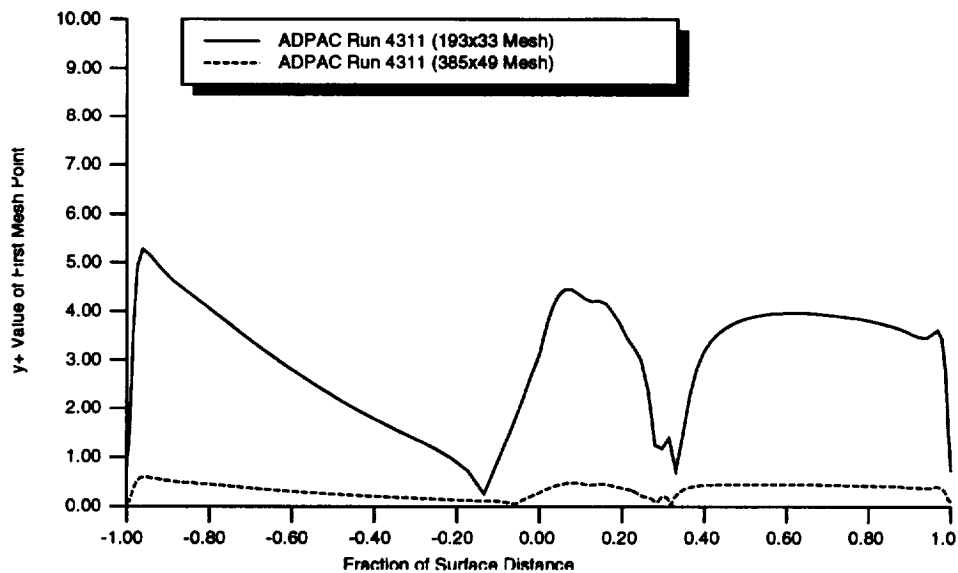


Figure 4.19: Mark II Vane Cascade Operating Point Study 2-D C-Grid Mesh System Airfoil Surface y^+ Values

Mark II Turbine Vane Flow Conditions for ADPAC Code Verification

	Run Code ¹	Exit Mach	Exit Re	Tc/Tg	Pc/Pg	Tw/Tg	Pt1 ²	Tt1 ³
Uncooled	4311	0.90	1.56E+06			0.71	5774.40	1445.0
	4321	0.89	1.55E+06			0.70	5519.52	1389.0
	5411	1.04	2.01E+06			0.68	7040.16	1418.0
	5421	1.04	2.05E+06			0.70	7237.44	1429.0
	5511	1.04	2.51E+06			0.71	8213.76	1339.0

1 - Run Code taken from NASA CR-168015

2 - Pounds per square foot

3 - Degrees Rankine

Runs 4311, 5411, 5511 Tu = 6.5%

Runs 4321, 5421 Tu = 8.3%

Table 4.3: Mark II Vane Cascade Calculation Operating Point Description

case. All calculations utilized three levels of multigrid, and the full multigrid initialization procedure. The frozen turbulence model strategy described in the previous section was utilized for all of the Mark II vane cascade calculations. Convergence was observed to be very stable and uniform for each case, and a three order reduction in the solution residual is achieved after a total of 300 iterations (100 on each coarse mesh level followed by 100 fine mesh iterations). A similar convergence behavior was observed for all other runs for the Mark II airfoil, and therefore, additional convergence histories will not be presented for each case.

Comparisons of predicted and experimental airfoil surface static pressure distributions and airfoil surface heat transfer coefficient distributions for the Mark II airfoil at an exit Mach number of 0.9 and exit flow Reynolds numbers of 1,550,000 and 2,500,000 (based on true chord) are given in Figures 4.20 and 4.21, respectively. Both the coarse (193x33) and fine (385x49) mesh predictions are plotted on each figure.

Again, the most striking feature of this flow is the presence of a normal shock on the suction surface of the airfoil at roughly 40% axial chord. The predicted and experimental airfoil static pressure distributions clearly depict the large overspeed and rapid compression associated with the shock system. Both the fine and coarse mesh solutions accurately capture this flow, and outstanding agreement with the experimental static pressure distributions was achieved. The predicted heat transfer distributions were also found to be in very good agreement with the experimental data. This is achieved, in part,

Mark II Cascade Run (uncooled, $M_{exit}=0.89$)
ADPAC 2-D Aerodynamic Analysis - Reynolds Number Comparison
Airfoil Surface Static Pressure Ratio Distribution

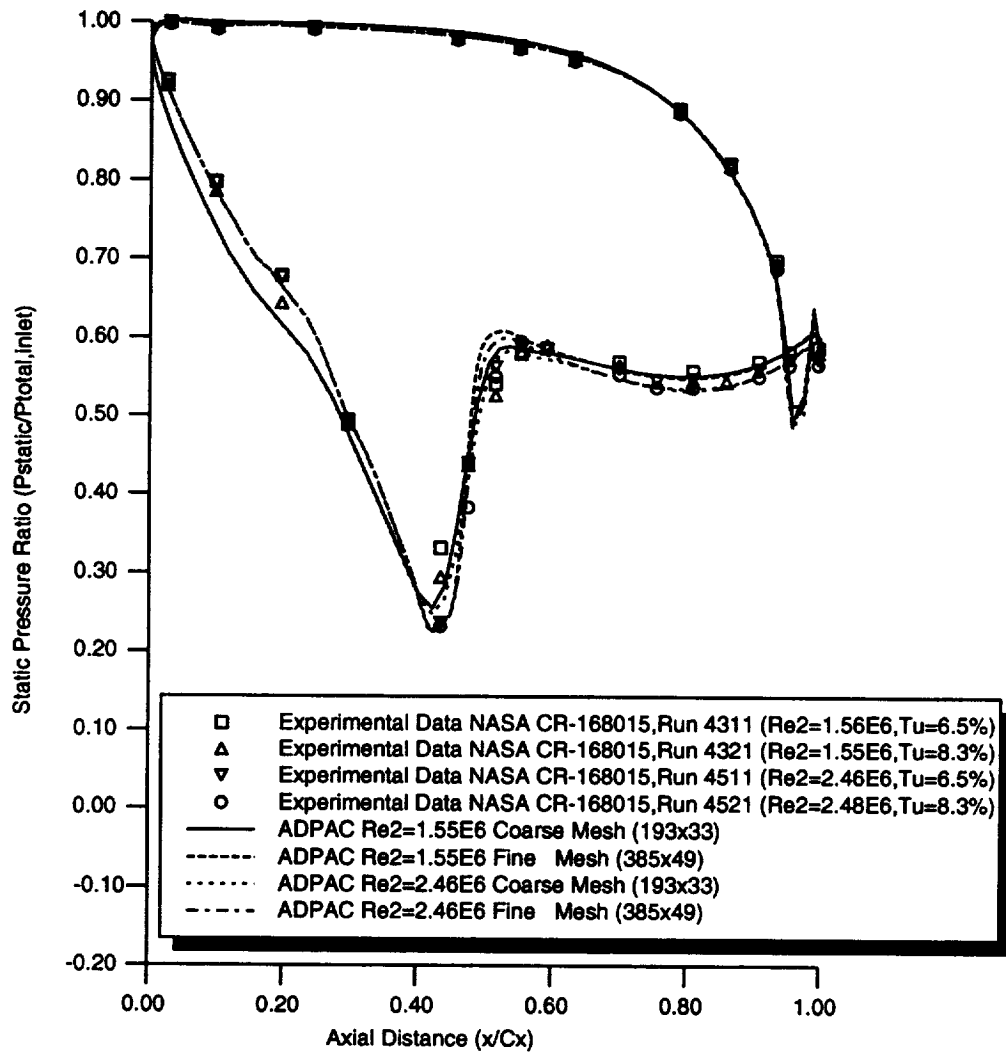


Figure 4.20: Comparison of Predicted and Experimental Airfoil Surface Static Pressure Ratio Distributions for Mark II Vane Cascade Operating Point Study ($M_2=0.89$)

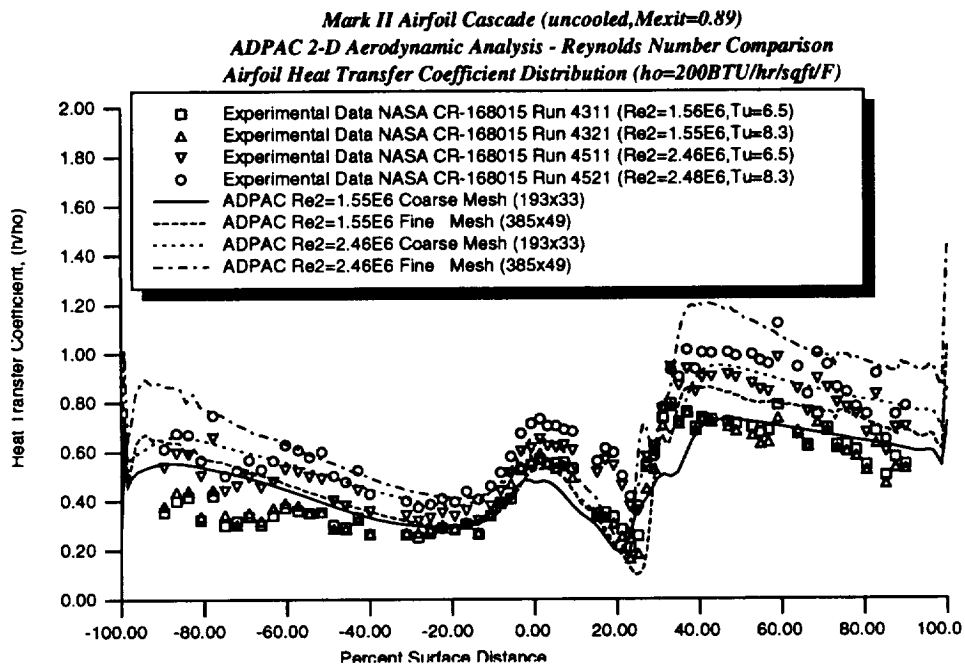


Figure 4.21: Comparison of Predicted and Experimental Airfoil Surface Heat Transfer Coefficient Distributions for Mark II Vane Cascade Operating Point Study ($M_2=0.9$)

Mark II Cascade Run (uncooled, $M_{exit}=1.05$)
ADPAC 2-D Aerodynamic Analysis - Reynolds Number Comparison
Airfoil Surface Static Pressure Ratio Distribution

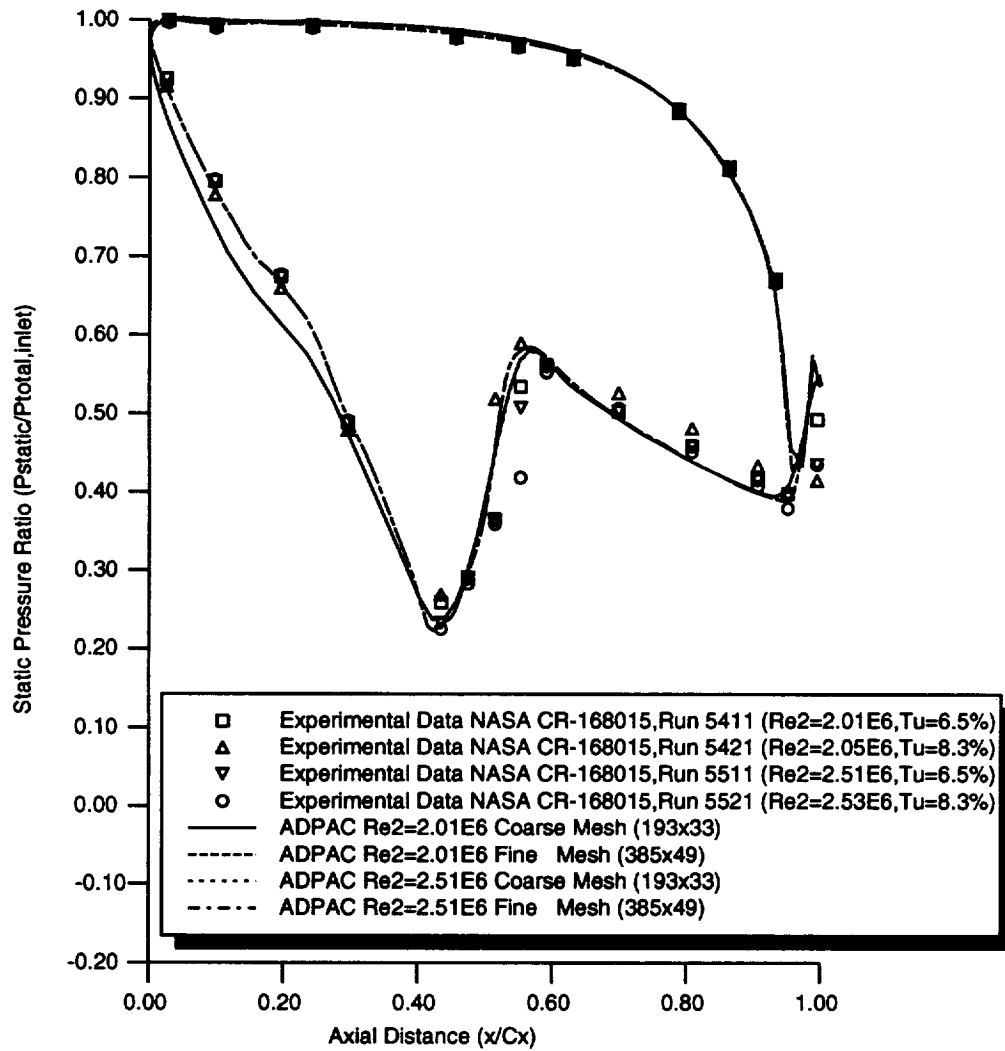


Figure 4.22: Comparison of Predicted and Experimental Airfoil Surface Static Pressure Ratio Distributions for Mark II Vane Cascade Operating Point Study ($M_2=1.05$)

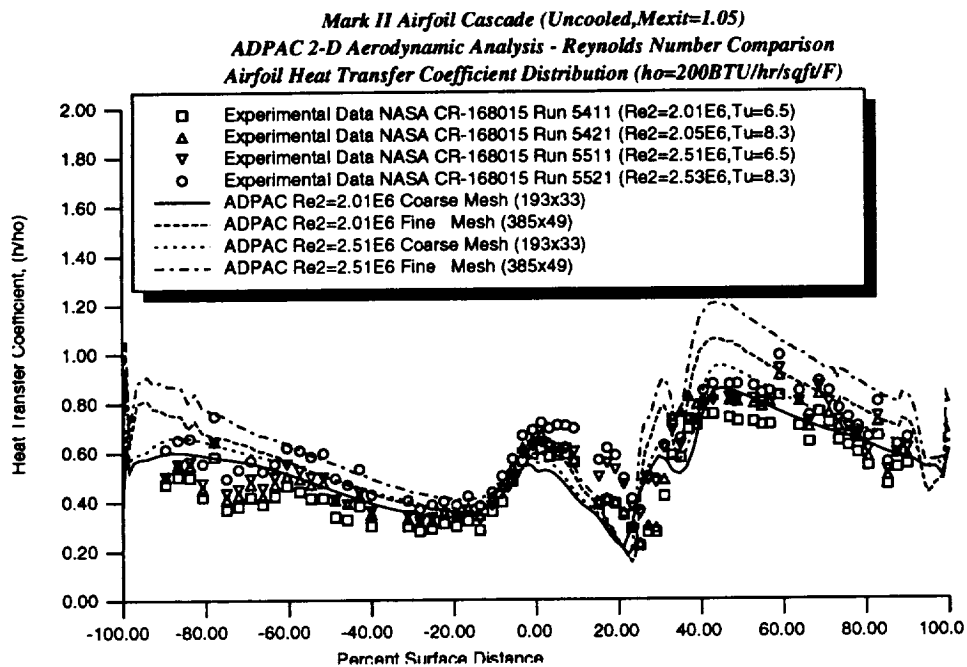


Figure 4.23: Comparison of Predicted and Experimental Airfoil Surface Heat Transfer Coefficient Distributions for Mark II Vane Cascade Operating Point Study ($M_2=1.05$)

due to the normal shock, which initiates transition in a rapid manner, much like the point transition model in the *ADPAC08* code. The absolute levels of heat transfer downstream of the leading edge and transition regions are generally overpredicted. There are substantial differences between the coarse and fine grid heat transfer coefficient distributions. In fact, the coarse grid results appear to match the experimental better than the fine mesh results. This observation demonstrates the absolute necessity for determining the true mesh dependence of any numerical scheme for predicting heat transfer, a qualification that many researchers choose to ignore. A promising observation is that the effective *change* in heat transfer levels due to changes in Reynolds numbers appears to be accurately captured by the *ADPAC08* code for *both* meshes. This suggests that differences in design configurations might be accurately predicted in spite of the fact that the absolute levels of heat transfer are not.

Comparisons of predicted and experimental airfoil surface static pressure distributions and airfoil surface heat transfer coefficient distributions for the Mark II airfoil at an exit Mach number of 1.05 and exit flow Reynolds number based on true chord of 2,000,000 and 2,500,000 are given in Figures 4.22 and 4.23, respectively. Once again, the agreement between experiment and prediction is very good, and the same trends observed in the 0.9 exit Mach number case were found in the 1.05 Mach number cases. No significant difference were observed in the airfoil surface static pressure distributions at Reynolds numbers of 2,000,000 and 2,500,000. The predicted heat transfer coefficient distributions display the observed experimental trend of increased heat transfer levels as Reynolds number increases. The overall agreement between prediction and experiment is thought to be very good, in spite of the known deficiencies of the *ADPAC08* turbulence model.

It should be mentioned that several sources of error are present which could account for some of the differences between predicted and experimental heat transfer coefficient values. The calculations were performed with a constant airfoil surface temperature, while the experimental data shows a nontrivial variation in airfoil surface temperature. For the purposes of simplifying the calculations, a constant gas Prandtl number was employed. The solutions also assume a fully turbulent pressure surface, although the real flow situation is more likely a long, gradual transition along the pressure surface. The margin of error in the experimentally-determined heat transfer coefficients is reported to be as large as +/- 6.8% near the leading edge

to +/- 23.5% near the airfoil trailing edge, so clearly, detailed comparisons cannot be interpreted too literally.

Chapter 5

C3X VANE CASCADE 2-D HEAT TRANSFER CALCULATIONS

Several preliminary 2-D calculations were performed for the C3X vane cascade described in Reference [1]. This airfoil has been tested extensively through both experimental measurements and through numerical analysis [1]. These calculations address the baseline geometry used in comparison with the film-cooled C3X turbine airfoil results described in the next chapter.

5.1 C3X Vane Cascade Description

The C3X airfoil is an Allison-designed film cooled turbine vane, experimentally tested in a planar cascade under NASA contract (References [1],[2],[3]). The C3X airfoil is shown in Figure 6.1. The C3X geometry is representative of a first vane in a modern high pressure turbine. Additional descriptions of the C3X cascade, and particularly the film cooling geometry are given in Chapter 5.0. The remainder of this chapter is dedicated to details associated with a series of 2-D heat transfer predictions for the non-cooled C3X vane cascade. A mesh dependence study and an operating point study (similar to those previously described for the Mark II vane cascade) are described in the paragraphs below for the C3X vane cascade.

The experimental data used for this preliminary set of comparisons were

C3X Vane Cascade Design Parameters

Setting Angle	59.89 degrees
Air Exit Angle	72.38 degrees
Throat	1.296 inches
Vane Height	3.000 inches
Vane Spacing	4.635 inches
Suction Surface Arc	7.001 inches
Pressure Surface Arc	5.403 inches
True Chord	5.706 inches
Axial Chord	3.077 inches

Table 5.1: C3X Vane Cascade Design Parameters

derived from References [1] and [2]. Experimental data were taken for two different exit Mach numbers (0.9 and 1.05) in a linear cascade facility. A complete description of the cascade facility and test procedure and data reduction are given in Reference [1]. Details of the C3X vane design are given in Table 5.1.

5.2 C3X Vane Cascade Mesh Generation

The *ADPAC08* analysis was applied to predict the two-dimensional flow about the C3X vane during this preliminary study to predict both aerodynamic and heat transfer performance. The calculations were performed using 2-D C-type meshes generated using the *JERRYC/TOMC* mesh generation system developed for the *TRAF2D* [15] code, and are similar in construction to the 3-D mesh which was generated for the 3-D discrete site film-cooling calculations for the C3X airfoil described later in this report. These C-type meshes are similar to those described earlier for the Mark II vane cascade.

During the course of the 2-D C3X calculations, an interesting phenomenon related to geometry and mesh generation was observed. As part of the mesh

dependence study described below for the C3X vane cascade, *ADPAC08* solutions were obtained for a series of meshes with increasing mesh density, similar to the study performed for the Mark II vane cascade using the discrete point geometry definition provided in Reference [1]. Predictions from the 2-D analysis displayed a series of oscillations in blade surface static pressure on the suction surface of the airfoil between 30% and 40% axial chord, near the throat. These oscillations were not found to exist in previous calculations using coarser meshes, and an investigation was launched to determine the cause of this behavior.

The predicted oscillations were found to be particularly sensitive to the mesh point distribution on the airfoil surface. The following meshes were studied:

- A coarse mesh developed using the *JERRYC/TOMC* [15] mesh generation programs for the non-cooled vane. The mesh dimensions were 193x25 (normals by contours).
- A finer mesh developed using *JERRYC/TOMC* for the non-cooled vane. The mesh dimensions were 497x65 (normals by contours).
- A mesh developed using *GRIDGEN*. This grid has a concentration of points near the leading edge for the resolution needed for film cooling. The dimensions are 497x65 normals by contours.

Several additional meshes were eventually generated by modifying the interpolation scheme utilized to distribute mesh points on the airfoil suction surface. The suction surface of the *GRIDGEN* mesh was modified for each interpolated definition of the vane, and aerodynamic results were obtained from the *ADPAC08* code.

The airfoil surface static pressure distributions for the various meshes are compared with experimental data in Figure 5.1. The *GRIDGEN* meshes which are to be used for film cooling result in much larger pressure oscillations than the meshes for a non-cooled vane because of the increased number of points in the area of interest.

Two factors which affect the oscillations in the surface static pressure distribution are surface curvature and the near wall mesh distribution. The oscillations in the surface static pressure distribution are caused by a step discontinuity in the slope of the surface curvature of the points that define the airfoil shape. This slope discontinuity is located in the same area as the

C3X Airfoil Cascade (Mexit=1.05, T_{wall}/T_{gas}=0.75)
ADPAC 2-D Aerodynamic Analysis
Airfoil Surface Static Pressure Ratio Distribution

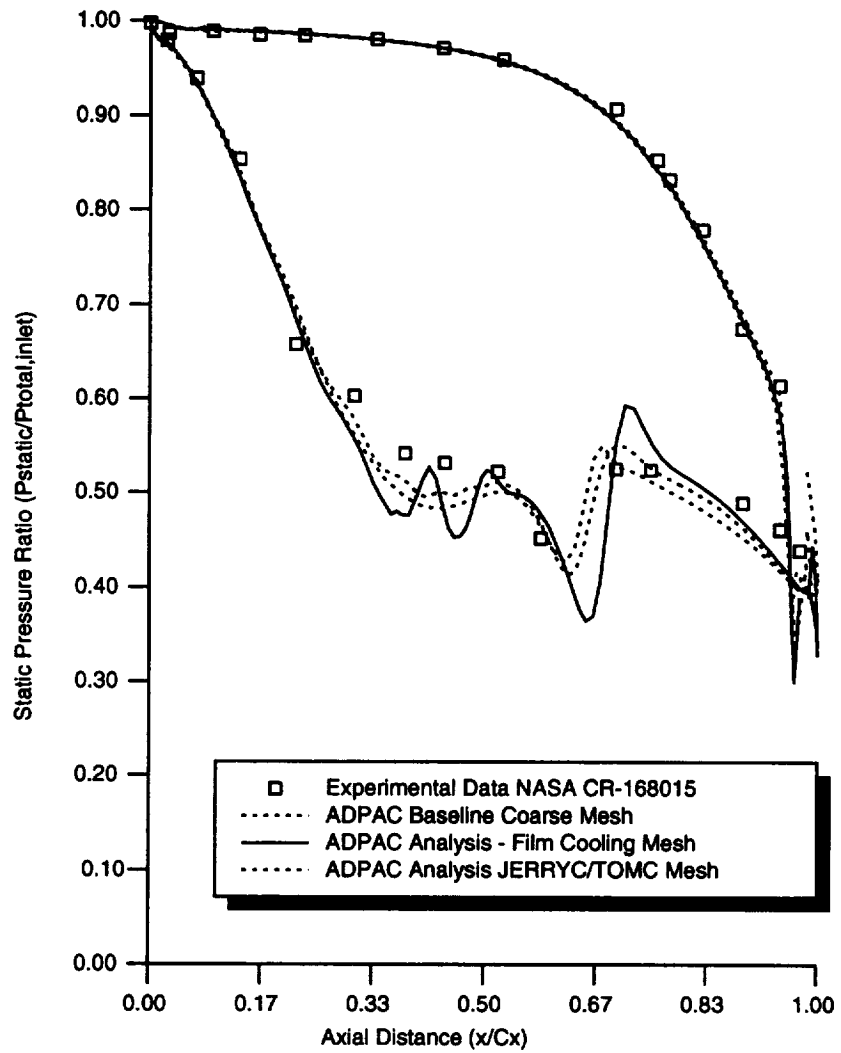


Figure 5.1: Comparison of Predicted and Experimental Airfoil Surface Static Pressure Distributions for the C3X Vane Cascade Illustrating Suction Surface Pressure Oscillations Due to Geometric Irregularity.

pressure oscillations. The aerodynamic response to the irregular surface is amplified by the fact that the disturbance occurs near the sonic point on the suction surface.

To correct this anomaly, several methods of defining the airfoil geometry have been used. Figure 5.2 illustrates the suction surface curvature distribution for the original vane definition (78 points), an Akima cubic spline fit of the original data, and a piece-wise cubic fit of the original definition. Note that the irregularity of the blade definition curvature causes overshoot in both interpolation methods.

A NURBS definition of the airfoil was provided by NASA Lewis Research Center personnel in the form of an IGES entity. Various manipulations were performed on this geometric representation but again a satisfactory blade profile could not be obtained. Ultimately, the vane surface was modified using an optimization technique to obtain a favorable pressure gradient in the area of interest (surface oscillations characteristically displayed non-favorable surface pressure gradients). This vane surface definition has a smooth curvature distribution, as shown in Figure 5.4. The 2-D calculation mesh was modified for this airfoil definition, and the *ADPAC08* code was used to obtain the aerodynamic predictions. The static pressure oscillations along the suction surface of the vane were not evident in any of the calculations using the optimized smooth airfoil definition. Figure 5.3 compares the static pressure distribution along the vane surface from the original definition with the optimized airfoil definition.

The final *datajc* and *airfoil.dat* files used by the *JERRYC* mesh generation code for the finest mesh in the mesh dependence study (Mesh #5) are listed in Appendix B. These files relate to the modified geometry used for all final calculations for the C3X airfoil in this report. The corresponding *ADPAC08* input file and boundary data file for the calculation of the C3X airfoil are also given in Appendix B for reference.

5.3 C3X Vane 2-D Heat Transfer Mesh Dependence Study

In order to quantify the effects of mesh density on predicted aerodynamic and heat transfer performance, a mesh dependence study was performed for the

*C3X Vane
Suction Surface Curvatures*

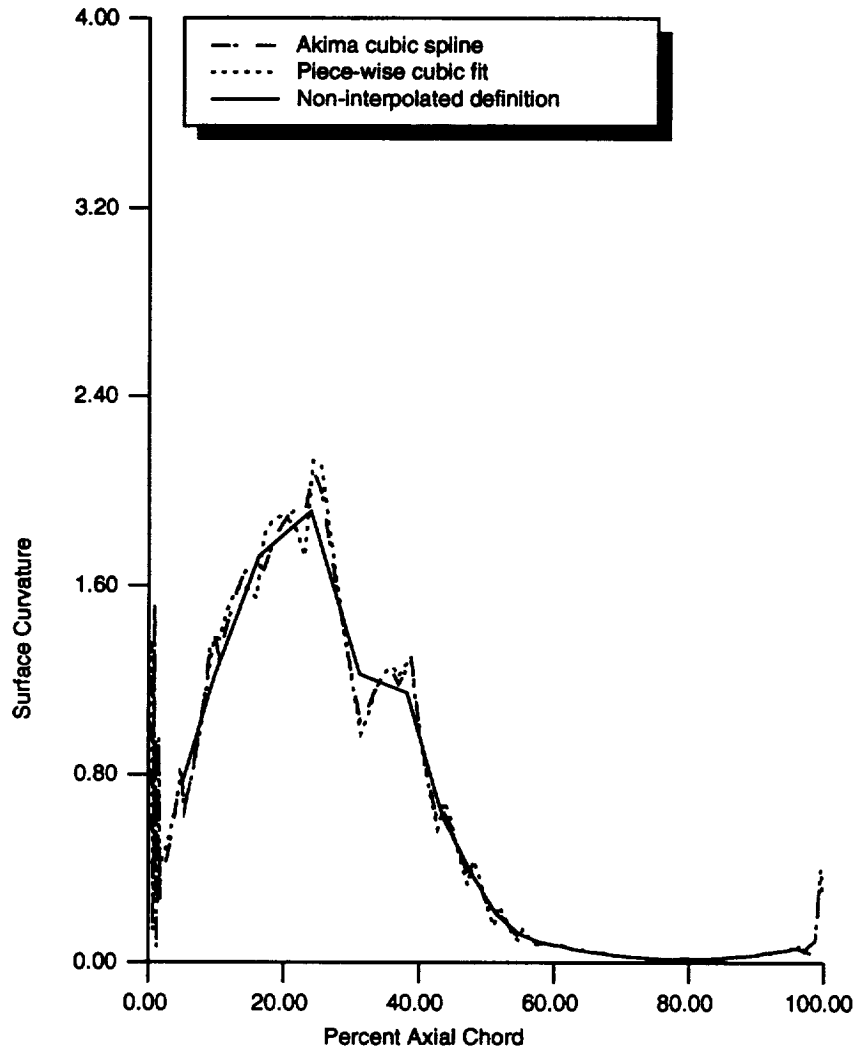


Figure 5.2: Comparison of Mesh Airfoil Surface Curvature for C3X Vane Cascade Illustrating Suction Surface Curvature Discontinuity.

*C3X Airfoil Cascade Run 4400 (Uncooled, $M_{exit}=0.90, Re_2=2E6$)
ADPAC 2-D Aerodynamic Analysis
Airfoil Surface Static Pressure Ratio Distribution*

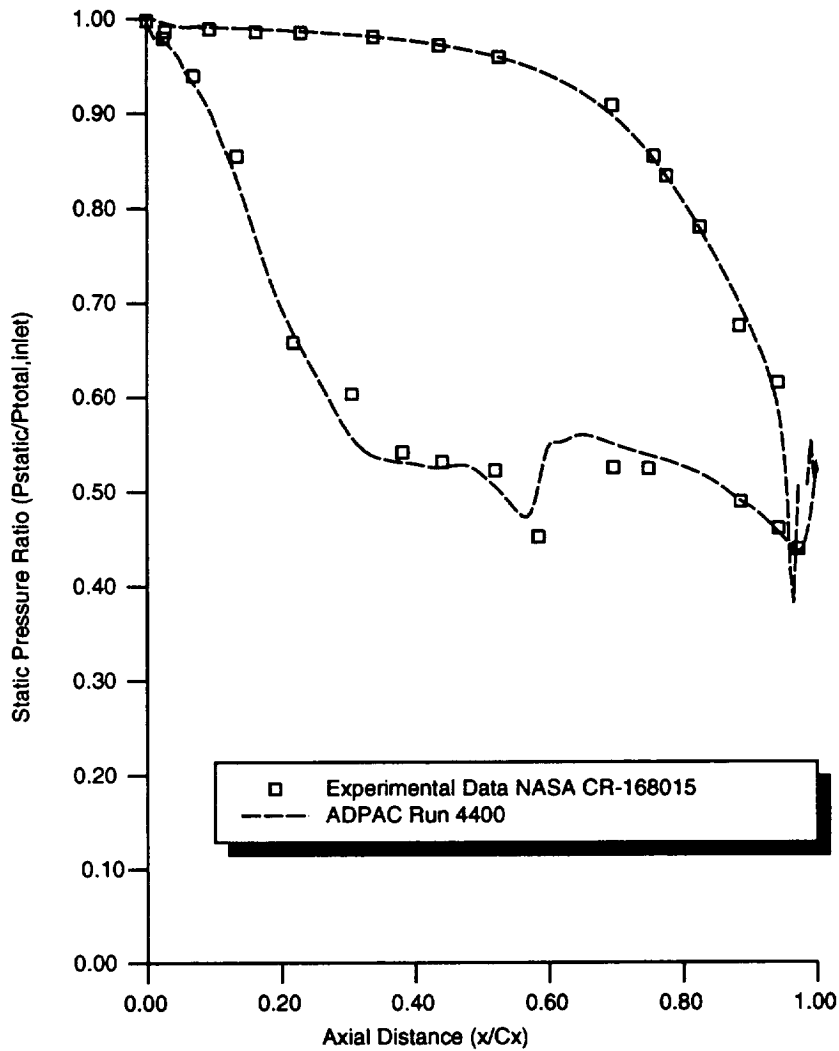


Figure 5.3: Comparison of Predicted and Experimental Airfoil Surface Static Pressure Distributions for the C3X Vane Cascade Illustrating Improved Suction Surface Pressure Distribution Due to Smoothed Airfoil Surface Geometry.

***C3X Vane
Suction Surface Curvatures***

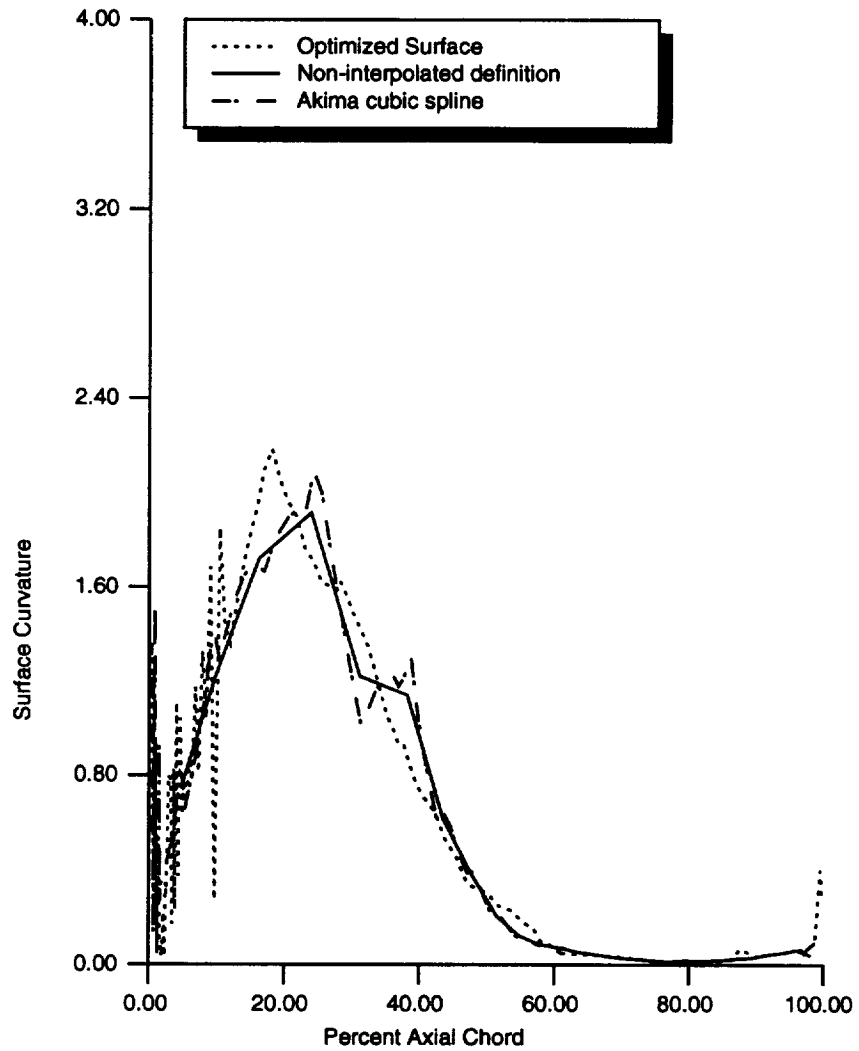


Figure 5.4: Comparison of Mesh Airfoil Surface Curvature for C3X Vane Cascade Illustrating Improved Suction Surface Curvature Distribution.

C3X vane geometry. A series of five meshes with increasing mesh density were analyzed at identical flow conditions, and predicted airfoil surface static pressure distributions and heat transfer coefficient distributions were compared to determine the minimum mesh density required for mesh-independent heat transfer results. This minimum mesh density was then later applied to predict additional flow cases for the C3X airfoil cascade. The flow conditions selected for this study correspond to Run 4411 of the C3X airfoil described in Reference [2]. The exit Mach number is 0.90, inlet total pressure and total temperature were 46.34 psia and 1415 degrees R, respectively.

Details of the five meshes employed in the mesh dependence study are presented in Table 5.2. The first two meshes were designed to increase both the number of normal (mesh lines around the airfoil) and the number of contour (mesh lines away from the airfoil) mesh lines used in the C-type mesh. The third, fourth, and fifth meshes increased the number of contour mesh lines only. Each increase in the number of contour mesh lines was accompanied by a reduction in the minimum spacing employed between adjacent contours at the airfoil surface. Graphical illustrations of the five mesh systems are presented in Figures 5.5-5.9 along with the predicted Mach number contours for a transitional flow. Each mesh was generated such that 3 levels of multigrid were available to the *ADPAC08* during execution. Each run for all five meshes were performed by using the full multigrid initialization procedure, using 100 iterations on each coarse mesh level, followed by 300 iterations on the fine mesh. The frozen turbulence model strategy described earlier for the Mark II vane cascade mesh dependence study was not employed in this series of calculations.

The following paragraphs describe results from the C3X vane cascade mesh dependence study. All 2-D flow calculations for the C3X were based on transitional flow. Calculations based on transitional flow for the C3X vane cascade employed the C-type mesh turbulence modeling scheme described in Section 3.5. The pressure surface was treated as fully turbulent, while the suction surface assumed a natural transition based on the Baldwin and Lomax [23] transition parameter (C_μ) value of 14.0.

A comparison of the convergence histories (in the form of log 10 RMS residual summations) are provided in Figure 5.10. No significant differences were observed in the convergence histories for the various meshes. Each mesh clearly displayed a full four order of magnitude reduction in the residuals for each case.

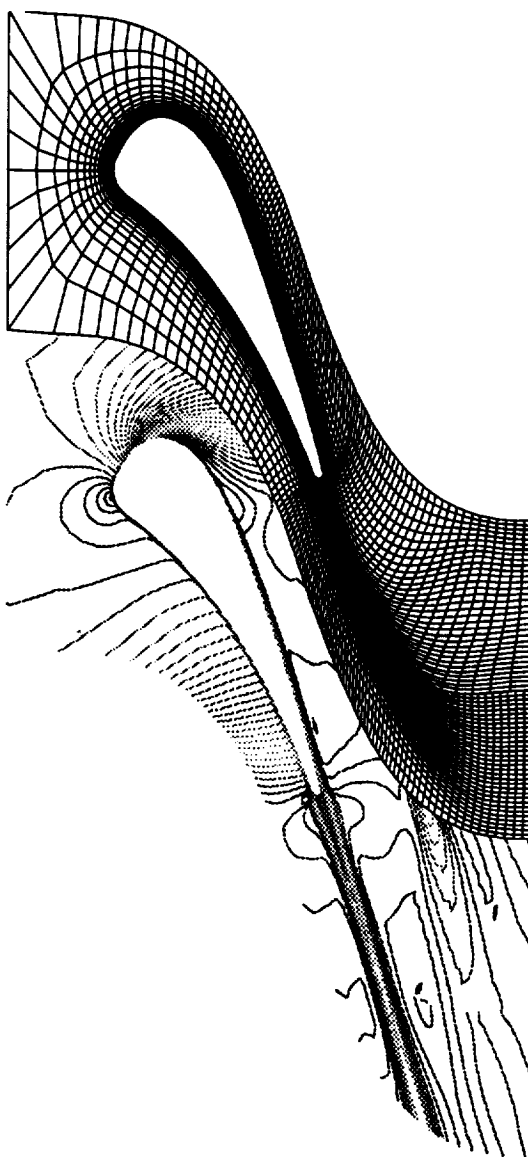


**Figure 5.5: C3X Vane Cascade Mesh Dependence Study - Mesh #1 (193x33)
Mesh System and Predicted Mach Number Contours**



**Figure 5.6: C3X Vane Cascade Mesh Dependence Study - Mesh #2 (385x49)
Mesh System and Predicted Mach Number Contours**



**Figure 5.7: C3X Vane Cascade Mesh Dependence Study - Mesh #3 (385x65)
Mesh System and Predicted Mach Number Contours**



**Figure 5.8: C3X Vane Cascade Mesh Dependence Study - Mesh #4 (385x81)
Mesh System and Predicted Mach Number Contours**



**Figure 5.9: C3X Vane Cascade Mesh Dependence Study - Mesh #5 (385x97)
Mesh System and Predicted Mach Number Contours**

C3X Vane Cascade Mesh Dependence Study Mesh Geometric Parameters

Mesh	Size	Normal Mesh Spacing at Airfoil Surface ¹	# Pts. S.S.	# Pts. P.S.
Mesh #1	193x33	0.000100	64	32
Mesh #2	385x49	0.000050	128	64
Mesh #3	385x65	0.000010	144	72
Mesh #4	385x81	0.000005	144	72
Mesh #5	385x97	0.000001	144	72

1 – normalized by airfoil axial chord

Table 5.2: C3X Vane Cascade Mesh Dependence Study Mesh Parameters)

Comparisons of the predicted and experimental airfoil surface static pressure ratio distributions for the transitional flow calculations are given in Figure 5.11 for the 5 meshes generated for the mesh dependence study. The predicted pressure distributions are in excellent agreement with the experimental measurements for every mesh. Comparisons of the transitional predicted and experimental airfoil surface heat transfer coefficient distributions are given in Figure 5.12. The pressure surface predictions are generally higher than the experimental data over most of the pressure surface. The experimental data for the suction surface indicate a finite length transition region which is not adequately represented by the *ADPAC08* point transition model. As a result, the *ADPAC08* heat transfer coefficient distributions are rather high immediately downstream of the transition point, while the experimental data suggest a more gradual rise in heat transfer coefficient. It appears that the heat transfer predictions from Meshes #3, #4, and #5, are very nearly mesh independent, and this observation ultimately led to the conclusions regarding mesh independent heat transfer predictions described in the next paragraph.

The near airfoil surface y^+ distributions for the transitional flow calculations on the five meshes are compared in Figure 5.13. For heat transfer

applications, it is normally recommended that a minimum y^+ value of 3.0 or less be maintained for the near airfoil surface mesh to achieve accurate heat transfer results. Meshes #3, #4, and #5 satisfy this criteria, and the predicted heat transfer results would appear to confirm the accuracy of this measure.

5.4 C3X Vane 2-D Heat Transfer Operating Point Study

Following the mesh dependence study, two mesh systems were constructed and evaluated for four different cascade operating points for the C3X cascade. The intention here was to evaluate predictions for the C3X vane cascade for two different exit Mach numbers (0.9, 1.05) and two different exit flow Reynolds numbers (2,000,000 and 2,500,500). The coarsest mesh system used was the 193x33 mesh illustrated in Figure 5.14. This mesh incorporates 97 points about the airfoil and has a near wall mesh spacing of 10^{-4} inches. A finer mesh (497x65) was also utilized in this study and is illustrated in Figure 5.15. This mesh was obtained by extracting a single spanwise slice from the 3-D mesh generated for the film cooling flow predictions described in Chapter 6. This mesh utilizes 383 point points about the airfoil and has a near wall mesh spacing of 1.0×10^{-5} inches. Many of the points along the airfoil surface are clustered around the leading edge due to the presence of the film cooling holes in the original 3-D mesh (see Chapter 6). The computed near airfoil surface mesh distributions of y^+ for the two meshes for the C3X airfoil operating point study are plotted in Figure 5.16 for a flow Mach number of 0.9, and exit flow Reynolds number of 2,000,000. The finer mesh clearly satisfies the $y^+ < 3$ criteria over the entire airfoil surface, while the coarser mesh does not. It is therefore expected that the results for the finer mesh are probably representative of the mesh independent result.

The cascade operating points used in the comparisons for the C3X vane are given in Table 5.3. The C3X results are categorized based on the exit Mach number (either 0.9 or 1.05). Calculations for both exit Mach number case were performed for two Reynolds numbers (2,000,000 and 2,500,000) as shown in Table 5.3. The coarse mesh calculations utilized three levels of multigrid, and the full multigrid initialization procedure. Convergence

C3X Airfoil Cascade (Uncooled, $M_{exit}=0.90, Re_2=1.99E6$)
ADPAC 2-D Aerodynamic Analysis Mesh Dependence Study (Transitional Flow)
Convergence History Comparison

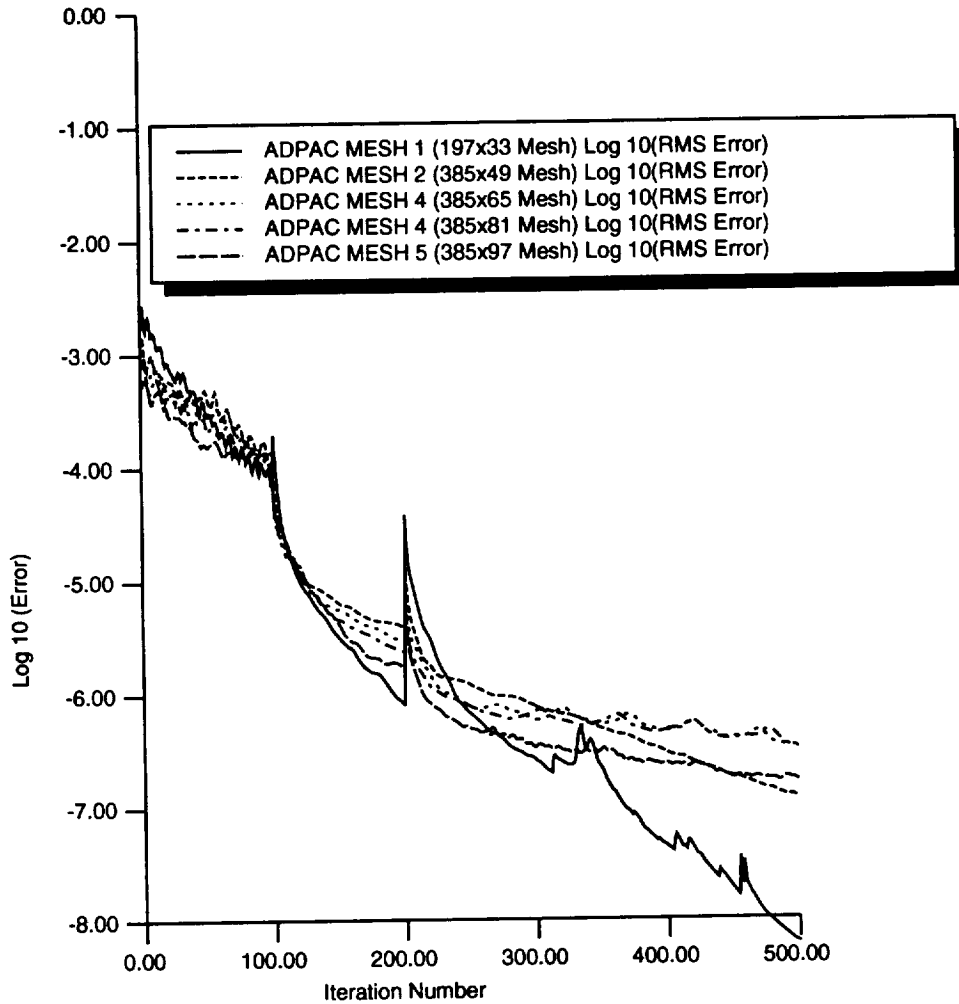


Figure 5.10: C3X Vane Cascade Mesh Dependence Study Convergence History Comparison

**C3X Airfoil Cascade (Uncooled, $M_{exit}=0.90, Re_2=1.99E6$)
ADPAC 2-D aerodynamic Analysis Mesh Dependence Study (Transitional Flow)
Airfoil Surface Static Pressure Ratio Distribution**

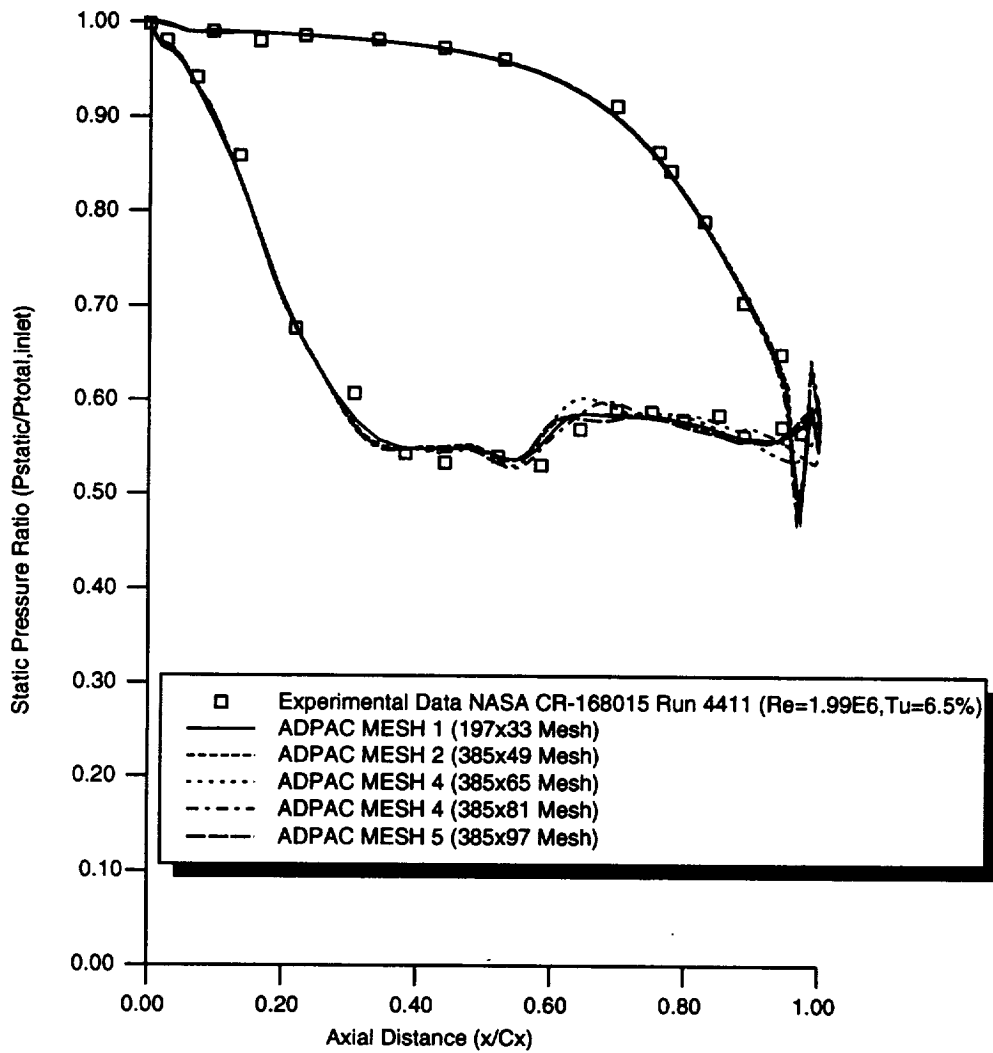


Figure 5.11: C3X Vane Cascade Mesh Dependence Study - Comparison of Predicted (Transitional Flow) and Experimental Airfoil Surface Static Pressure Ratio Distributions.

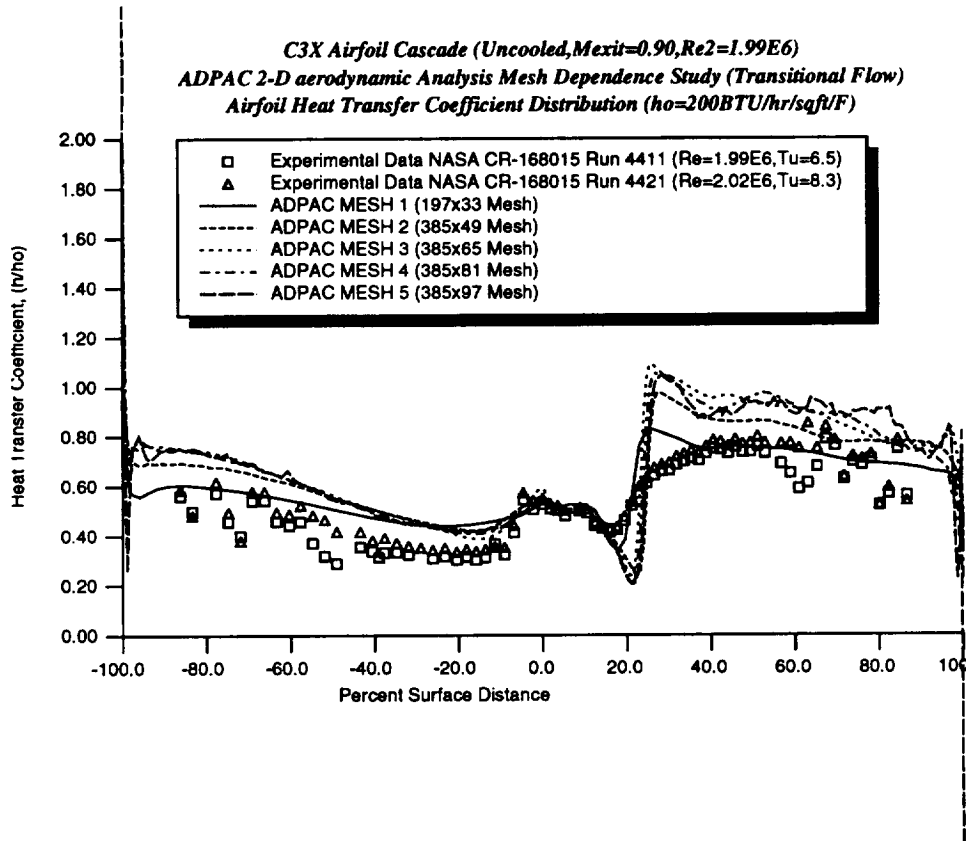


Figure 5.12: C3X Vane Cascade Mesh Dependence Study - Comparison of Predicted (Transitional Flow) and Experimental Airfoil Surface Heat Transfer Coefficient Distributions.

**C3X Airfoil Cascade (Uncooled, $Mach=0.90, Re_2=1.99E6$)
 ADPAC 2-D Aerodynamic Analysis Mesh Dependence Study (Transitional Flow)
 Near Airfoil Surface Mesh y^+ Value**

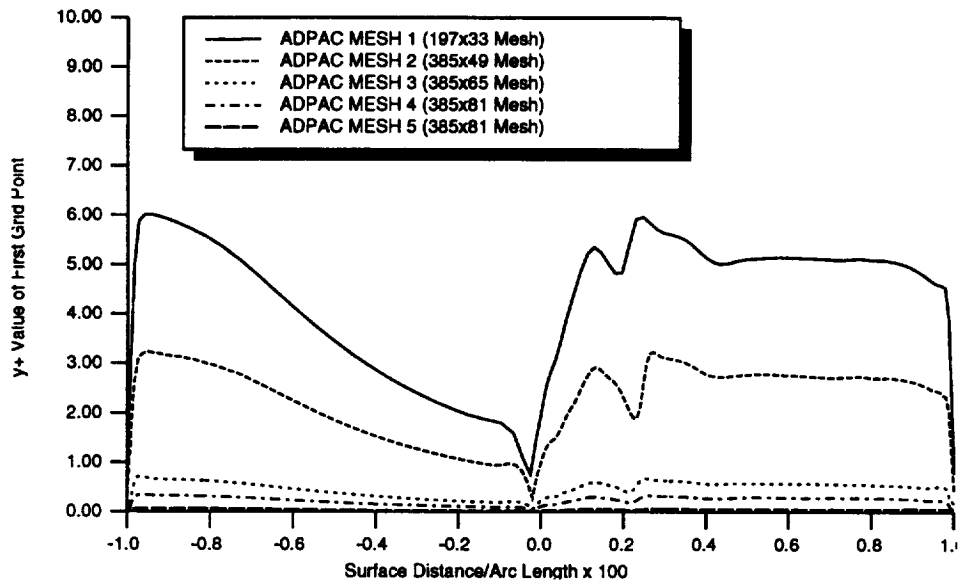


Figure 5.13: C3X Vane Cascade Mesh Dependence Study - Comparison of Predicted (Transitional Flow) Near Airfoil Surface Mesh y^+ Values.

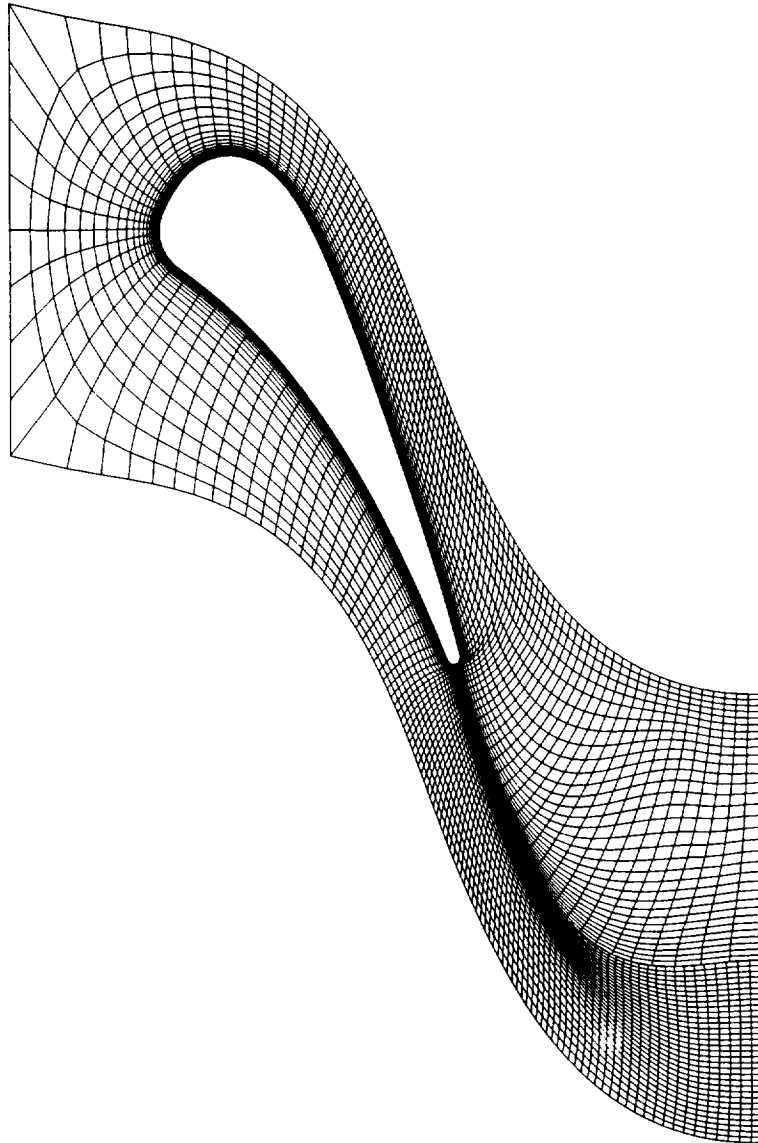


Figure 5.14: C3X Vane Cascade 193x33 2-D C-Grid Mesh System

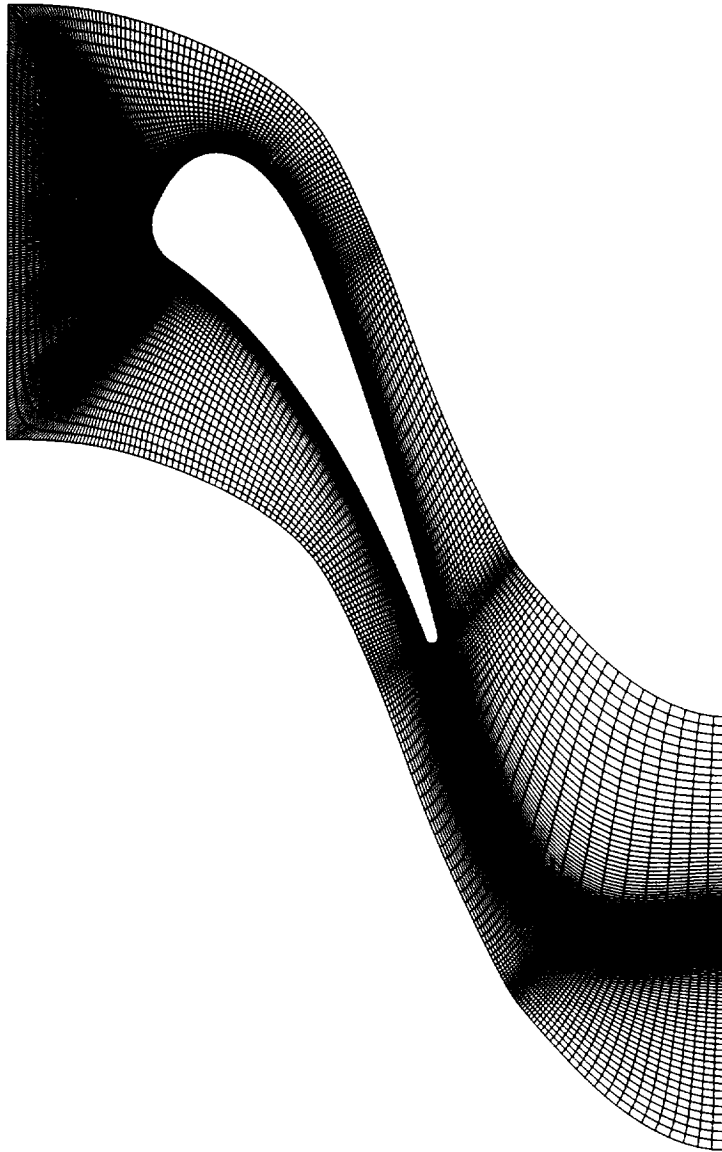


Figure 5.15: C3X Vane Cascade Operating Point Study 497x65 2-D C-Grid Mesh System

**C3X Airfoil Cascade NASA CR-174827 Run 4400 (Uncooled, $Mach=0.90, Re=1.99E6$)
 ADPAC 2-D Aerodynamic Analysis
 Airfoil y^+ Value**

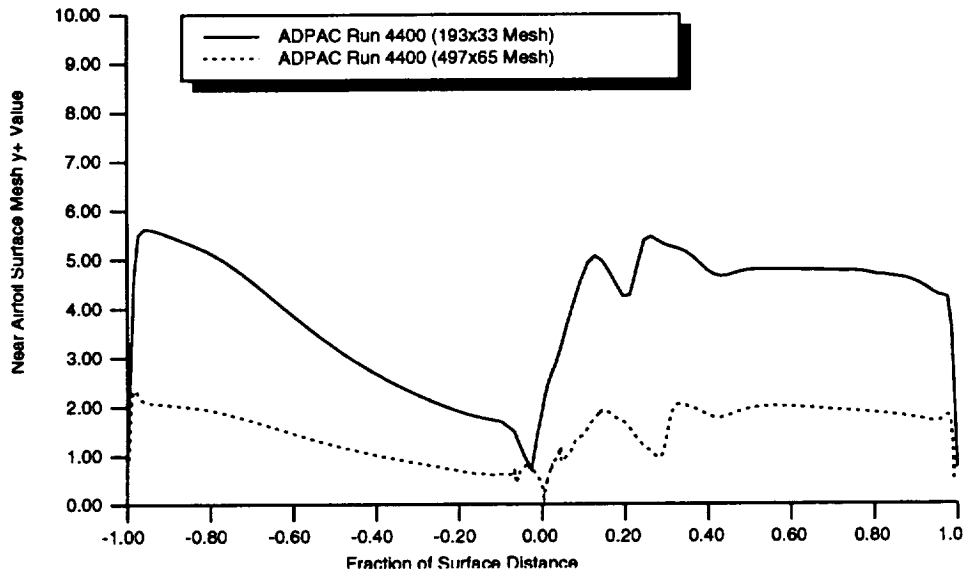


Figure 5.16: C3X Vane Cascade Operating Point Study 2-D C-Grid Mesh System Airfoil Surface y^+ Values

C3X Turbine Vane Flow Conditions for ADPAC Code Verification

	Run Code ¹	Exit Mach	Exit Re	Tc/Tg	Pc/Pg	Tw/Tg	Pt1 ²	Tt1 ³	Coolant Flow ⁴
Uncooled	4400	0.90	1.99E+06			0.78	5711.04	1236.0	
	5400	1.05	2.00E+06			0.76	5598.72	1247.0	
	4500	0.89	2.49E+06			0.81	7220.16	1245.0	
	5500	1.05	2.49E+06			0.79	6923.52	1244.0	
Cooled	4415	0.90	1.99E+06	(min) 0.71	1.100	0.77	5757.12	1243.0	0.0133
	4417	0.90	2.00E+06	(min) 0.66	1.501	0.76	5785.92	1245.0	0.0304
	4435	0.89	1.99E+06	(max) 0.86	1.099	0.77	5770.08	1244.0	0.0094
	4437	0.90	2.00E+06	(max) 0.90	1.505	0.79	5760.00	1243.0	0.0187

1 - Run Code taken from NASA CR-174827

Tu = 6.5%

2 - Pounds per square foot

3 - Degrees Rankine

4 - Pounds per second

Table 5.3: C3X Vane Cascade Calculation Operating Point Description

was observed to be very stable and uniform for each case, and a three order reduction in the solution residual is achieved after a total of 300 iterations (100 on each coarse mesh level followed by 100 fine mesh iterations). The fine mesh utilized 5 levels of multigrid, and followed a similar pattern of coarse and fine mesh iterations. A comparison of convergence histories for the two meshes for the case corresponding to Run #4400 described on Table 5.3 is given on Figure 5.17. Both solutions achieved a nearly 6 order of magnitude reduction in the RMS residual. A similar convergence behavior was observed for all other runs for the C3X airfoil, and therefore, additional convergence histories will not be presented for each case.

Comparisons of predicted and experimental airfoil surface static pressure distributions and airfoil surface heat transfer coefficient distributions for Run #4400 of the C3X airfoil at an exit Mach number of 0.9 and exit flow Reynolds numbers of 2,000,000 (based on true chord) are given in Figures 5.18 and 5.19, respectively. Both the coarse (193x33) and fine (497x65) mesh predictions are plotted on each figure.

Both the fine and coarse mesh solutions accurately capture the airfoil surface static pressure ratio distribution, and outstanding agreement with the experimental static pressure distributions was achieved. The predicted heat transfer distributions were also found to be in very good agreement with the experimental data in spite of the rather poor representation of the apparent finite length transition process indicated by the experimental data. The

**C3X Airfoil Cascade NASA CR174827 Run 4400 (Uncooled, Mexit=0.90, Re2=1.99E6)
ADPAC 2-D Aerodynamic Analysis
Convergence History Comparison**

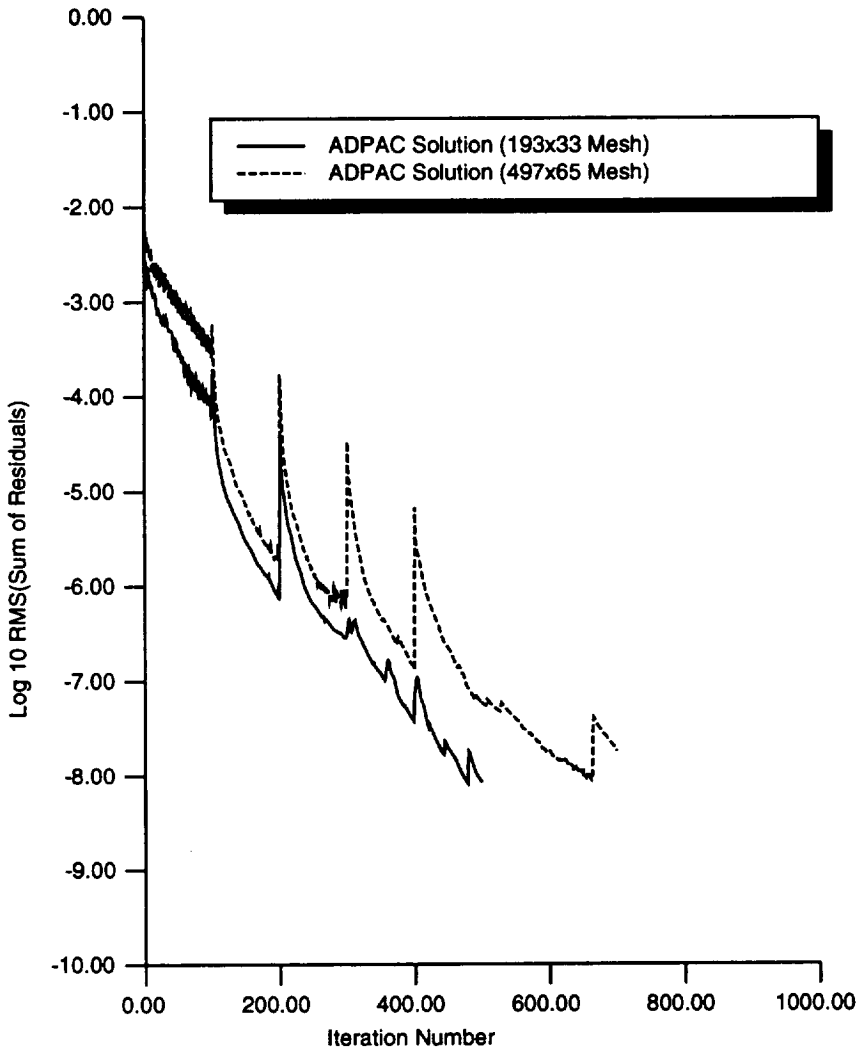


Figure 5.17: C3X Vane Cascade Operating Point Study Convergence History Comparison

C3X Airfoil Cascade NASA CR174827 Run 4400 (Uncooled, $M_{exit}=0.90, Re_2=1.99E6$)
ADPAC 2-D Aerodynamic Analysis
Airfoil Surface Static Pressure Ratio Distribution

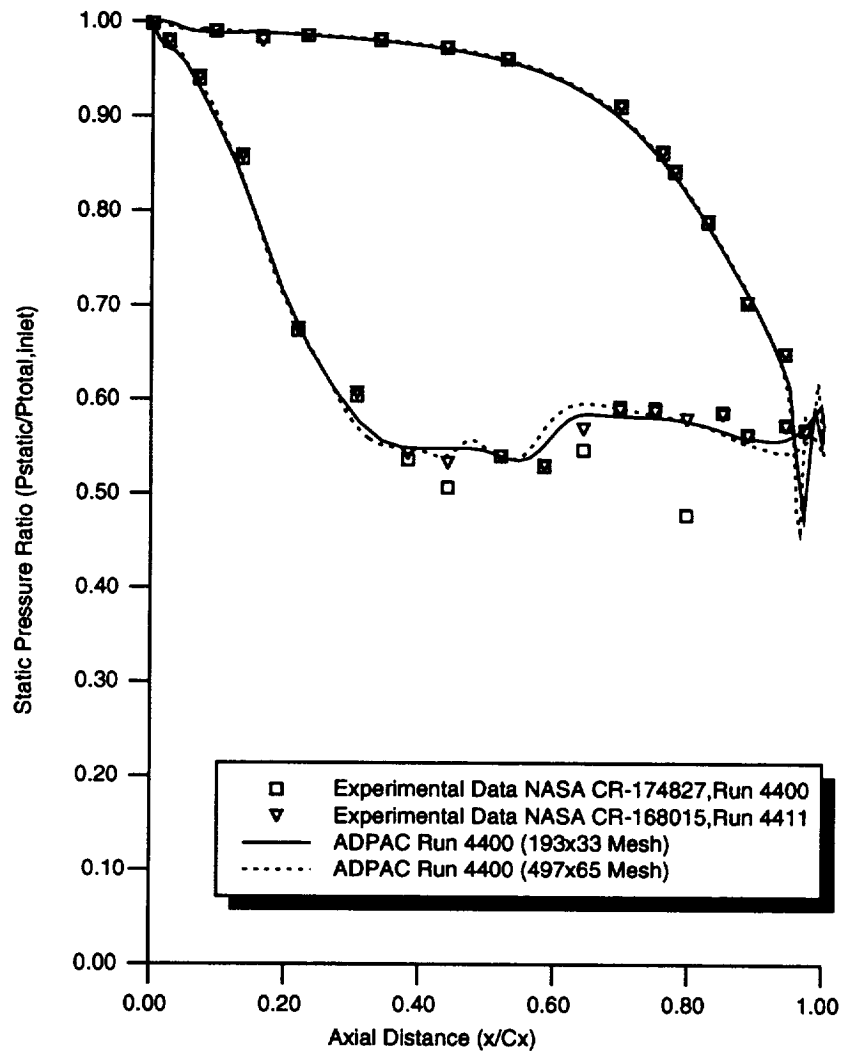


Figure 5.18: Comparison of Predicted and Experimental Airfoil Surface Static Pressure Ratio Distributions for C3X Vane Cascade Operating Point Study (Run #4400, $M_2=0.9$, $Re_2=2,000,000$)

**C3X Airfoil Cascade NASA CR-174827 Run 4400 (Uncooled, $M_{exit}=0.90, Re_2=1.99E6$)
 ADPAC 2-D Aerodynamic Analysis
 Airfoil Heat Transfer Coefficient Distribution ($h_o=200\text{BTU/hr/sgf/F}$)**

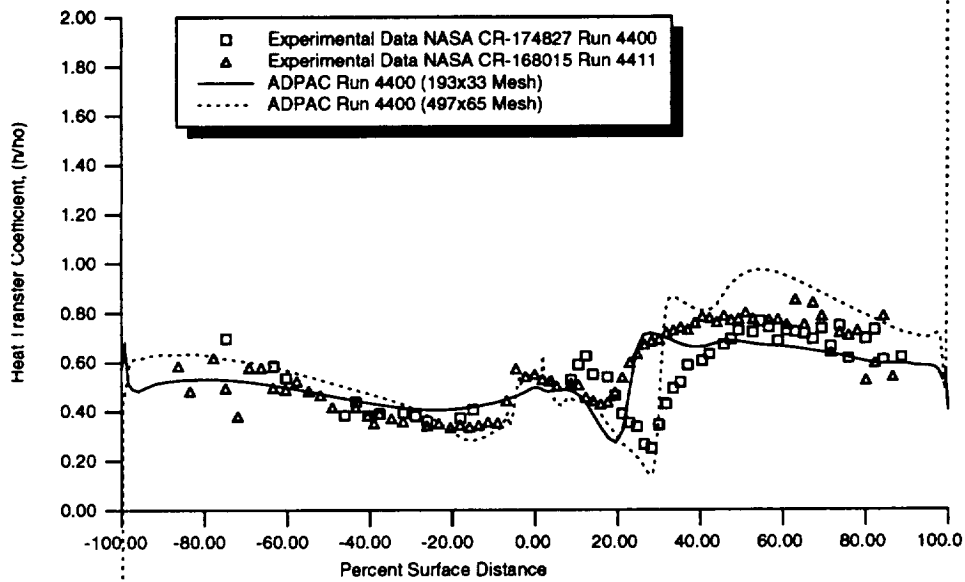


Figure 5.19: Comparison of Predicted and Experimental Airfoil Surface Heat Transfer Coefficient Distributions for C3X Vane Cascade Operating Point Study (Run #4400, $M_2=0.9$, $Re_2=2,000,000$)

**C3X Airfoil Cascade NASA CR-174827 Run 4500 (Uncooled, $M_{exit}=0.89, Re_2=2.49E6$)
ADPAC 2-D Aerodynamic Analysis
Airfoil Surface Static Pressure Ratio Distribution**

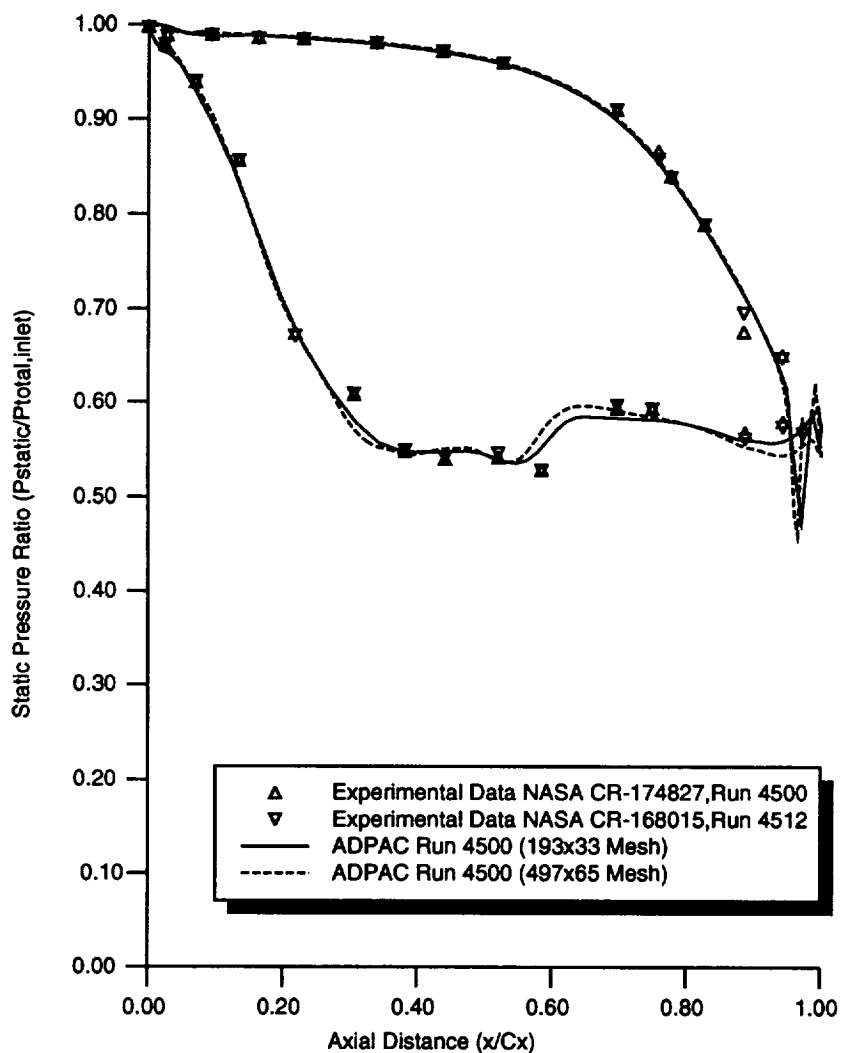


Figure 5.20: Comparison of Predicted and Experimental Airfoil Surface Static Pressure Ratio Distributions for C3X Vane Cascade Operating Point Study (Run #4500, $M_2=0.90, Re_2=2,500,000$)

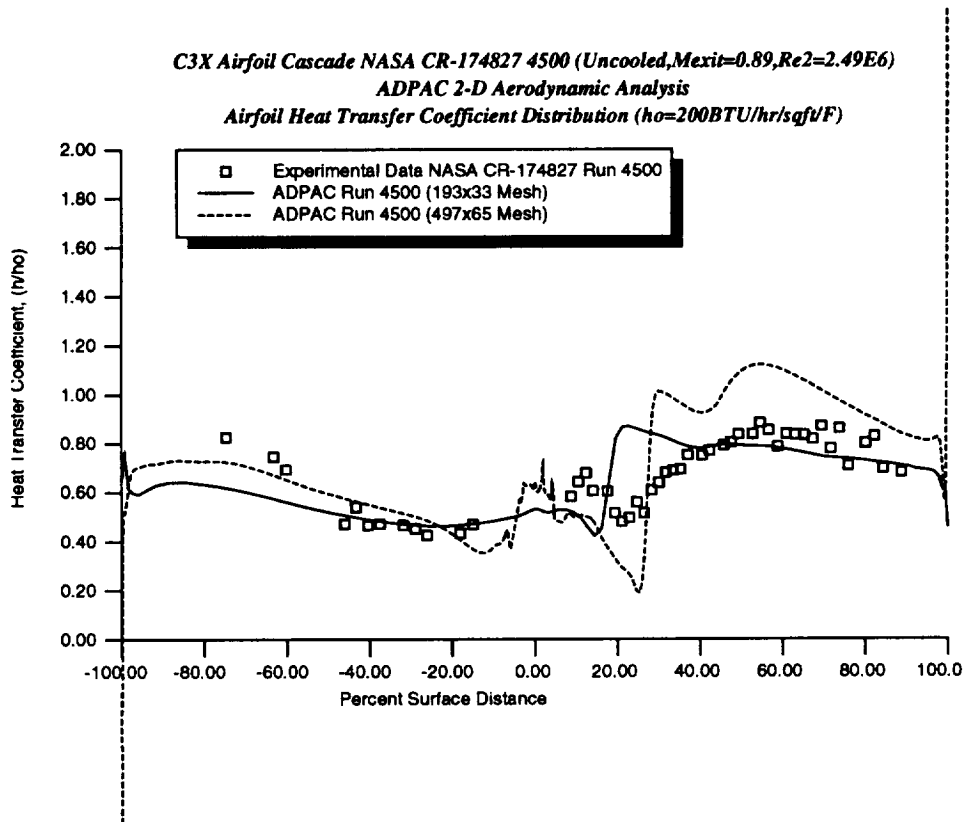


Figure 5.21: Comparison of Predicted and Experimental Airfoil Surface Heat Transfer Coefficient Distributions for C3X Vane Cascade Operating Point Study (Run #4500, $M_2=0.90, Re_2=2,500,000$)

C3X Airfoil Cascade NASA CR-174827 Run 5400 (Uncooled, $M_{exit}=1.05, Re_2=2.00E6$)
ADPAC 2-D Aerodynamic Analysis
Airfoil Surface Static Pressure Ratio Distribution

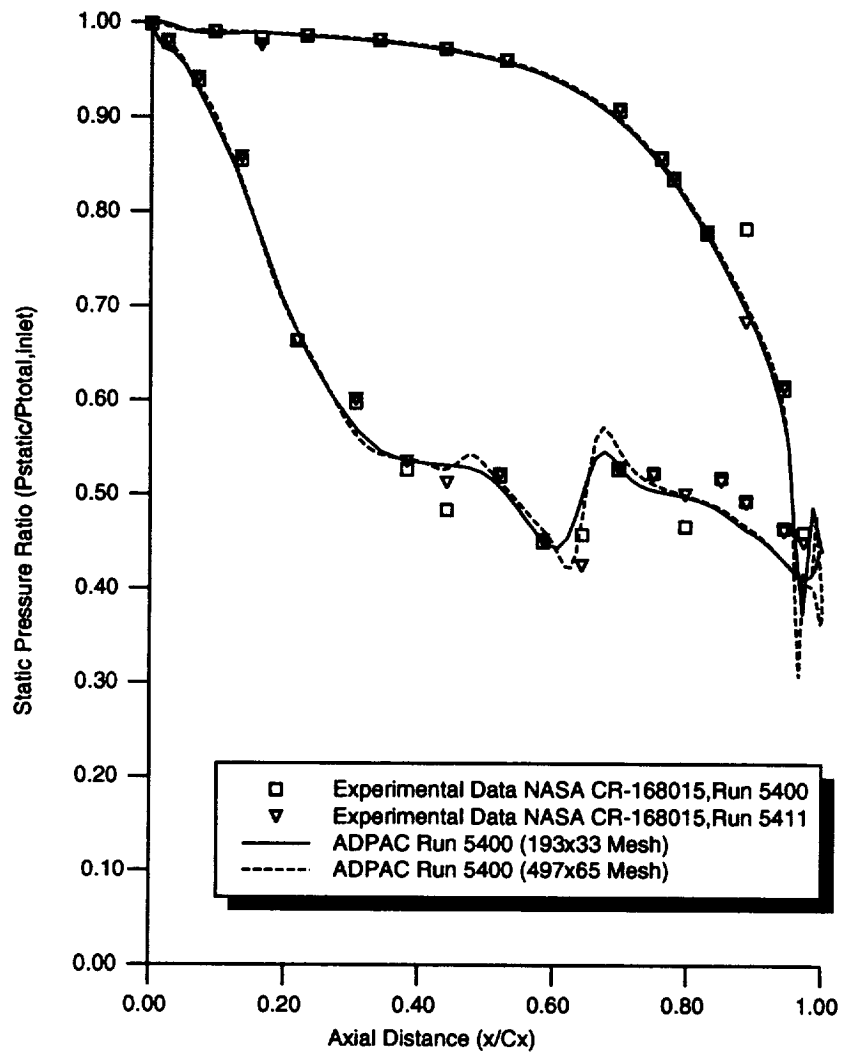


Figure 5.22: Comparison of Predicted and Experimental Airfoil Surface Static Pressure Ratio Distributions for C3X Vane Cascade Operating Point Study (Run #5400, $M_2=1.05, Re_2=2,000,000$)

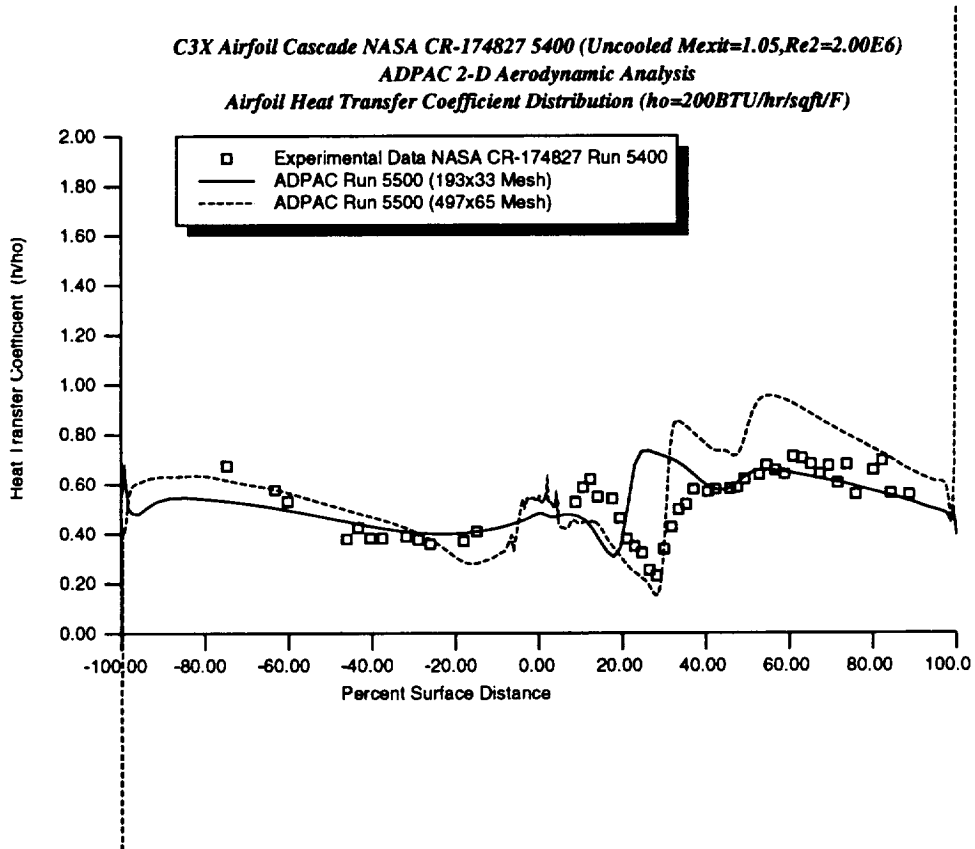


Figure 5.23: Comparison of Predicted and Experimental Airfoil Surface Heat Transfer Coefficient Distributions for C3X Vane Cascade Operating Point Study (Run #5400, $M_2=1.05$, $Re_2=2,000,000$)

C3X Airfoil Cascade NASA CR-174827 Run 5500 (Uncooled, $M_{exit}=1.05, Re_2=2.49E6$)
ADPAC 2-D Aerodynamic Analysis
Airfoil Surface Static Pressure Ratio Distribution

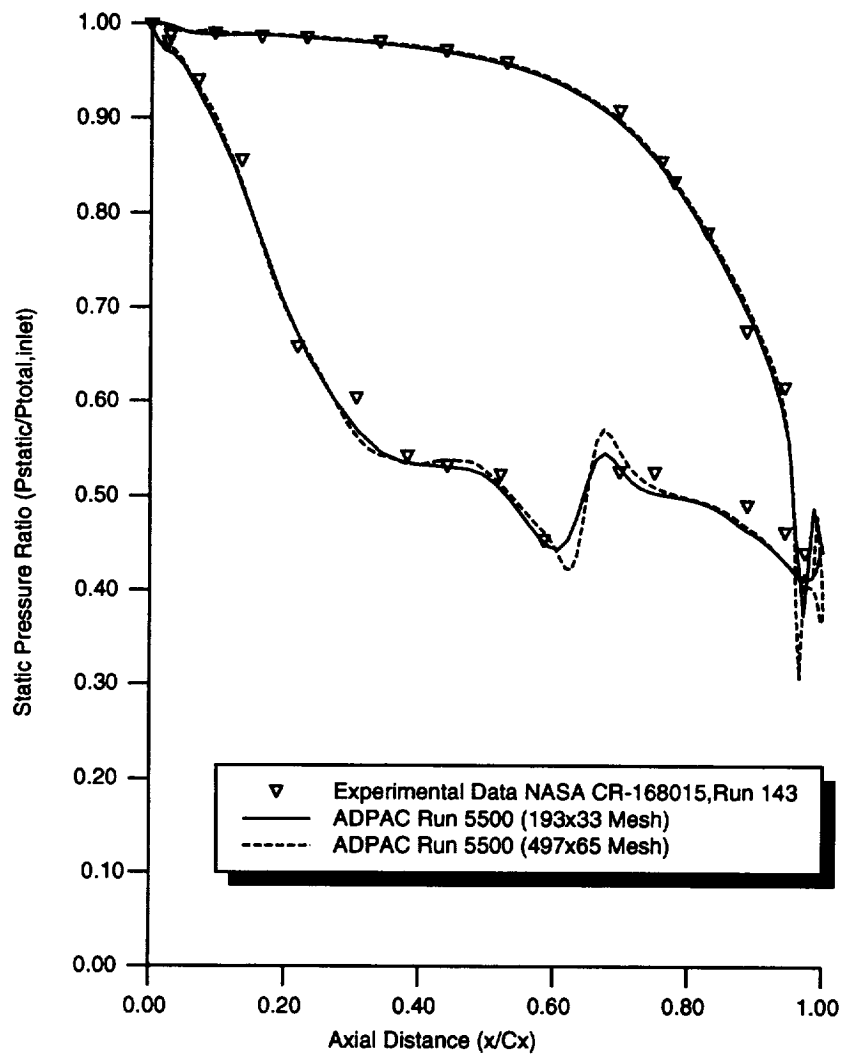


Figure 5.24: Comparison of Predicted and Experimental Airfoil Surface Static Pressure Ratio Distributions for C3X Vane Cascade Operating Point Study (Run #5500, $M_2=1.05, Re_2=2,500,000$)

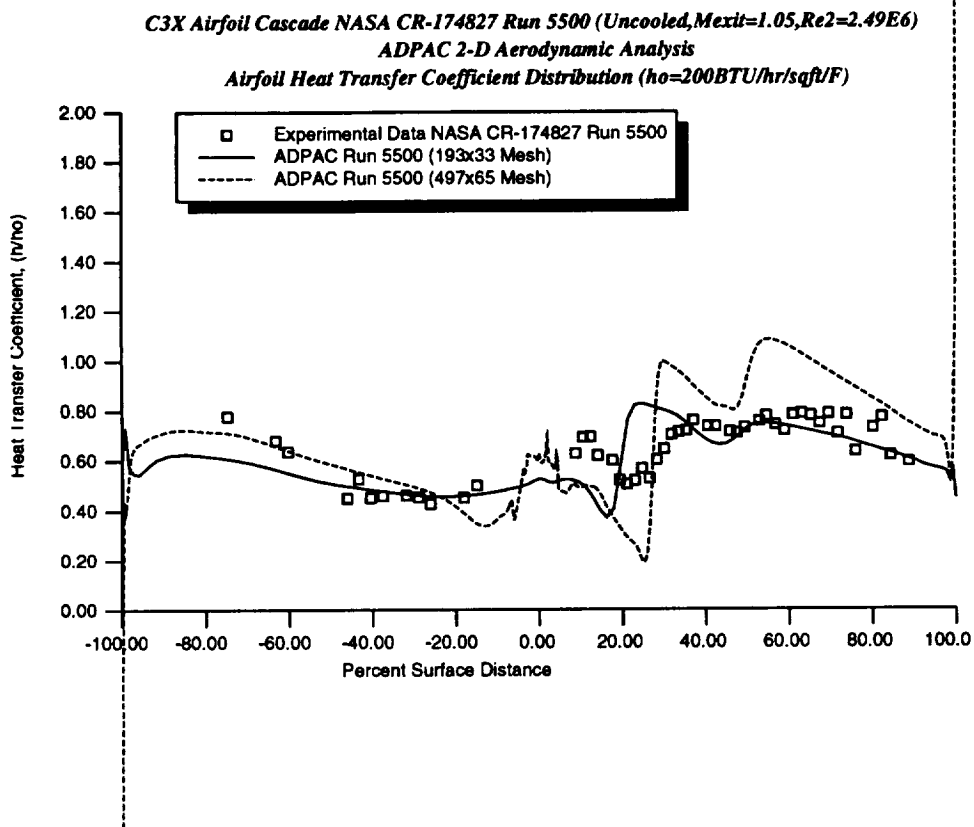


Figure 5.25: Comparison of Predicted and Experimental Airfoil Surface Heat Transfer Coefficient Distributions for C3X Vane Cascade Operating Point Study (Run #5500, $M_2=1.05, Re_2=2,500,000$)

absolute levels of heat transfer downstream of the leading edge and transition regions are generally overpredicted. There are substantial differences between the coarse and fine grid heat transfer coefficient distributions. In fact, the coarse grid results appear to match the experimental data better than the fine mesh results. Without the benefit of the mesh dependence study, the accuracy of the analysis might have been overestimated based on the coarse mesh data alone. The important consideration here is to only interpret and draw conclusions about any analysis after the mesh dependence of the solution has been established.

Comparisons of predicted and experimental airfoil surface static pressure distributions and airfoil surface heat transfer coefficient distributions for Run #4500 of the C3X airfoil at an exit Mach number of 0.9 and exit flow Reynolds numbers of 2,500,000 (based on true chord) are given in Figures 5.20 and 5.21, respectively. This solution permits an examination on the effects of changing Reynolds number for a constant exit Mach number. No significant change in airfoil static pressure distributions resulted from the change in Reynolds number when compared to the results for Run #4400. Airfoil surface heat transfer coefficient levels are somewhat higher, and it again appears that the analysis accurately captures the effective change in heat transfer due to change in Reynolds number in spite of the general overprediction of heat transfer levels.

Comparisons of predicted and experimental airfoil surface static pressure distributions and airfoil surface heat transfer coefficient distributions for Run #5400 of the C3X airfoil at an exit Mach number of 1.05 and exit flow Reynolds number based on true chord of 2,000,000 are given in Figures 5.22 and 5.23, respectively. Comparison with the results from Run #4400 now permit an analysis of the effects of increasing the exit flow Mach number for a constant Reynolds number. Once again, the agreement between experiment and prediction is very good, and the same trends observed in the 0.9 exit Mach number case were found in the 1.05 Mach number cases. Comparisons of predicted and experimental airfoil surface static pressure distributions and airfoil surface heat transfer coefficient distributions for Run #5500 of the C3X airfoil at an exit Mach number of 1.05 and exit flow Reynolds numbers of 2,500,000 are given in Figures 5.24 and 5.25, respectively. No significant difference were observed in the airfoil surface static pressure distributions at Reynolds numbers of 2,000,000 and 2,500,000 for the 1.05 exit Mach number results. The predicted heat transfer coefficient distributions

again display the observed experimental trend of increased heat transfer levels as Reynolds number increases. The overall agreement between prediction and experiment is thought to be very good, in spite of the known deficiencies of the *ADPAC08* turbulence model.

Again, several sources of error are present which could account for some of the differences between predicted and experimental heat transfer coefficient values. The calculations were performed with a constant airfoil surface temperature, while the experimental data shows a nontrivial variation in airfoil surface temperature. For the purposes of simplifying the calculations, a constant gas Prandtl number was employed. The solutions also assume a fully turbulent pressure surface, although the real flow situation is more likely a long, gradual transition along the pressure surface. The reported margin of error in the experimentally determined heat transfer coefficients was as large as $\pm 6.7\%$ near the leading edge, and $\pm 23.5\%$ near the airfoil trailing edge, so clearly, detailed comparisons cannot be interpreted too literally.

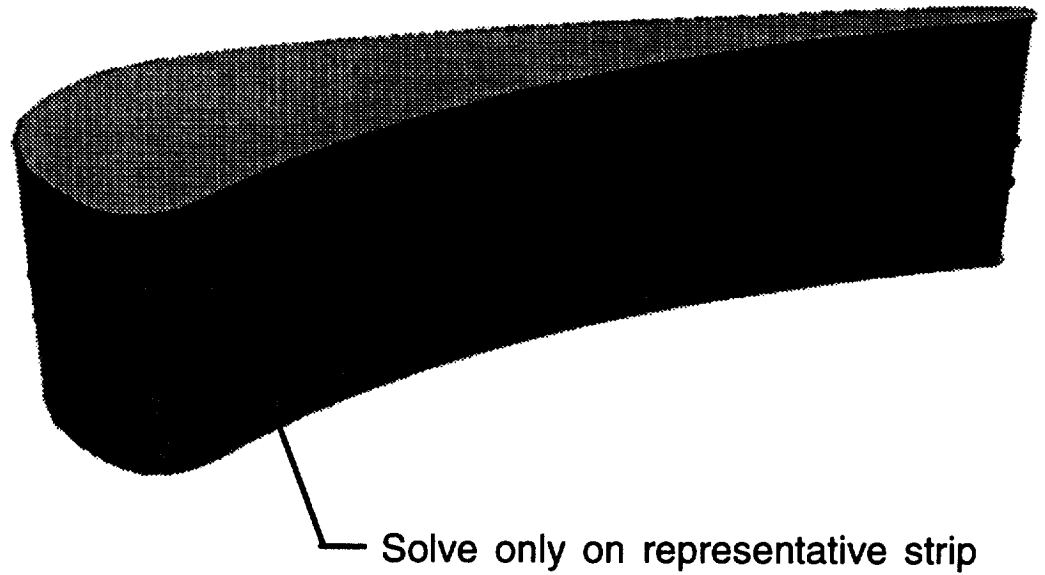
Chapter 6

C3X VANE CASCADE 3-D HEAT TRANSFER CALCULATIONS

6.1 C3X Vane Cascade Description

The C3X airfoil is an Allison-designed film cooled turbine vane, experimentally tested in a planar cascade under NASA contract (References [1],[2],[3]). The C3X airfoil is shown in Figure 6.1. The C3X geometry is representative of a first vane in a modern high pressure turbine. Film cooling is accomplished by a showerhead array of holes in the leading edge region of the airfoil (and through downstream injection sites as well [3]). The showerhead array utilizes a repeating pattern of 5 cooling holes of circular cross section which are inclined at a 45 degree angle in the spanwise direction (see Figure 6.1). The geometry is periodic in the spanwise direction, and therefore the analysis was limited to a representative spanwise strip with spatial periodicity applied to the upper and lower surfaces, respectively. This solution procedure essentially neglects endwall effects, which is felt to be negligible for the midspan flow behavior.

C3X Vane With Film Cooling Holes



Showerhead contains 5 rows of holes.

Holes are drilled at 45 degree angle with respect to Z axis.

Figure 6.1: C3X Vane With Film Cooling Holes.

6.2 C3X Vane Cascade Geometry Model

A CAD model of the C3X airfoil was generated using the (ANVIL 5000) CAD system. Each of the circular film cooling holes were projected to the airfoil surface to determine the exact shape of the airfoil/coolant hole intersections. The airfoil shape and the coolant hole shapes were ultimately splined for use in the mesh generation process. Preliminary calculations of this splined geometry utilizing very fine mesh distributions displayed noticeable oscillations in the airfoil static pressure profile as described in the previous chapter. These oscillations were ultimately traced to minute fluctuations in the airfoil surface curvature which were only discernable in meshes with high density. The final airfoil surface used in the remainder of the calculations was numerically smoothed through an optimization process to eliminate these wiggles for very fine meshes.

6.3 C3X Vane Cascade 3-D Grid Philosophy

A C-type mesh was selected in order to provide the smoothest possible grid around the leading edge, and have grid lines clustered along the expected wake path. The *ADPAC* analysis is capable of using a noncontiguous block interface, which provides a means of reducing the shear which normally occurs in O-type and C-type grids about high stagger airfoils. The drawback to noncontiguous boundaries, is that the solution is interpolated along the boundary, which can introduce small discrepancies at the boundary. In a C-type grid, there are two periodic grid boundaries: one between the airfoils (referred to as the periodic boundary), and one along the wake boundary (referred to as the cut line). Either of these boundaries could be noncontiguous, but the cut line was chosen because the downstream flow is of less interest than the flow in the passage.

In order to take advantage of the multigrid flow solver in the *ADPAC* code, the overall grid size was chosen to enable a multilevel multigrid solution. The grid was generated with the understanding that the mesh index for each important geometric feature must be a “multigrid number”. Multigrid numbers are numbers such that

$$\text{mod}(num + 1, 2) = 0 \tag{6.1}$$

The number of times that Equation 6.1 can be recursively applied plus 1 is the number of multigrid levels possible for that number. Generally, three levels of multigrid was found to be sufficient for good convergence acceleration. Five levels of multigrid were possible in the final mesh constructed for this analysis.

6.4 C3X Vane Cascade 3-D Grid Layout

The final grid size was $497 \times 65 \times 65$ (2,099,825 points) with a 17×17 grid patch (289 points) on each hole. The cut line is noncontiguous with 81 points on the lower side, and 33 points on the upper side. The grid layout is shown in Figure 6.2.

The grid generation procedure began by running a 2-D C-grid generator to get a general idea of how the points should be distributed to achieve adequate resolution with minimum grid shear. The intent was to examine a large number of grid layouts in a short time, without the bother of 3-dimensionality or modeling hole shapes. The *JERRYC* (Reference [15]) program was chosen because it permitted rapid generation of C-type grids with non-contiguous cut lines. The *JERRYC* code was used to get an initial guess for the number and distribution of points on the inlet boundary, the periodic boundary, and the cut line. The cut line shape found in *JerryC* was preserved in the final grid, but the periodic boundary was only used as an initial guess.

6.5 C3X Vane Cascade 3-D Grid Generation

The final grid was generated using the *GRIDGEN* (Reference [21]) program. *GRIDGEN* was chosen because it has the capability of generating multiple block grids about arbitrary shapes in three dimensions. The blade surface grid around the holes is shown in Figure 6.3 (the image is warped by the projection to 2-D).

Maintaining orthogonality and grid spacing at the blade surface also required special attention. Experience has shown that a grid spacing on the order of 0.0001 inches for the first point normal to the airfoil is adequate for heat transfer predictions for the C3X airfoil (axial chord 3.077 inches). Actual spacings in the final grid deviate from this slightly.

C3X Vane

C-Grid Point Layout

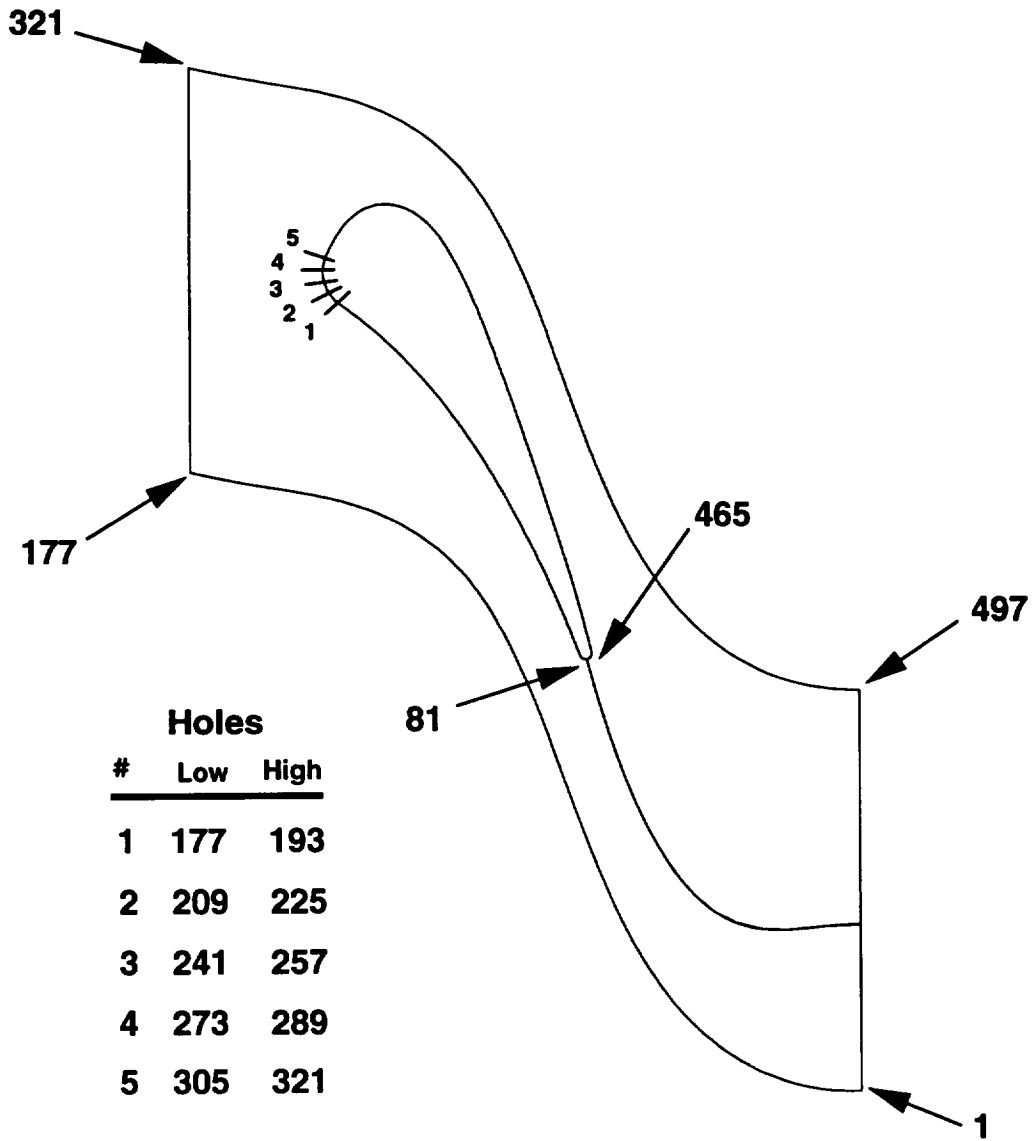
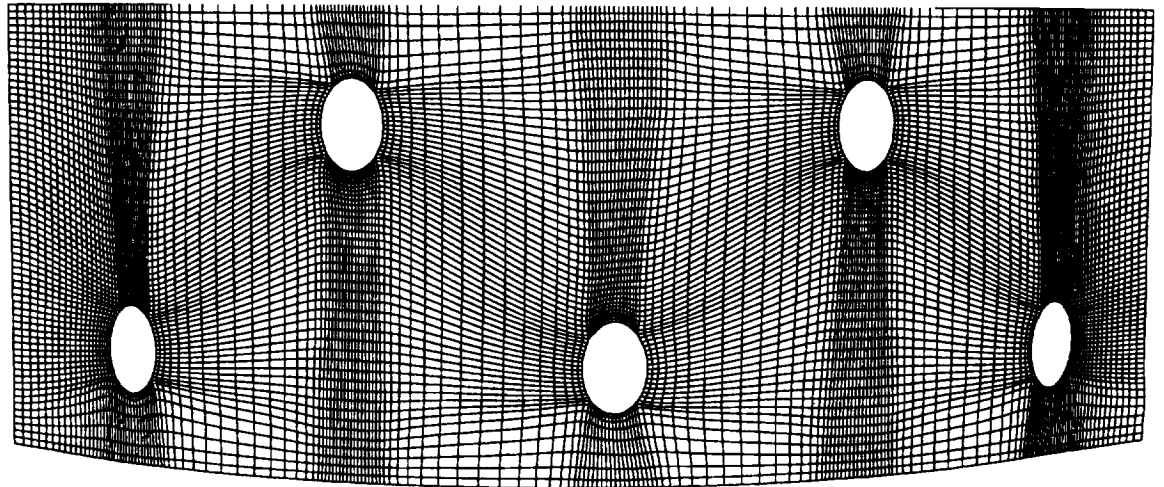


Figure 6.2: Layout of C-grid with point assignment of film cooling holes.

C3X Vane

Blade Surface Grid Around Showerhead



Note: Plot is a 2-D projection of a 3-D object. Hole shapes are not true view.

Figure 6.3: Blade surface grid around film cooling holes.

6.6 C3X Vane Cascade 3-D Uncooled Heat Transfer Predictions

Three-dimensional viscous flow analyses were performed for the C3X vane cascade at four different operating points using the *ADPAC08* Navier-Stokes analysis. The cascade operating points for the non-cooled turbine vane are listed in Figure 5.3. Preliminary calculations were performed using a reduced mesh system obtained from the full 3-D mesh system described above. The reduced mesh system was obtained by eliminating every other mesh point in each coordinate direction, reducing the airfoil C-grid mesh size from 497x65x65 to 249x33x33. The 3-D calculations on the reduced mesh utilized 3 levels of multigrid, with the full multigrid initialization procedure. The full multigrid initialization utilized 100 iterations on each of the coarser mesh levels, followed by 400 iteration on the fine mesh level. The solution typically converged approximately 3 orders of magnitude in the first 200 iterations of the fine mesh cycle.

Predicted vane surface static pressure ratio and heat transfer coefficient distributions from the reduced 3-D analysis were found to be essentially identical to the corresponding 2-D solutions presented earlier in this report and will not be presented here, but are only mentioned for completeness.

6.7 C3X Vane Cascade 3-D Film-Cooled Heat Transfer Predictions

The objectives of this study were to assess the accuracy of the *ADPAC* analysis for predicting heat transfer in film-cooled turbine airfoils, investigate aerodynamic details of discrete site cooling flows, and to attempt to define the minimum mesh requirements needed to accurately portray this type of flow. To achieve these goals, calculations were performed for the the 3-D flow about the C3X turbine vane cascade with a leading edge showerhead film cooling arrangement at a single Mach number and Reynolds number for 2 different coolant to freestream pressure ratios and 2 different coolant to freestream temperature ratios. The Mach number and Reynolds number selected for this study were 0.9 and 2,000,000, respectively. The coolant to gas temperature and pressure ratios were determined from the available experi-

mental data and are listed in Figure 5.3 along with the non-cooled turbine vane flow conditions.

Calculations for the film-cooled C3X vane were performed using two mesh systems. These mesh systems are referred to as the fine mesh and the reduced mesh. The reduced mesh was obtained from the fine mesh (the full 3-D mesh system described in the previous sections) by removing every other mesh line. In order to accurately model the velocity profile of the incoming coolant flow, additional meshes were generated to represent the internal walls of the coolant flow holes as shown in Figure 6.4. The coolant flow hole meshes are aligned with the desired coolant flow injection angle and add little to the overall cost of the calculation, while greatly simplifying the accurate application of coolant flow boundary conditions. In addition, the internal coolant channels aid by allowing a realistic coolant flow velocity profile to develop, which is important to accurately predict details of the coolant flow-primary gas flow interaction.

Film cooled calculations for the reduced mesh system again utilized 3 levels of multigrid and the same iteration strategy as described above for the non-cooled C3X turbine vane calculations.

During the course of these calculations, significantly different flow patterns were observed between the low coolant total pressure calculations and the high coolant total pressure calculations, and therefore, the results for the calculations will be presented separately based on coolant total pressure ratio. Results from both the reduced mesh and fine mesh calculations displayed similar characteristics, and, as a result, both calculations are described simultaneously in the paragraphs which follow.

The first set of calculations to be discussed are based on Run #4415 and #4435 as described in Figure 5.3. For these two calculations the coolant total pressure ratio was approximately 1.1 which results in a relatively low coolant flow (compared to the high coolant total pressure ratio calculations described later). An interesting feature of the film-cooled C3X turbine vane calculations is the interaction between the coolant flow jet and the primary vane passage flow. The predicted near-leading edge airfoil surface streamline flow pattern for Run # 4415 is illustrated in Figure 6.5. The coolant holes have been outlined for reference, with the pressure side of the airfoil on the right, and the suction side of the airfoil on the left. The rather unique flow pattern which is formed on the downwind side of each cooling hole results from the interaction between the coolant flow jet and the primary vane

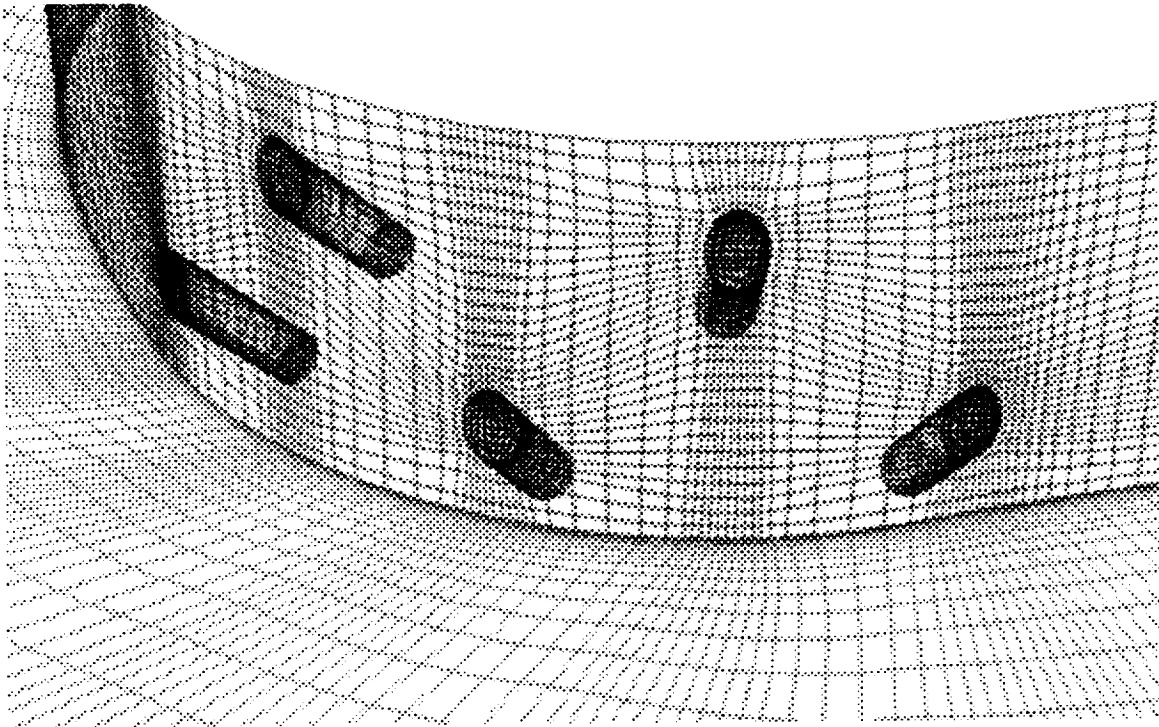


Figure 6.4: Leading edge close-up of reduced 3-D mesh system for C3X turbine vane illustrating coolant hole mesh systems

passage flowfield. As the jet emerges from the coolant hole, the shear forces resulting from the primary gas crossflow drives a pair of counterrotating vortices within the jet as well as directing the jet centerline downstream along the airfoil surface. The strong secondary flow within the jet entrains fluid near the blade surface on the downwind half of the flow causing the backflow regions observed for each cooling hole. The convergence of the shear lines downstream of each hole illustrates the effect of the secondary flow and provides a mechanism for tracking the centerline of the coolant flow jet. It is clear from this pattern that in spite of the staggered 5 hole arrangement which is repeated along the blade span, only a single cold stream results along the pressure and suction surfaces. This phenomenon is clearly a result of the merging of adjacent hole jets and suggests that alternate hole patterns might be more effective at providing a cool gas thermal layer. An attempt to graphically track the coolant flow jets is presented in Figures 6.6 and 6.7. These figures illustrate the coolant flow particle traces and predicted near airfoil surface temperature contours (indicative of heat transfer coefficient) for Run # 4415 and #4435, respectively. The coolant flow particle traces are very similar for these two calculations, with only slight differences in cooling level due to the higher coolant total temperature ratio for Run #4435. As the coolant flow jet emerges from the injection site, the relative ratios of coolant jet momentum and local primary gas flow momentum determine the trajectory of the coolant jet. For the low coolant total pressure ratio cases, the jet trajectory is influenced significantly by the local primary gas flow, and the jets on the suction side of the airfoil are immediately turned downstream with very little spanwise spreading. The two jets turned running downstream along the airfoil suction surface appear to merge into a single coolant stream, and the lack of spanwise migration results in the striping pattern illustrated by the near airfoil surface temperature contours. Due to the spanwise length of the instrumentation used in the C3X test rig, it is unlikely that the measured heat transfer coefficient data can reflect this "striping" behavior, and if, in fact, this behavior was truly present, then the experimental data could only reflect some spanwise average of the actual discrete spanwise heat transfer coefficient distributions. The comparisons between predicted and experimental heat transfer coefficient distributions for this flow must therefore be judged with this limitation in mind. Along the airfoil pressure surface, much of the near airfoil flow is essentially stagnated, and the spanwise migration of the coolant flow is relatively unimpeded. This

results in a much more uniform flow pattern on the pressure surface, and the "striping" effect observed on the airfoil suction surface is not nearly so evident on the pressure surface. The spanwise migration of the coolant jets is clearly displayed, and the mixing of neighboring jets can also be observed. The original design intent of the C3X showerhead film cooling scheme was to place the center row of holes at the airfoil stagnation point. Based on the calculations, it appears that the center row of holes is slightly aft on the pressure surface of the actual stagnation point, and as a result, the bulk of the coolant flow emerging from the center row of holes ends up on the airfoil pressure surface. There is some slight variation with spanwise position for the exact stagnation point due to the coolant hole pattern, and there is some evidence of small leakage flows about the leading edge from coolant flow jets near the stagnation point.

It was observed that the secondary flow within the jet hinders the effectiveness of the cooling scheme as outlined in Figure 6.8. This figure illustrates the detrimental effects caused by the secondary flow within the jet, and the resulting interaction with the outer hot gas flow. As the coolant jet follows the airfoil surface, the secondary flow within the jet acts to entrain hot fluid from the outer region and draw it down towards the airfoil surface between the adjacent jets. Eventually, enough hot gas migrates to the airfoil surface that the jet essentially "lifts off" the airfoil surface and is no longer effective as a cooling medium. This phenomena is captured numerically and is illustrated in the predicted total temperature contours given in Figure 6.9. Predicted total temperature contours are given on two grid surfaces which are essentially normal to the airfoil surface at different chordwise locations. The coolant jets are clearly defined by the array of low total temperature regions near the airfoil surface on the forward contour plane. The coolant jet "lift-off" phenomena described above is plainly visible on the downstream contour plane. The seepage of hot gas due to secondary flow entrainment results in a buffer layer of hot gas between the coolant jet and the airfoil surface which degrades the cooling scheme effectiveness.

A comparison of the predicted and measured airfoil surface static pressure ratio and heat transfer coefficient distributions are presented in Figures 6.10 and 6.11 for the reduced mesh prediction of Run #4415 of the C3X vane cascade. Computational results are presented for several spanwise mesh planes for the computational results to illustrate the "striping" effect described above. The effect of the striping phenomena on the airfoil suction

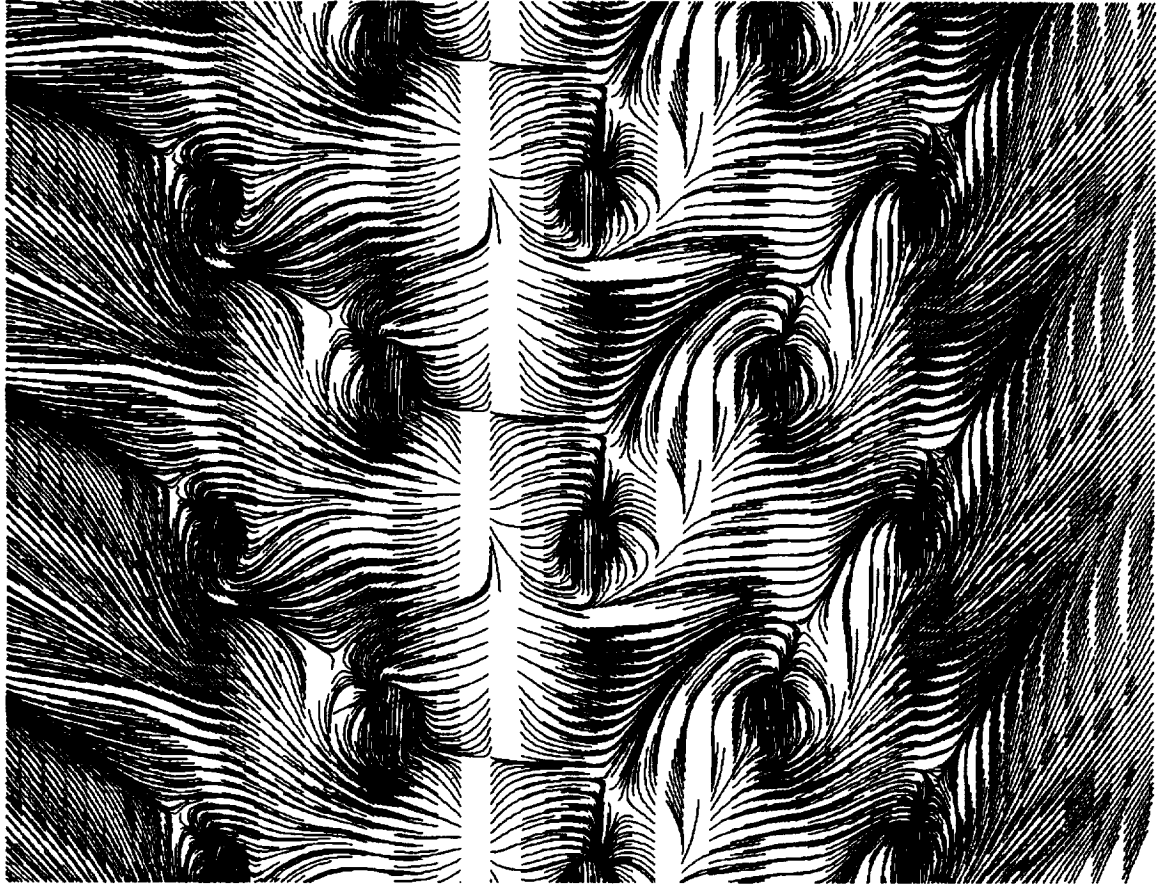


Figure 6.5: Predicted near leading edge airfoil surface shear flow pattern for Run # 4415 of the C3X turbine vane cascade

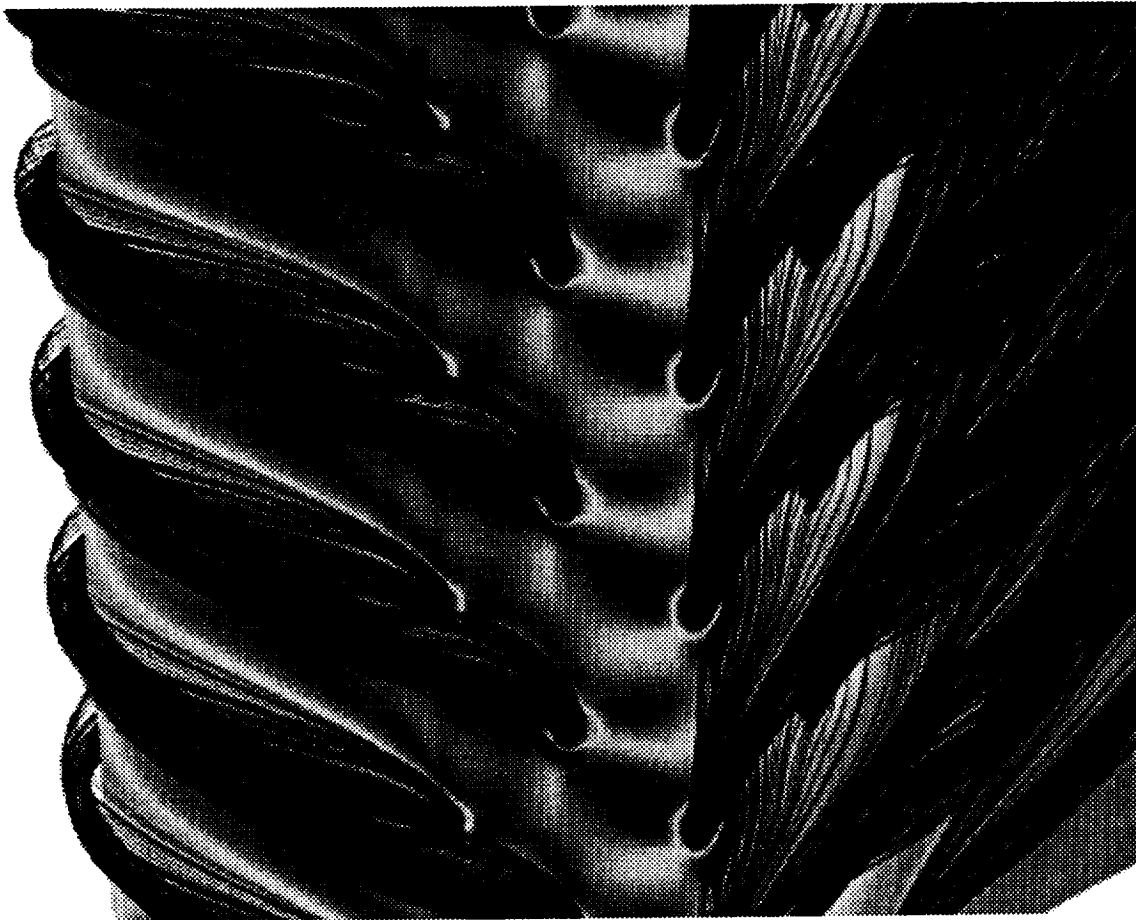


Figure 6.6: Predicted Coolant Flow Particle Traces and Near Airfoil Surface Temperature Contours for Run # 4415 of the C3X turbine vane cascade

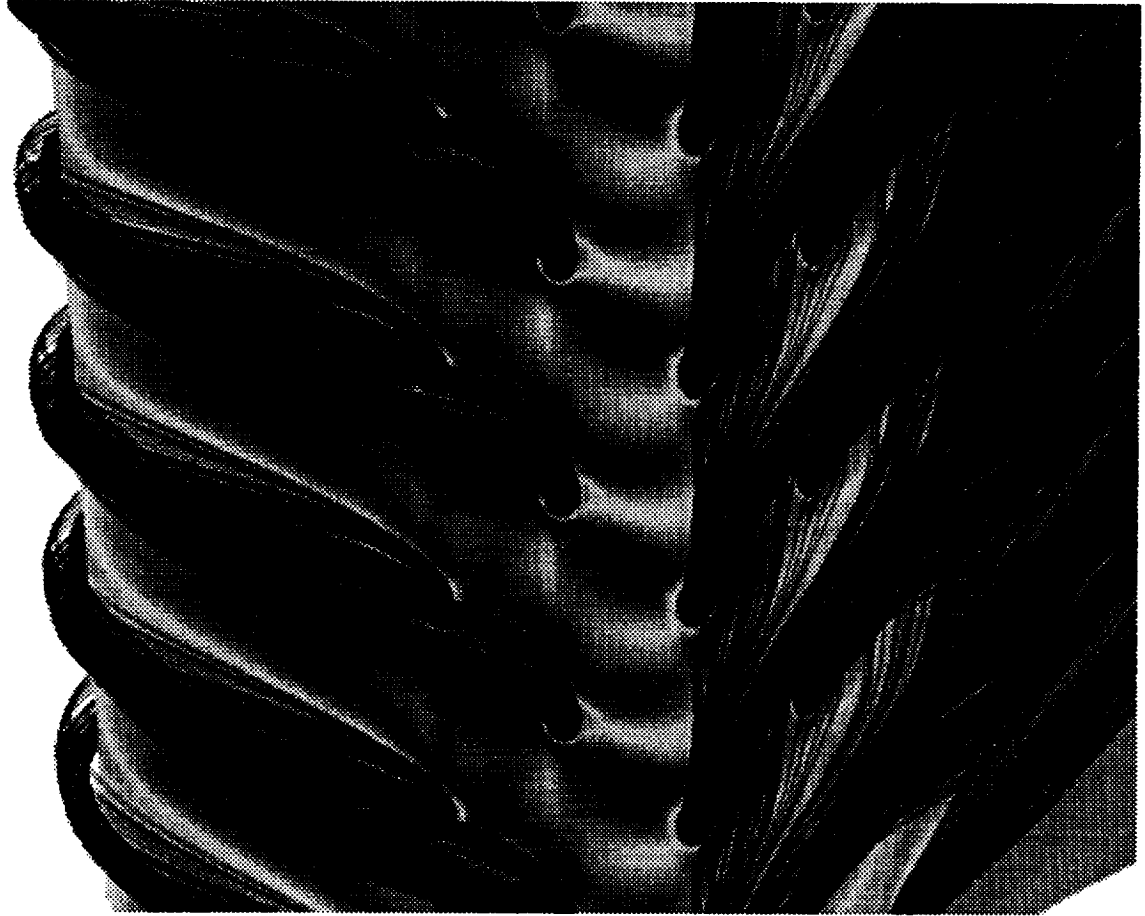


Figure 6.7: Predicted Coolant Flow Particle Traces and Near Airfoil Surface Temperature Contours for Run # 4435 of the C3X turbine vane cascade

Coolant Jet Secondary Flow Hot Gas Entrainment (View Looking Downstream)

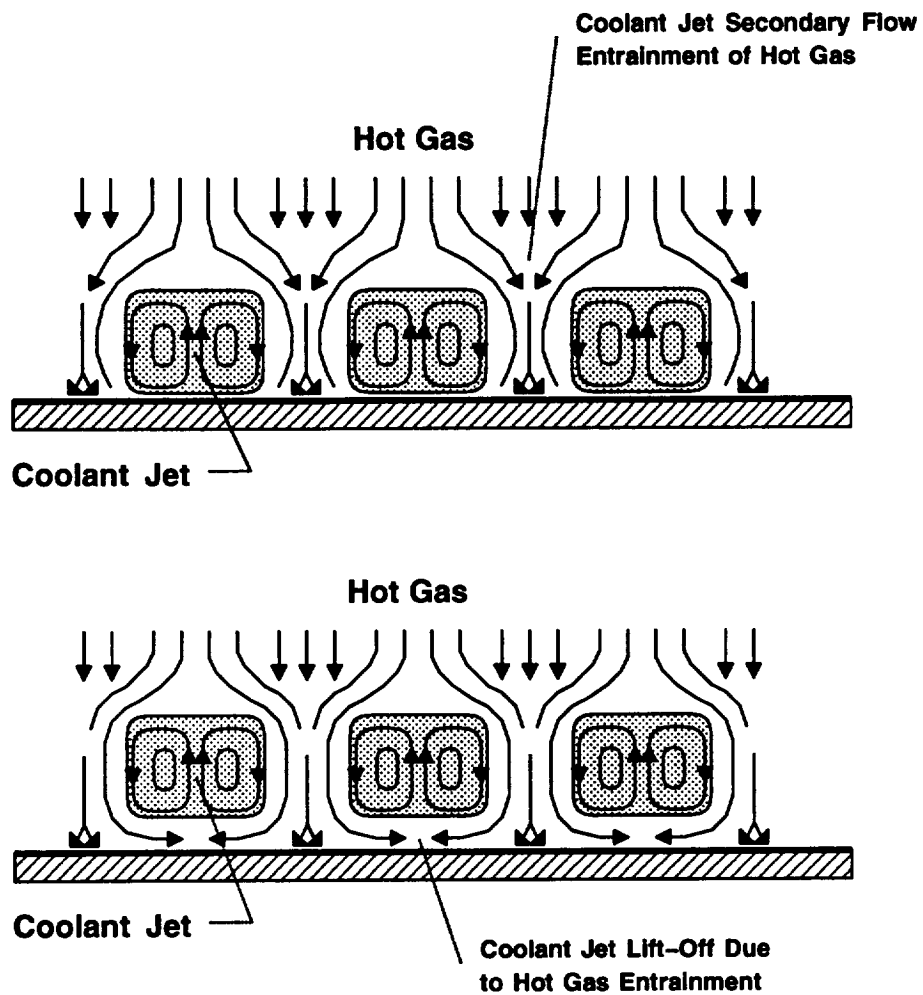


Figure 6.8: Cooling Flow Effectiveness Degradation and Coolant Jet Lift-Off Due to Coolant Jet Secondary Flow and Hot Gas Entrainment

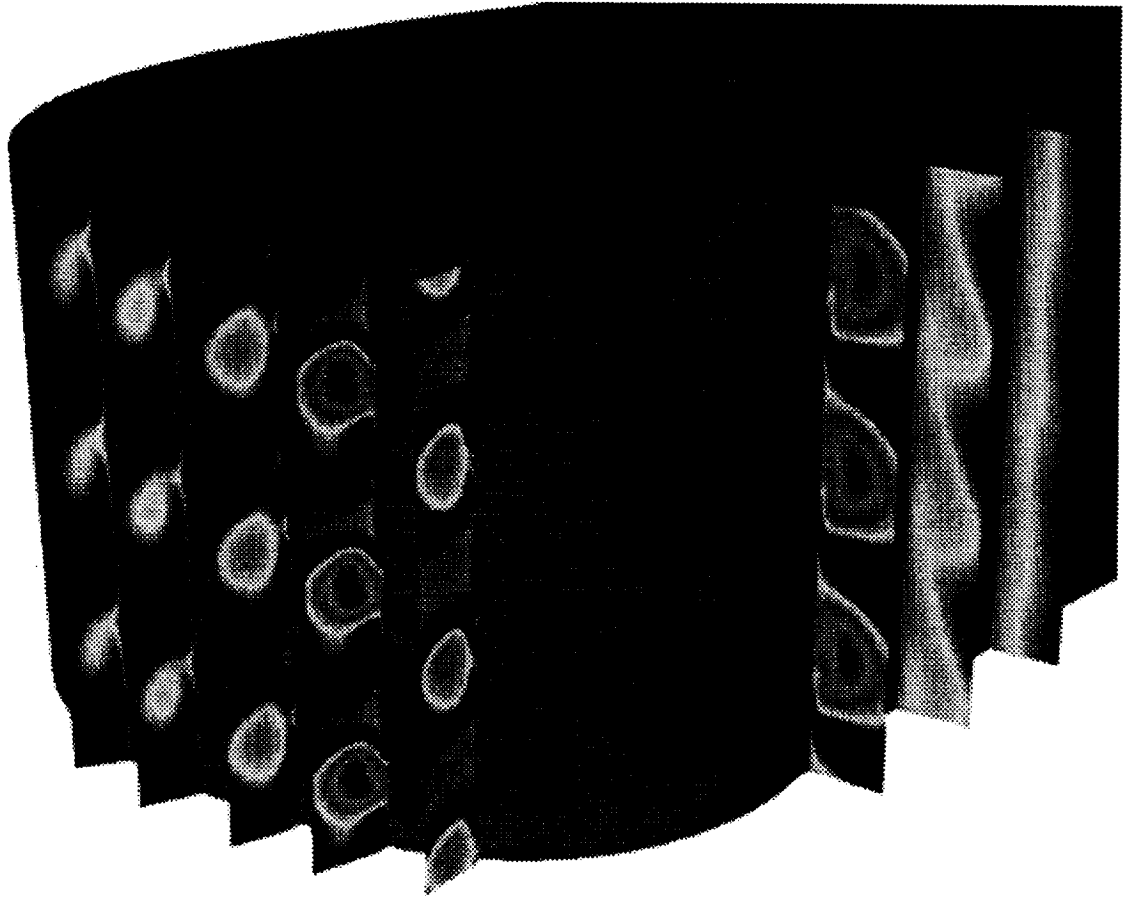


Figure 6.9: Predicted Chordwise Near Airfoil Surface Total Temperature Contours for Run # 4415 of the C3X Turbine Vane Cascade Illustrating Coolant Jet Lift-Off

surface is clearly pronounced by the large variation in predicted heat transfer coefficient distributions on the suction surface, as compared to the rather miniscule variations along the airfoil pressure surface. It would appear that the experimental data does, in fact, represent a spanwise average of the predicted results for this case, although no detailed conclusions may be drawn from these comparisons due to the limitations in the C3X rig instrumentation described earlier. Similar comparisons of static pressure ratio and heat transfer coefficient distributions are presented for the fine mesh results for Run #4415 on Figures 6.12 and 6.13. Similar characteristics were observed for both the reduced and fine mesh calculations. The predicted airfoil surface heat transfer coefficient distribution for the corresponding non-cooled flow is also presented in Figure 6.13 for comparison. The effective reduction in airfoil surface heat transfer coefficient is indicated by the lower levels of heat transfer illustrated for the film-cooled predictions given on Figure 6.13.

A comparison of the predicted and measured airfoil surface static pressure ratio and heat transfer coefficient distributions are presented for the reduced mesh calculation in Figures 6.14, and 6.15 respectively, for Run #4435 of the C3X vane cascade. Similar characteristics were observed for this set of calculations as compared to the Run #4415 calculations, although the reduction in airfoil surface heat transfer coefficient distributions is now lower due to the increase in coolant gas total temperature ratio from 0.7 to 0.9.

The following section discusses results from the film-cooled C3X calculations for the higher coolant total pressure ratio corresponding to Runs #4417 and #4437 described on Figure 5.3. For these two calculations the coolant total pressure ratio was approximately 1.5 which results in a relatively high coolant flow (compared to the low coolant total pressure ratio calculations described later). The predicted near-leading edge airfoil surface streamline flow pattern for Run # 4417 is illustrated in Figure 6.16. The coolant holes have been outlined for reference, with the pressure side of the airfoil on the right, and the suction side of the airfoil on the left. In this case, the flow pattern is just as striking, but significantly altered from the flow pattern described for Run #4415 given in Figure 6.5. In this case, the shear forces resulting from the interaction between the coolant flow and the primary flow again generate the secondary flow within the jet, but the jet has significantly more momentum than the previous calculations described, and the jet trajectory indicates a significant component of spanwise momentum.

A graphical depiction of the coolant flow jets is presented in Figures 6.17

C3X Airfoil Cascade NASA CR174827 Run 4415 (Cooled, Mexit=0.90, Re2=1.99E6)
ADPAC 2-D Aerodynamic Analysis
Airfoil Surface Static Pressure Ratio Distribution

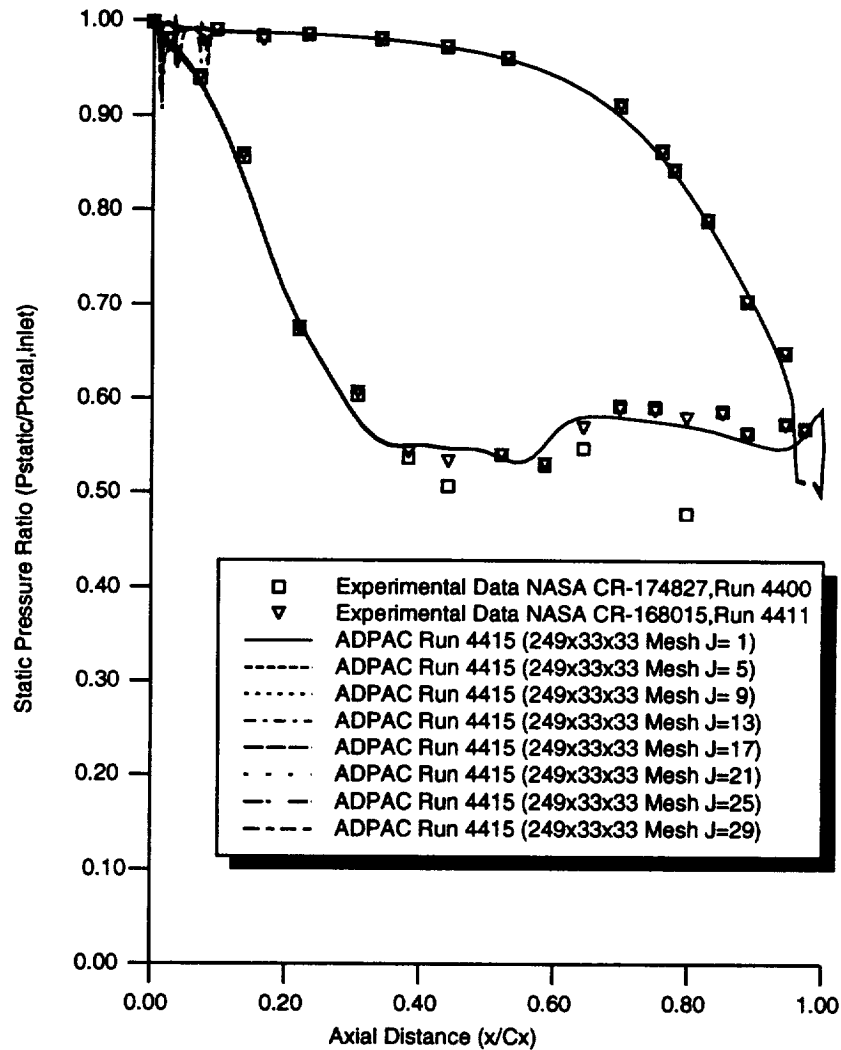


Figure 6.10: Comparison of Predicted and Experimental Airfoil Surface Static Pressure Ratio Distributions for Run # 4415 of the C3X Turbine Vane Cascade on the Reduced Mesh (249x33x33 Airfoil Mesh)

C3X Airfoil Cascade NASA CR-174827 Run 4415 (Cooled, $M_{exit}=0.90, Re_2=1.99E6$)
ADPAC 2-D Aerodynamic Analysis
Airfoil Heat Transfer Coefficient Distribution ($h_o=200\text{BTU/hr/sqft/F}$)

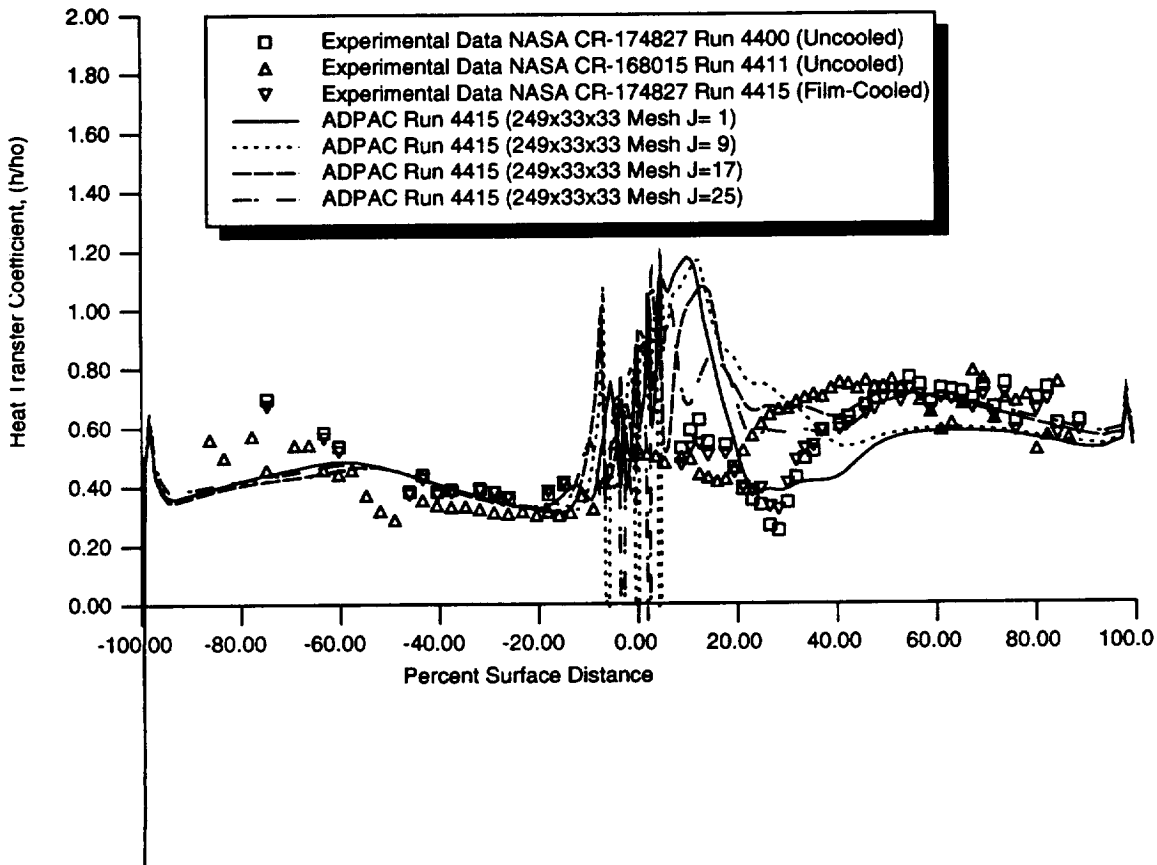


Figure 6.11: Comparison of Predicted and Experimental Airfoil Surface Heat Transfer Coefficient Distributions for Run # 4415 of the C3X Turbine Vane Cascade on the Reduced Mesh (249x33x33 Airfoil Mesh)

C3X Airfoil Cascade NASA CR174827 Run 4415 (Cooled, $Mach=0.90, Re_2=1.99E6$)
ADPAC 3-D Aerodynamic Analysis
Airfoil Surface Static Pressure Ratio Distribution

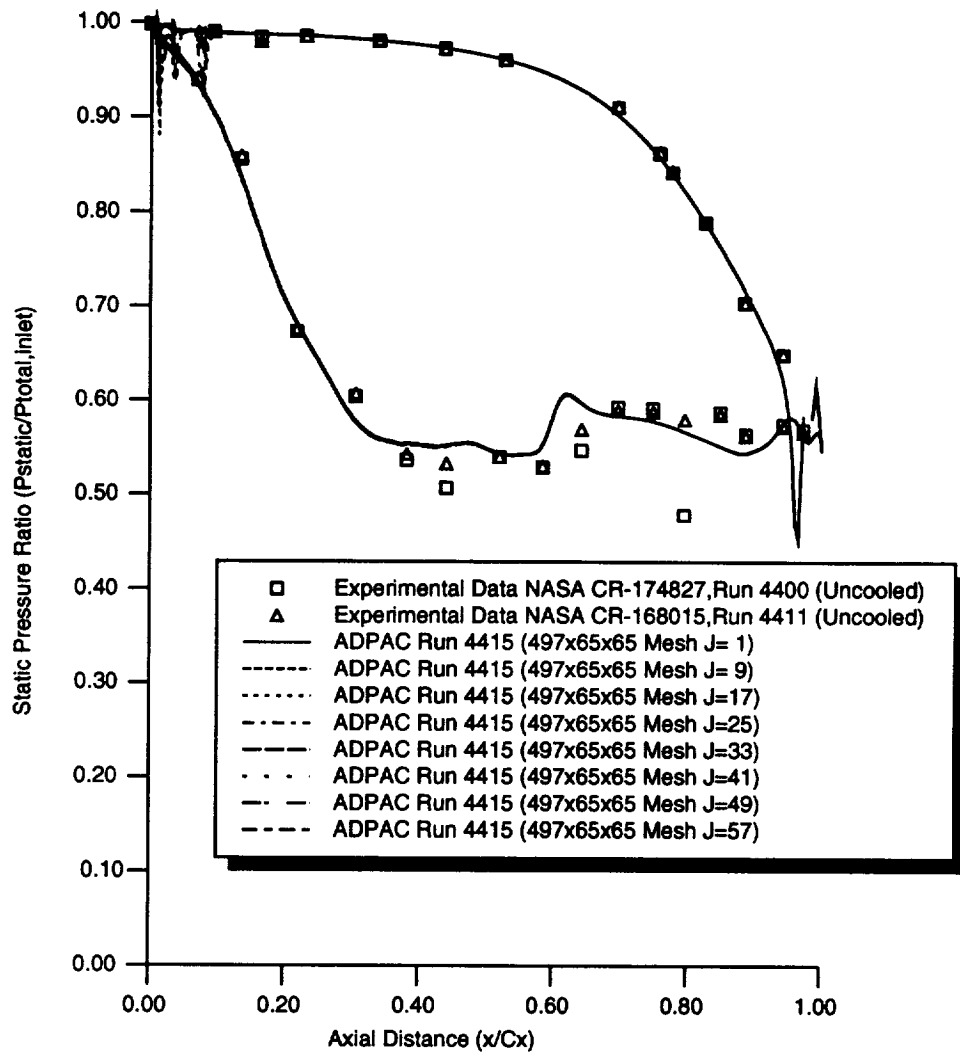


Figure 6.12: Comparison of Predicted and Experimental Airfoil Surface Static Pressure Ratio Distributions for Run # 4415 of the C3X Turbine Vane Cascade on the Fine Mesh (497x65x65 Airfoil Mesh)

C3X Airfoil Cascade NASA CR-174827 Run 4415 (Cooled, $Mach=0.90$, $Re_2=1.99E6$)
ADPAC 3-D Aerodynamic Analysis
Airfoil Heat Transfer Coefficient Distribution ($h_o=200\text{BTU/hr/sqft/F}$)

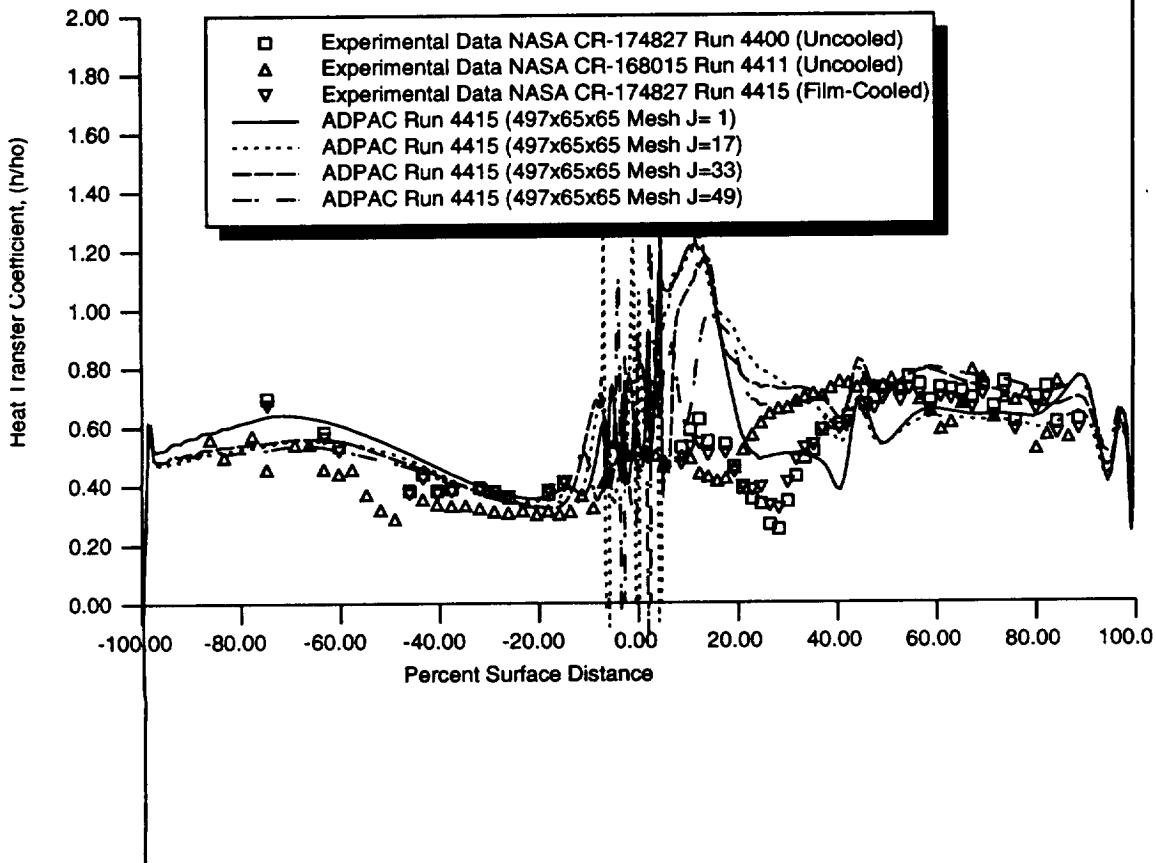


Figure 6.13: Comparison of Predicted and Experimental Airfoil Surface Heat Transfer Coefficient Distributions for Run # 4415 of the C3X Turbine Vane Cascade on the Fine Mesh (497x65x65 Airfoil Mesh)

C3X Airfoil Cascade NASA CR174827 Run 4435 (Cooled, Mexit=0.90, Re2=1.99E6)
ADPAC 2-D Aerodynamic Analysis
Airfoil Surface Static Pressure Ratio Distribution

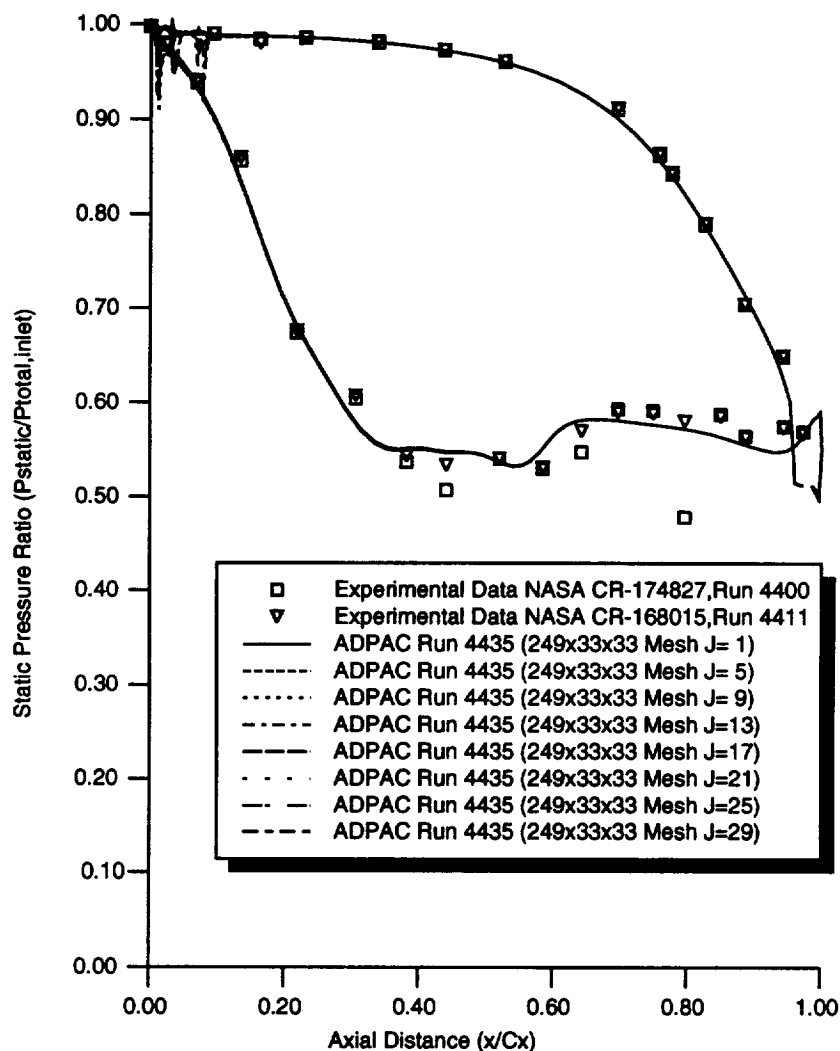


Figure 6.14: Comparison of Predicted and Experimental Airfoil Surface Static Pressure Ratio Distributions for Run # 4435 of the C3X Turbine Vane Cascade on the Reduced Mesh (249x33x33 Airfoil Mesh)

C3X Airfoil Cascade NASA CR-174827 Run 4435 (Cooled, Mexit=0.90, Re2=1.99E6)
ADPAC 2-D Aerodynamic Analysis
Airfoil Heat Transfer Coefficient Distribution (ho=200BTU/hr/sqft/F)

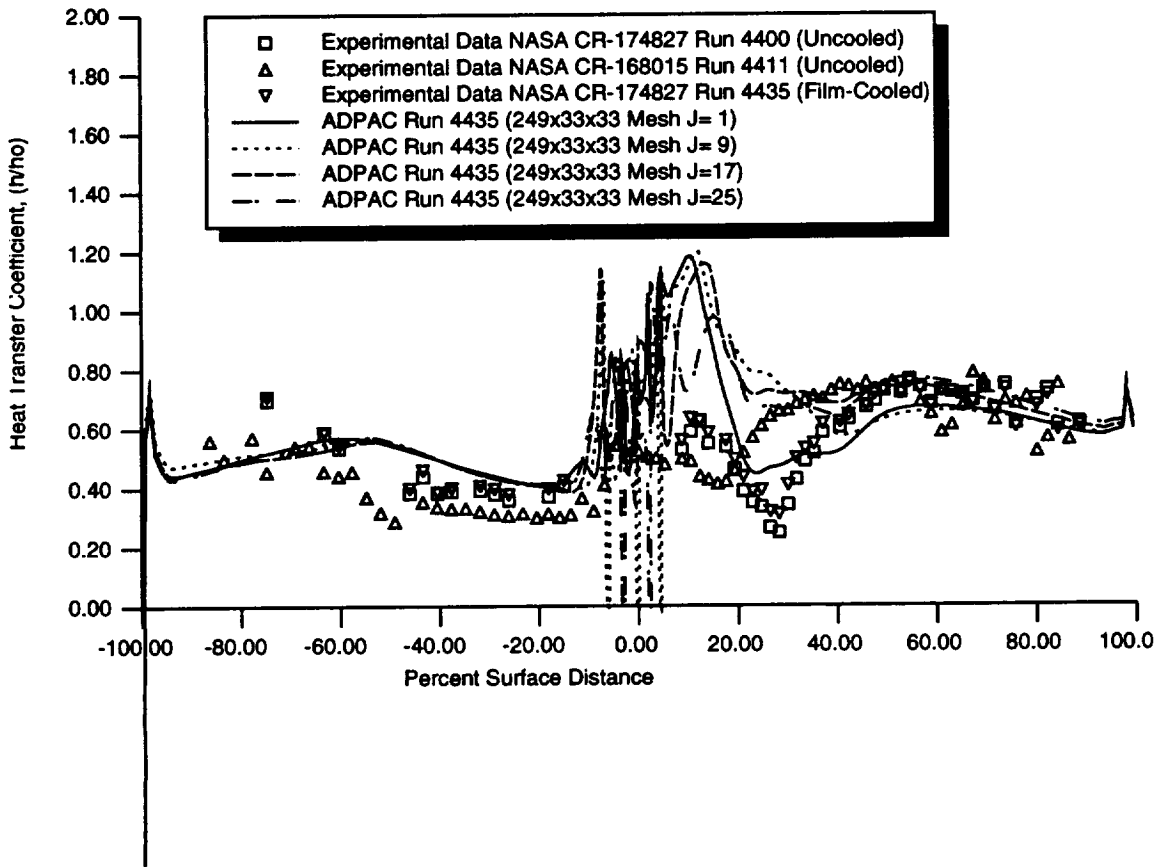


Figure 6.15: Comparison of Predicted and Experimental Airfoil Surface Heat Transfer Coefficient Distributions for Run # 4435 of the C3X Turbine Vane Cascade on the Reduced Mesh (249x33x33 Airfoil Mesh)

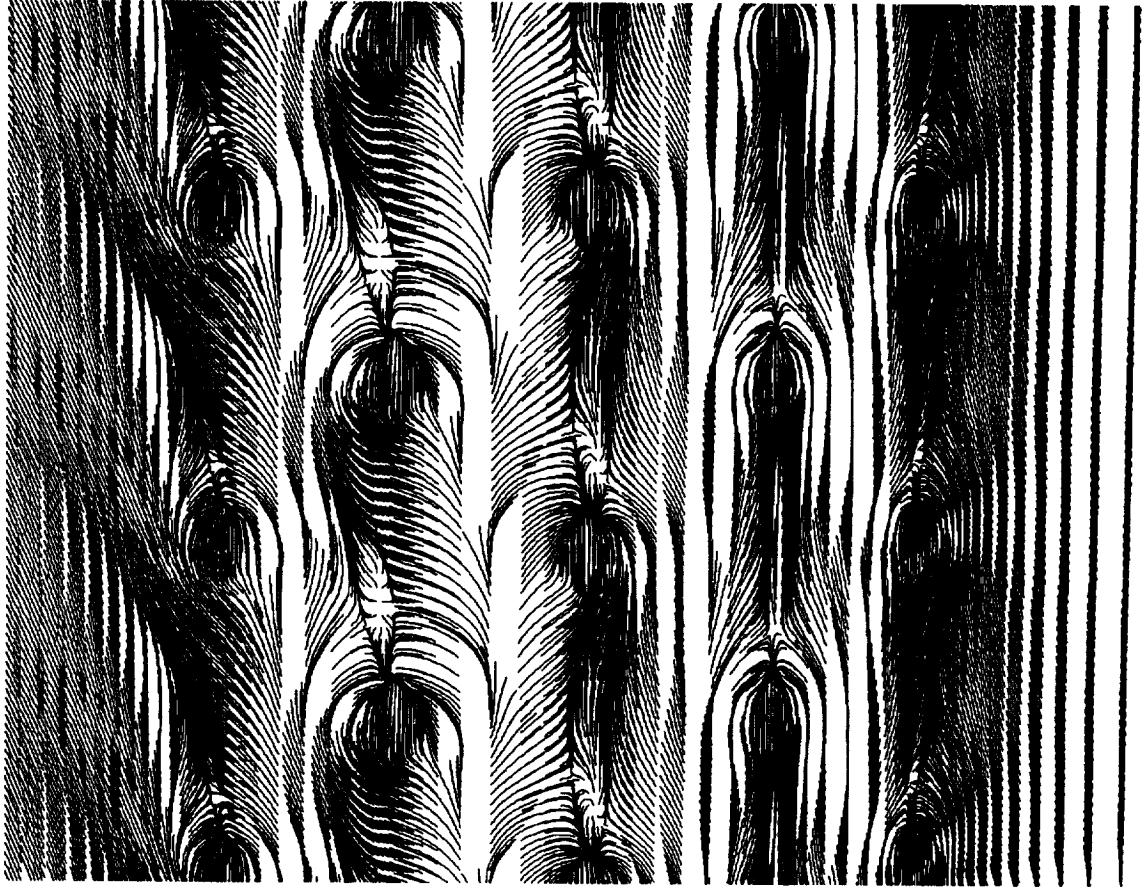


Figure 6.16: Predicted near leading edge airfoil surface shear flow pattern for Run # 4417 of the C3X turbine vane cascade

and 6.18. These figures illustrate the coolant flow particle traces and predicted near airfoil surface temperature contours (indicative of heat transfer coefficient) for Run # 4417 and #4437, respectively. The coolant flow particle traces are very similar for these two calculations, with differences in cooling level due to the higher coolant total temperature ratio for Run #4437. In these cases, as the coolant flow jet emerges from the injection site, the relative ratios of coolant jet and primary gas flow momentum permit the jets to follow a more spanwise trajectory on both the airfoil suction and pressure surfaces. As a result, the “striping” pattern previously observed for the low coolant total pressure ratio calculations is eliminated, and a more even distribution of coolant flow is achieved. Naturally, this improved effectiveness was achieved at the cost of additional coolant flow and an increase in coolant total pressure required to drive the flow, both undesirable options for the turbine engine designer.

A comparison of the predicted and measured airfoil surface static pressure ratio and heat transfer coefficient distributions are presented for the reduced mesh in Figures 6.19 and 6.20 for Run #4417 of the C3X vane cascade. Predicted and measured airfoil surface heat transfer coefficient distributions for the fine mesh calculation are presented in Figure 6.21. For completeness, a comparison of the predicted and measured airfoil surface static pressure ratio and heat transfer coefficient distributions are also presented for the reduced mesh calculation in Figures 6.22 and 6.23 respectively, for Run #4437 of the C3X vane cascade. It is now evident from these results that the spanwise variation in airfoil surface heat transfer coefficient distributions has been reduced by the improvement in jet spanwise migration, and the reduced effects of jet merging.

6.8 C3X Vane Cascade Porous Surface Boundary Condition Heat Transfer Predictions

In this section, the porous surface boundary condition described in Section 3.6.1 was applied in the *ADPAC* analysis for the prediction of the C3X turbine vane cascade film-cooling flow problem. Due to the spanwise symmetry implied by the averaging procedure in the porous surface boundary model, the calculations were performed on a 2-D grid taken from the first spanwise slice

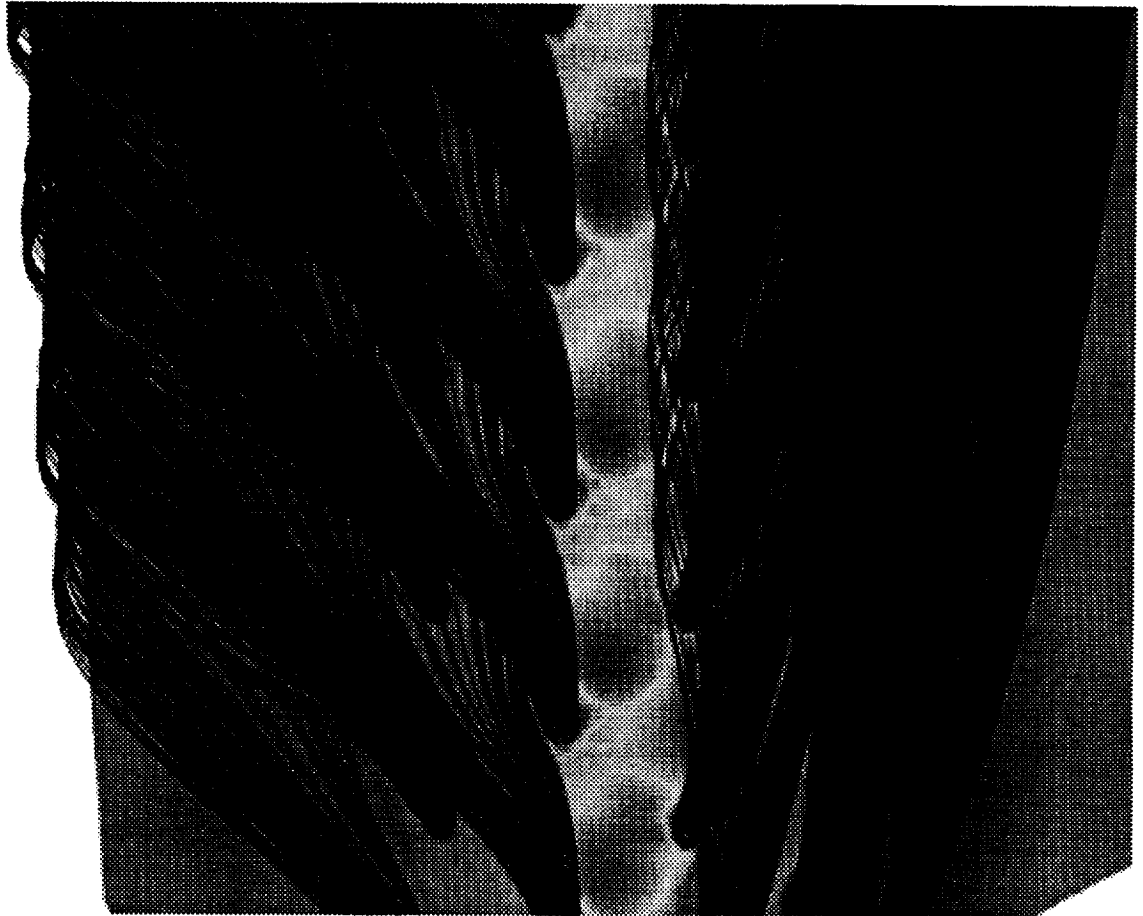


Figure 6.17: Predicted Coolant Flow Particle Traces and Near Airfoil Surface Temperature Contours for Run # 4417 of the C3X turbine vane cascade



Figure 6.18: Predicted Coolant Flow Particle Traces and Near Airfoil Surface Temperature Contours for Run # 4437 of the C3X turbine vane cascade

C3X Airfoil Cascade NASA CR174827 Run 4417 (Cooled, Mexit=0.90, Re2=1.99E6)
ADPAC 2-D Aerodynamic Analysis
Airfoil Surface Static Pressure Ratio Distribution

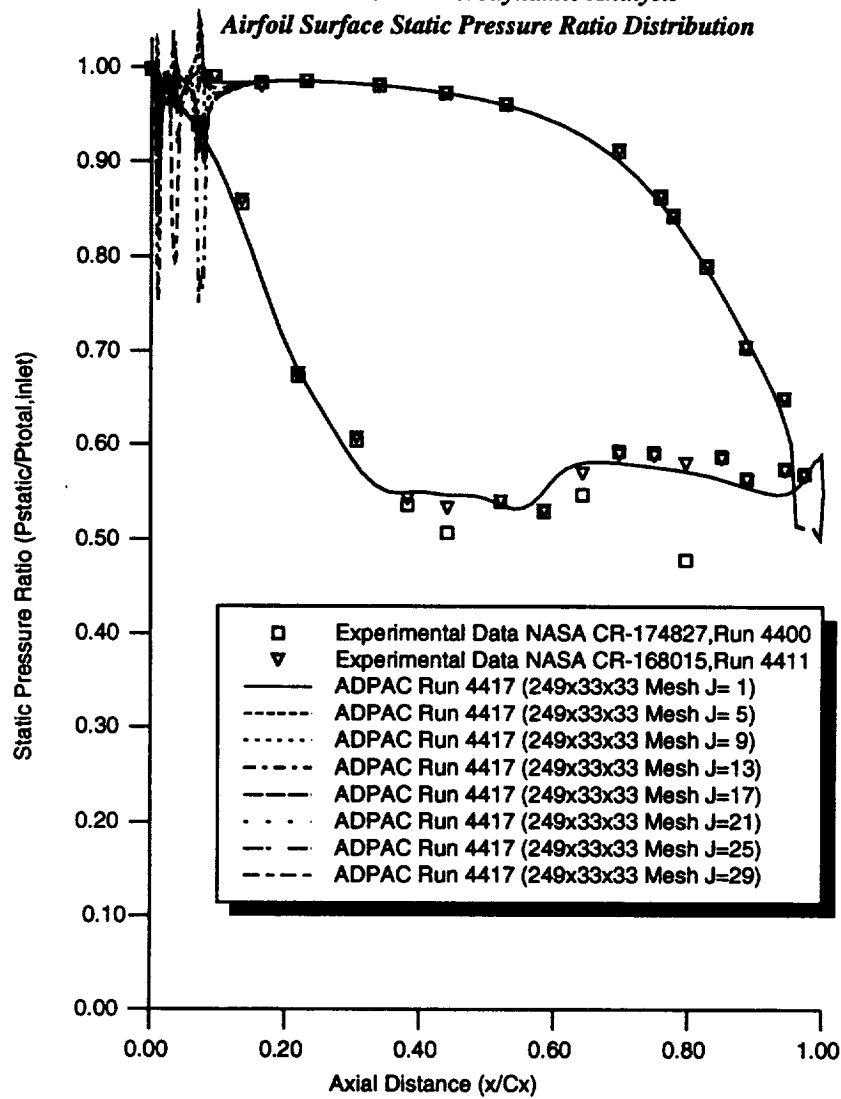


Figure 6.19: Comparison of Predicted and Experimental Airfoil Surface Static Pressure Ratio Distributions for Run # 4417 of the C3X Turbine Vane Cascade on the Reduced Mesh (249x33x33 Airfoil Mesh)

C3X Airfoil Cascade NASA CR-174827 Run 4417 (Cooled, $Mach=0.90, Re_2=1.99E6$)
ADPAC 2-D Aerodynamic Analysis
Airfoil Heat Transfer Coefficient Distribution ($h_o=200\text{BTU/hr/sqft/F}$)

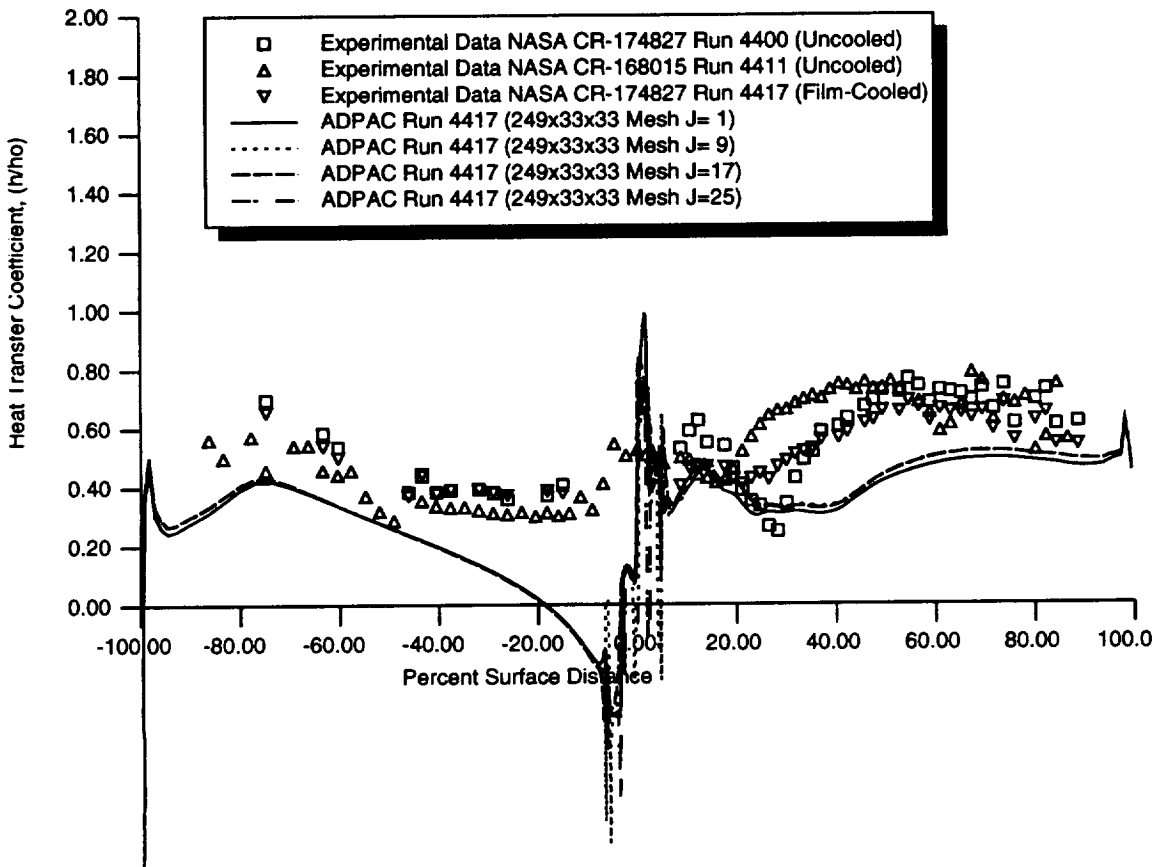


Figure 6.20: Comparison of Predicted and Experimental Airfoil Surface Heat Transfer Coefficient Distributions for Run # 4417 of the C3X Turbine Vane Cascade on the Reduced Mesh (249x33x33 Airfoil Mesh)

C3X Airfoil Cascade NASA CR-174827 Run 4417 (Cooled, $Mach=0.90, Re_2=1.99E6$)
ADPAC 2-D Aerodynamic Analysis
Airfoil Heat Transfer Coefficient Distribution ($h_o=200\text{BTU/hr/sqft/F}$)

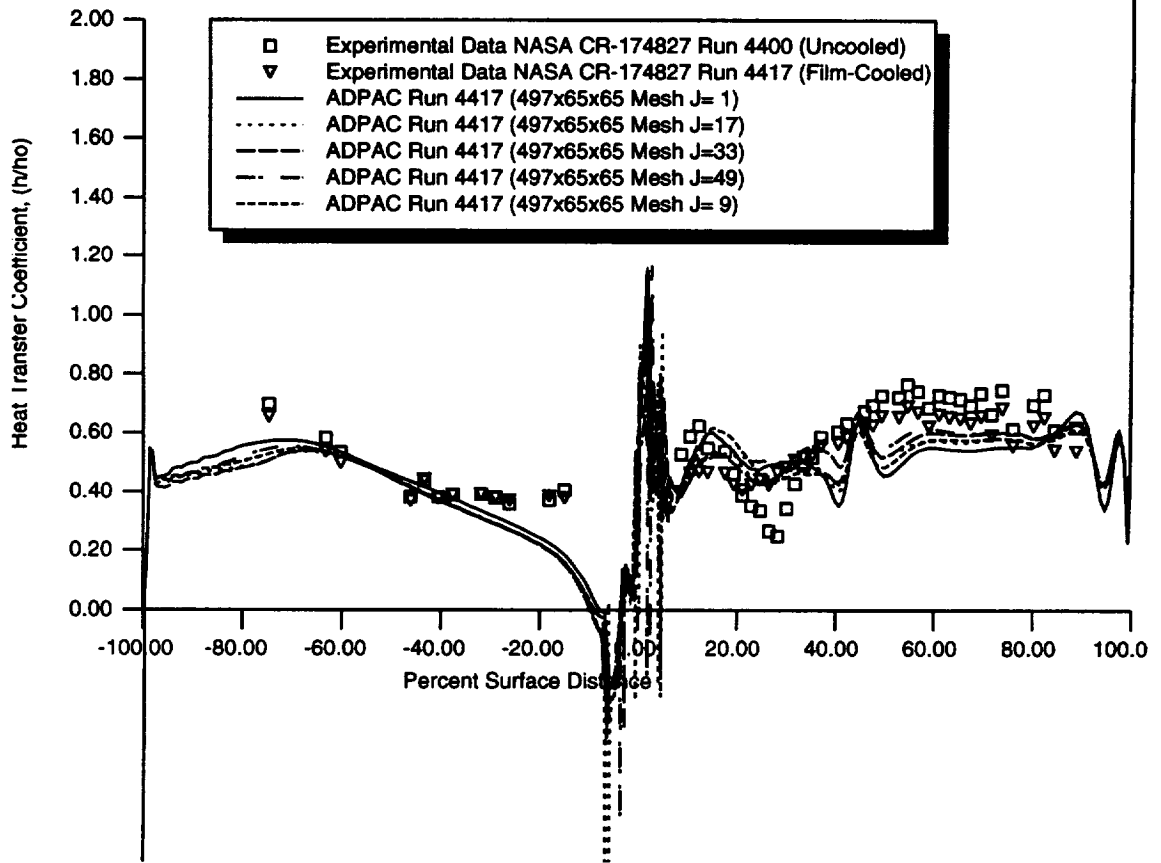


Figure 6.21: Comparison of Predicted and Experimental Airfoil Surface Heat Transfer Coefficient Distributions for Run # 4417 of the C3X Turbine Vane Cascade on the Fine Mesh (497x65x65 Airfoil Mesh)

C3X Airfoil Cascade NASA CR174827 Run 4437 (Cooled, Mexit=0.90, Re2=1.99E6)
ADPAC 2-D Aerodynamic Analysis
Airfoil Surface Static Pressure Ratio Distribution

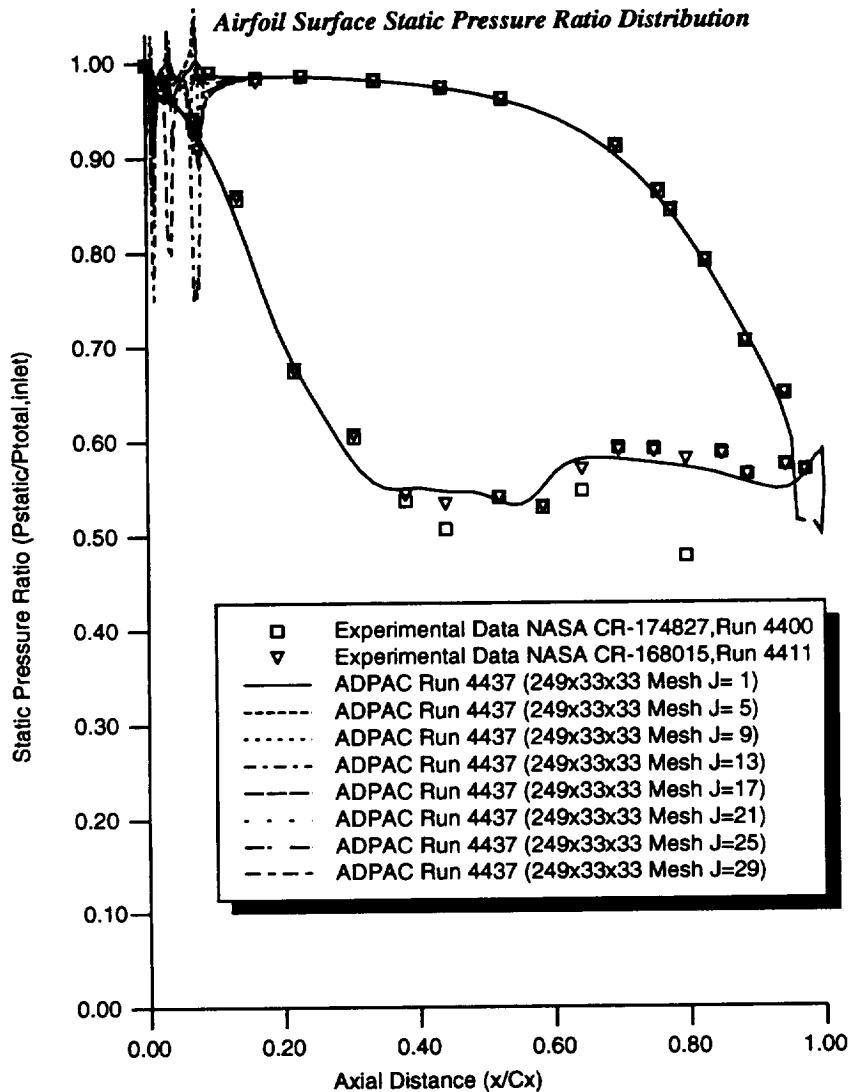


Figure 6.22: Comparison of Predicted and Experimental Airfoil Surface Static Pressure Ratio Distributions for Run # 4437 of the C3X Turbine Vane Cascade on the Reduced Mesh (249x33x33 Airfoil Mesh)

C3X Airfoil Cascade NASA CR-174827 Run 4437 (Cooled, Mexit=0.90, Re2=1.99E6)
ADPAC 2-D Aerodynamic Analysis
Airfoil Heat Transfer Coefficient Distribution ($h_o=200\text{BTU/hr/sqft/F}$)

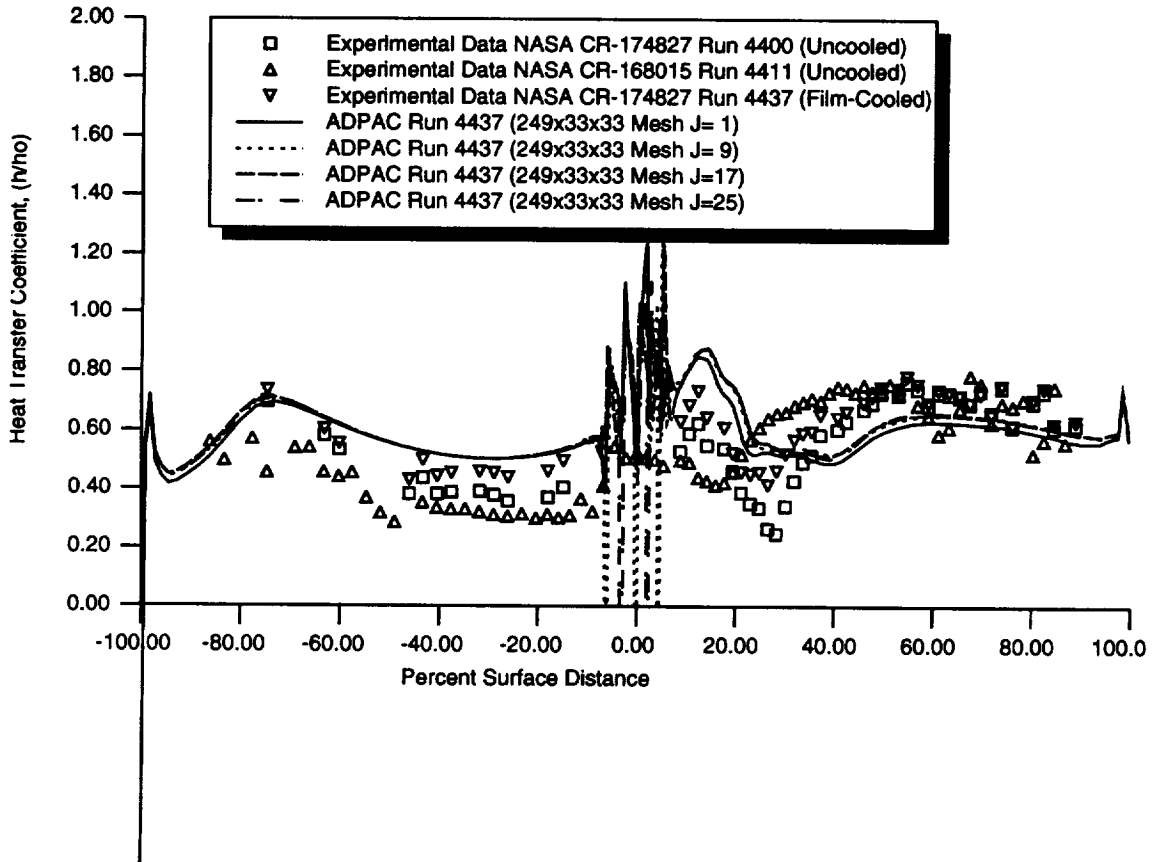


Figure 6.23: Comparison of Predicted and Experimental Airfoil Surface Heat Transfer Coefficient Distributions for Run # 4437 of the C3X Turbine Vane Cascade on the Reduced Mesh (249x33x33 Airfoil Mesh)

of the finest 3-D mesh used in the discrete site film-cooling flow calculations described in the previous section. The Mach number and Reynolds number selected for this study were 0.9 and 2,000,000, respectively. The coolant to gas total temperature and total pressure ratios were determined from the available experimental data for Run #4415 and are listed in Figure 5.3.

The porous surface boundary condition was utilized over a region roughly covering the leading edge showerhead film cooling pattern, and overlapping the streamwise extent of the injection holes by approximately 1 hole diameter along both the suction and pressure surfaces of the airfoil. The injection total pressure and temperature were set according to the data in Table 5.3. The initial area ratio (see Section 3.6.1) used for the porous wall boundary condition was set to 3%, based on an integration of the geometric injection and noninjection surface areas for the 3-D mesh. Preliminary calculations using the true geometric area ratio resulted in a coolant mass flow rate significantly lower than the experimental measurements. This was due, in part, to the averaging procedure used in the porous boundary condition model. The specified area ratio used in the boundary condition model was arbitrarily increased until the predicted mass flow rate matched the experimental level. The final area ratio used in the boundary condition model was 0.15. The analysis utilized 3 levels of multigrid, and the solution convergence behavior was found to be similar to previous 3-D film-cooled airfoil calculations.

Illustrations of the predicted Mach number contours and near leading edge velocity vectors are given in Figure 6.24. The thermal layering effect afforded by the coolant injection is clearly visible in this figure. The injection velocities resulting from this boundary model were fairly uniform across the porous model region in spite of the fact that the model permits mesh cell to mesh cell variations in the injected flow (although the injection velocity is assumed to be uniform across any given mesh cell). The integrated injection mass flow for this case was 0.01323 pounds per second (for the complete test airfoil based on the 0.15 area ratio prediction) and compares favorably to both the predicted three-dimensional discrete site injection mass flow rate of 0.01374 pounds per second and the experimentally measured injection mass flow rate of 0.0133 pounds per second.

A comparison of experimental and predicted airfoil surface heat transfer coefficient distributions are presented in Figure 6.25 for both the porous surface boundary model calculation and selected constant span airfoil surface heat transfer coefficient distributions for the 3-D discrete site film-cooled flow

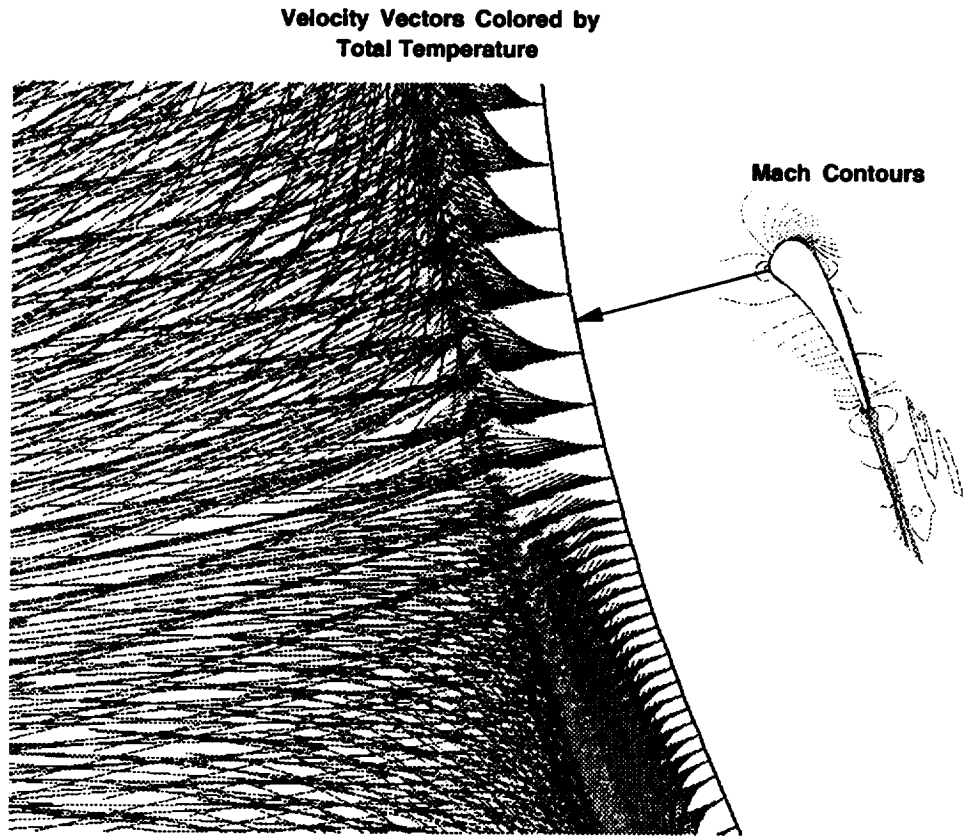


Figure 6.24: Predicted Mach Contours and Near Leading Edge Velocity Vectors for Porous Boundary Condition Analysis of Run # 4415 of the C3X Turbine Vane Cascade

calculation. It is interesting to note that the porous boundary model prediction more closely resembles the experimental data in the laminar/transition region on the airfoil suction surface. This is primarily due to the early transition which occurs in the 3-D model due to the complex coolant flow/primary flow interactions which occur near the injection holes, triggering a false transition in the 3-D model. Unfortunately, farther downstream, the porous boundary condition model is less well behaved, and appears to be extremely sensitive to variations in the external flow, as evidenced by the large fluctuations in heat transfer near the sonic point on the airfoil suction surface. This behavior may be indicative of the lack of mixing which is likely to occur

C3X Airfoil Cascade NASA CR-174827 Run 4415 (Cooled, Mexit=0.90, Re2=1.99E6)
ADPAC 3-D Aerodynamic Analysis
Airfoil Heat Transfer Coefficient Distribution ($h_o=200\text{BTU/hr/sqft/F}$)

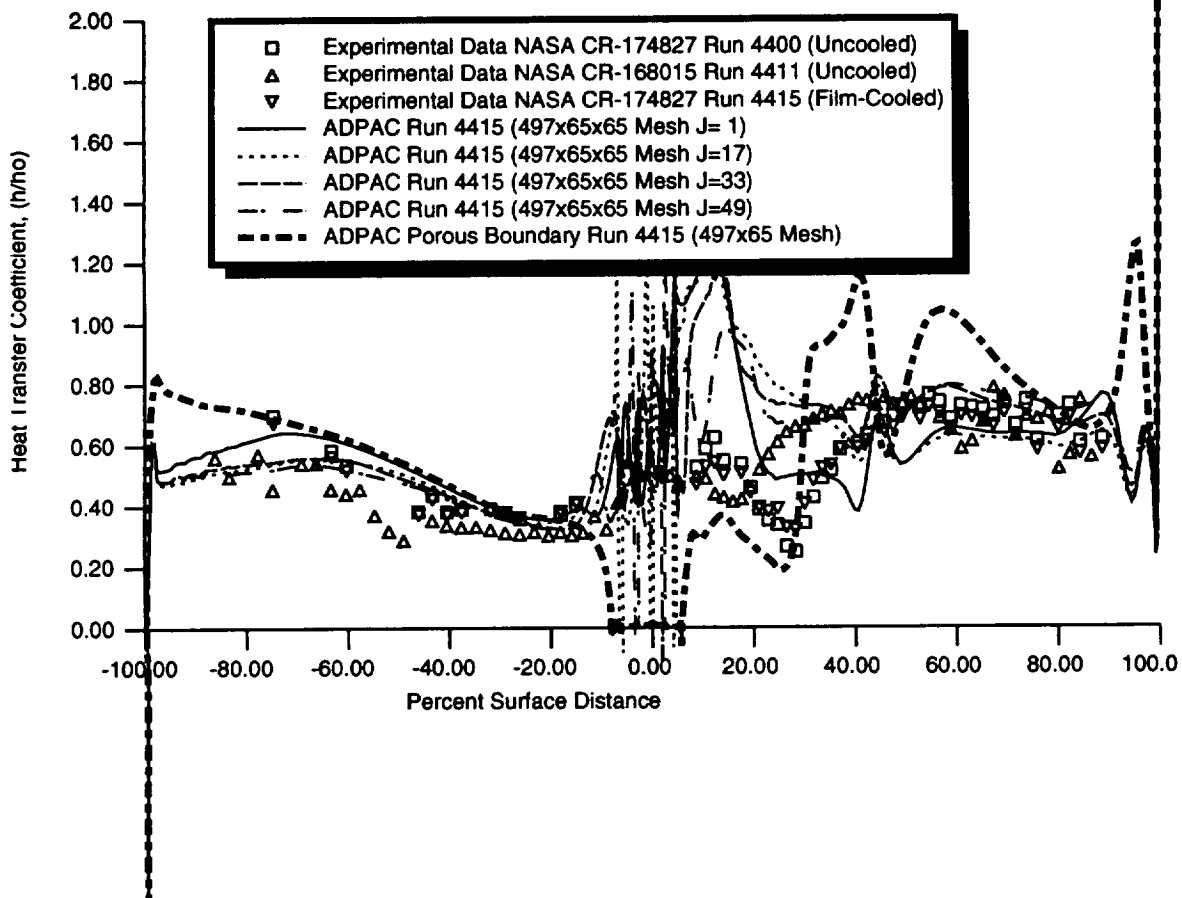


Figure 6.25: Comparison of Predicted and Experimental Airfoil Surface Heat Transfer Coefficient Distributions for Run # 4415 of the C3X Turbine Vane Cascade Illustrating the Porous Surface Boundary Condition Model

for the porous boundary model compared to the 3-D discrete site injection model because the complex secondary flows observed in the 3-D calculations cannot be represented in the porous boundary model.

From these limited results, it is clear that further testing of the porous boundary condition model is needed, and that applications involving finer scale injection sites (the leading edge showerhead cooling scheme for the C3X airfoil has relatively few, large holes when compared to the assumed intent of the porous boundary model) would be more appropriate for this type of analytical approach.

Chapter 7

CONCLUSIONS

Detailed flow and heat transfer predictions have been performed using a Navier-Stokes analysis for realistic turbine airfoil blade rows both with and without leading edge showerhead film cooling. The emphasis of this analysis was to determine grid requirements to accurately predict details of the turbine airfoil heat transfer problem using relatively standard turbulence modeling techniques. These grid requirements were then utilized to define a gridding scheme for the C3X turbine airfoil with leading edge showerhead film cooling. The predicted results were analyzed to extract relevant features of the cooling flow/primary gas flow interaction, and the resultant effect on heat transfer properties in the vicinity of the cooling holes.

Several comments are in order concerning the various numerical techniques applied in this study. It was immediately apparent that the algebraic turbulence model is not ideally suited for the general heat transfer problems which can occur for modern turbomachinery blade designs. Future efforts may benefit from more detailed turbulence models developed for complex 3-D flows, such as two-equation turbulence models. Of equal importance is the development of accurate transition point, transition path, and transition length models to accurately account for the unusual transition phenomena known to occur for turbine airfoils, particularly the flow on the pressure side of the airfoil.

Data analysis of the predictions from the mesh dependence study for the Mark II airfoil cascade clearly indicated the difficulties associated with achieving mesh independence for flows with shock waves. It is relatively easy to demonstrate the requirements for mesh independence of the distribution

of mesh points normal to the airfoil surface ($y^+ \leq 3$). Unfortunately, changes in spatial resolution along the airfoil surface did not achieve the same level of mesh independence as changes in the mesh spacing normal to the mesh surface because of the problems associated with resolving the normal shock which occurs for the Mark II airfoil flow. In spite of this limitation, excellent agreement was achieved between predictions and experiment for airfoil surface static pressure distributions, and reasonable agreement was achieved for airfoil surface heat transfer coefficients. The best agreement between experiment and analysis was achieved by allowing transition on the suction surface of the airfoil, but maintaining fully turbulent flow on the pressure surface. Interpretation of the various experimental and numerical data suggests that the pressure surface actually experiences a long gradual transition rather than the relatively sharp transition which occurs on the suction surface of the airfoil. Clearly this behavior cannot be reproduced with the point transition scheme utilized in the present analysis. Additional calculations for the Mark II airfoil cascade indicated that although the analysis did not always accurately predict the *level* of heat transfer, the apparent effects of changes in Mach number and Reynolds number on the airfoil surface heat transfer coefficient distributions were accurately reproduced.

Calculations for the non-cooled C3X airfoil demonstrated essentially the same features as the Mark II airfoil predictions. The mesh dependence study for the C3X airfoil was successful in establishing the usual criteria for mesh independence for heat transfer predictions ($y^+ \leq 3$). Heat transfer predictions were compared with experimental data for a matrix of 2 different Reynolds numbers and two different Mach numbers. Again, although the level of heat transfer was not ideally predicted, the influence of changes in Reynolds number and Mach number appeared to be accurate. The deficiencies of the point transition turbulence model were more apparent in these results since no shock wave was present to cause rapid transition. Comparisons were also performed for predictions from a proven 2-D boundary layer analysis which was essentially tuned through existing heat transfer data sets. This tuned model did a better job of predicting the heat transfer data, but the implementation in a 2-D boundary layer code has clear limitations for advanced, realistic 3-D turbine airfoil geometries.

Detailed meshes were generated for the C3X airfoil employing a leading edge showerhead film cooling geometry. The film cooling injection sites were modeled as discrete elements in the 3-D grid, and included coolant flow feed

tubes roughly representative of the experimental configuration. Numerical predictions were performed for 2 different coolant/gas temperature and pressure ratios for a fixed Mach number and flow Reynolds number. Numerical results from the analysis indicated a number of pertinent features related to film cooling due to the interaction of the coolant flow jet and primary gas flow. Immediately upon discharge from the coolant hole, the coolant flow jet is redirected to a trajectory more parallel with the airfoil surface. The amount of redirection appears to be directly dependent on the ratio of momentum of the coolant jet as opposed to the primary gas flow. The jet itself assumes a crossflow pattern indicative of a pair of counterrotating vortices. The net effect of these two actions is that the secondary flow often draws hot gas towards the airfoil surface, thus defeating the purpose of the film cooling. Local hot spots resulting from this action were consistently observed immediately behind the cooling holes located in the stagnation zone of the airfoil. In addition, the placement of the cooling holes often resulted in the coalescing of neighboring jet streams into a single, less effective coolant jet, suggesting the need for improvement in the coolant hole pattern. The redirection and spreading of the coolant jet defines the amount of film cooling surface coverage available from the coolant flow, and for low coolant total pressure ratios, poor surface coverage was observed on the suction surface of the airfoil.

Finally, predictions were also obtained from a simplified film cooling flow model based on a porous surface representation of the film cooling injection, rather than the more detailed discrete site injection film cooling model. This procedure failed to reproduce the details available from the discrete model, but is considerably easier to apply for realistic geometries.

The 3-D analytical technique shows great promise for investigating details of the coolant flow/airfoil flow interaction, and the nature and effectiveness of various design changes such as hole size, shape, and placement. The major drawback to this approach is the problem of grid generation, and there is a clear need for combined computer-aided design/grid generation software to simplify the mesh generation process.

Bibliography

- [1] Hylton, L. D., Mihelc, M. S., Turner, E. R., Nealy, D. A., and York, R. E., "Analytical and Experimental Evaluation of the Heat Transfer Distribution Over the Surfaces of Turbine Vanes", NASA CR-168015, 1983.
- [2] Turner, E. R., Wilson, M. D., Hylton, L. D., and Kaufman, R. M., "Analytical and Experimental Evaluation of Surface Heat Transfer Distributions with Leading Edge Showerhead Film Cooling", NASA CR-174827, 1985.
- [3] Hylton, L. D., Nirmalan, V., Sultanian, B., and Kaufman, R., "The Effects of Leading Edge and Downstream Film Cooling on Turbine Vane Heat Transfer", NASA CR-182133, October, 1988.
- [4] Goldstein, R. J., In *Advances in Heat Transfer*, pages 321-379, 1971.
- [5] Goldstein, and Eckert, E. R. G., "Effects of Hole Geometry and Density on Three-Dimensional Film Cooling", *International Journal of Heat Transfer*, Volume 107, pages 595-607, 1974.
- [6] Foster, N. W., and Lampard, D., "The Flow and Film Cooling Effectiveness Injection through a Row of Holes", *Journal of Engineering for Power*, Volume 102, pages 584-588, 1980.
- [7] Jubran, B., and Brown, A., "Film Cooling from Two Rows of Holes Inclined in the Streamwise and Spanwise Directions", *Journal of Engineering for Gas Turbine Power*, Volume 107, pages 85-91, 1985.
- [8] Mehandale, A. B., and Han, J. C., "Influence of High Mainstream Turbulence on Leading Edge Film Cooling Heat Transfer: Effect of

- Film Hole Spacing", International Journal of Heat and Mass Transfer, Volume 35, pages 2593-2604, 1992.
- [9] Yang, R. J., Weinberg, B. C., Shamroth, S. J., and McDonald, H., "Turbine Vane External Heat Transfer-Volume II: Numerical Solutions of the Navier-Stokes Equations for Two- and Three-Dimensional Turbine Cascades with Heat Transfer", NASA CR-174828, July, 1985.
- [10] Dorny, D. J., and Davis, R. L., "Numerical Simulation of Turbine "Hot Spot" Alleviation Using film Cooling", AIAA Paper 92-3309, 1993.
- [11] Garg, V. K., and Gaugler, R. E., "Heat Transfer in Film-Cooled Turbine Blades", ASME Paper 93-GT-81, 1993.
- [12] Zhou, J., Salcudean, M., and Gartshore, I., "Prediction of Film Cooling by Discrete-Hole Injection", ASME Paper 93-GT-75, 1993.
- [13] Leylek, . H., and Zerkle, J. H., "Discrete-Jet film cooling: A Comparison of Comptational Results with Experiments", ASME Paper 93-GT-207, 1993.
- [14] Pietrzyk, J. R., Bogard, D. G., and Crawford, M. E., "Hydrodynamic Measurements of Jets in Crossflow for Gas Turbine Film Cooling Applications", ASME Journal of Turbomachinery, Volume 111, pages 139-145.
- [15] Arnone, Andrea, *Notes on the Use of the TRAF Codes*. Department of Energy Engineering, University of Florence, and Institute for Computational Mechanics in Propulsion, NASA Lewis Research Center, November, 1992.
- [16] White, F. M., "Viscous Fluid Flow", McGraw-Hill Book Company, New York, New York, 1974.
- [17] Ameri, A. A., and Arnone, A., "Three Dimensional Navier-Stokes Analysis of Turbine Passage Heat Transfer", AIAA Paper AIAA-91-2241, 1991.
- [18] Ameri, A. A., and Arnone, A., "Navier-Stokes Turbine Heat Transfer Predictions Using Two-Equation Turbulence Closures", AIAA Paper 92-3067, 1992.

- [19] Garg, V. K., and Gaugler, R. E., "Heat Transfer in Film-Cooled Turbine Blades", ASME Paper 93-GT-81, 1993.
- [20] Kim, D. H., Lee, J. S., Kim, C. J., and Lee, D., "A Full Navier-Stokes Analysis of Flow and Heat Transfer in Steady Two-Dimensional Transonic Cascades", ASME Paper 93-GT-80, 1993.
- [21] J. Steinbrenner et. al., *The Gridgen 3D Multiple Block Grid Generation System*. Final Report WRDC-TR-90-3022, 1990
- [22] Hall, E. J. and Delaney, R. A., "Investigation of Advanced Counterrotation Blade Configuration Concepts for High Speed Turboprop Systems: Task V - Counterrotation Ducted Propfan Analysis, Final Report", NASA CR 187126, NASA Contract NAS3-25270, 1992.
- [23] Baldwin, B. S., and Lomax, H. "Thin Layer Approximation and Algebraic Model for Separated Turbulent Flows", AIAA Paper 78-257, 1978.
- [24] Barber, T., Choi, D., Delaney, R., Hall, E., and McNulty, G., "Preliminary Findings in Certification of ADPAC", AIAA Paper 94-2240, June, 1994.
- [25] Hall, E. J. and Delaney, R. A., "Investigation of Advanced Counterrotation Blade Configuration Concepts for High Speed Turboprop Systems: Task II - Unsteady Ducted Propfan Analysis - Final Report", NASA CR 187106, NASA Contract NAS3-25270, 1992.
- [26] Hall, E. J. and Delaney, R. A., "Investigation of Advanced Counterrotation Blade Configuration Concepts for High Speed Turboprop Systems: Task II - Unsteady Ducted Propfan Analysis - Computer Program User's Manual", NASA CR 187105, NASA Contract NAS3-25270, 1992.
- [27] Hall, E. J. and Delaney, R. A., "Investigation of Advanced Counterrotation Blade Configuration Concepts for High Speed Turboprop Systems: Task V - Counterrotation Ducted Propfan Analysis, Computer Program Users Manual", NASA CR 187125, NASA Contract NAS3-25270, 1992.

- [28] Hall, E. J., Topp, D. A., Heidegger, N. J., and Delaney, R. A., "Investigation of Advanced Counterrotation Blade Configuration Concepts for High Speed Turboprop Systems: Task VIII - Cooling Flow/Heat Transfer Analysis, Computer Program Users Manual", NASA CR-195360, NASA Contract NAS3-25270, 1994.
- [29] Martinelli, L., "Calculation of Viscous Flows with a Multigrid Method", Ph. D. Dissertation, MAE Department, Princeton University, 1987.
- [30] Hall, E. J., Delaney, R. A., and Bettner, J. L., "Investigation of Advanced Counterrotation Blade Configuration Concepts for High Speed Turboprop Systems: Task I - Ducted Propfan Analysis", NASA CR 185217, NASA Contract NAS3-25270, 1990.
- [31] Whipple, D., "BDX-Binary Data Exchange Preliminary Information", NASA-Lewis Research Center, 1989.
- [32] Walatka, P. P., and Buning, P. G., "PLOT3D User's Manual", rough draft for NASA TM, 1988.
- [33] Plessel, Todd, "SURF User's Guide", NASA Ames Research Center, 1988.
- [34] Walatka, P. P., and Buning, P. G., "FAST", NASA Ames Research Center, 1990.
- [35] Anderson, D. A., Tannehill, J. C., and Pletcher, R. H. , "Computational Fluid Mechanics and Heat Transfer", McGraw-Hill, New York, New York, 1984.
- [36] Hung, C. M., and Kordulla, W., "A Time-Split Finite Volume Algorithm for Three-Dimensional Flow-Field Simulation," AIAA Paper 83-1957, 1983.
- [37] Jameson, A., Schmidt, W., and Turkel, E., "Numerical Solutions of the Euler Equations by Finite Volume Methods Using Runge-Kutta Time-Stepping Schemes," AIAA Paper 81-1259, 1981.

- [38] Radespiel, R., Rossow, C., and Swanson, R. C., "Efficient Cell Vertex Multigrid Scheme for the Three-Dimensional Navier-Stokes Equations", *AIAA Journal*, Vol. 28, No. 8, pp. 1464-1472, 1990.
- [39] Hollanders, H., Lerat, A., and Peyret, R., "Three-Dimensional Calculation of Transonic Viscous Flows by an Implicit Method," *AIAA Journal*, 23, pp. 1670-1678, 1985.
- [40] Jorgensen, P. C. E., and Chima, R. V., "An Unconditionally Stable Runge-Kutta Method for Unsteady Flows," NASA TM 101347, 1989.
- [41] Rao, K. V., and Delaney, R. A., 1990, "Investigation of Unsteady Flow Through a Transonic Turbine Stage: Part I- Analysis", AIAA Paper 90-2408.

Appendix A

Mark II Vane Cascade Mesh Generation and ADPAC08 Input File Listing

Mark II Vane Cascade *JERRYC* Mesh Generation *datajc* Input File
Mesh Dependence Study Mesh #5

```
*** file DATAJC ***

*-- rot --- gap---
   0.0   1.892833
*-- gal --- galf---- ga2 ---
   90.    90.    20.
*-- xin --- xout--- ispl ---
   0.5    1.0    1
*-- d0x --- dix --- dsn --- jfix-- istrss-- istrps--(r+c+r=1,r+c=2,r+r=3)
   .015   .015   0.02   6    1    1
*-- rns --- rnse ---
   3.     1.
*-- nw  --- nss --- nps --- nin-- ny --- inl ---
   64    128    64    16    16    2
*-- omega --- dampb --- dampe --- itmax -
```

```
.01      .5      1.      500
*- ilet  -* (read from file=1)
  0
*- iwake -- xwake -- ywake --
  1      1.      1.
*- xshock *- n1 ----*
  .45    44
*- iannu --(0=prismatic, 1=annular)
  0
```

**Mark II Vane Cascade *JERRYC* Mesh Generation *airfoil.dat* Input
File
Mesh Dependence Study Mesh #5**

2.6986

38

0.0000000E+00	4.289100
7.7000000E-03	4.376600
3.0400001E-02	4.461500
6.7500003E-02	4.541100
0.1179000	4.613100
0.1800000	4.675200
0.2520000	4.725600
0.3316000	4.762700
0.4059000	4.784300
0.5514000	4.797000
0.7490000	4.766400
0.9285000	4.677300
1.073200	4.537900
1.173700	4.363500
1.256800	4.180100
1.337700	3.995700
1.417100	3.810800
1.495100	3.625300
1.571600	3.439200
1.646600	3.252600
1.720000	3.065600
1.792000	2.878000
1.862500	2.690000
1.931600	2.501500
1.999100	2.312600
2.065200	2.123200
2.129900	1.933600
2.193000	1.743400
2.254700	1.552900
2.315000	1.362100

2.373800	1.170900
2.431100	0.9794000
2.487000	0.7876000
2.541500	0.5956000
2.594500	0.4033000
2.646100	0.2108000
2.696200	1.8400000E-02
2.697300	-1.2800000E-02

41

0.0000000E+00	4.289100
7.7000000E-03	4.201600
3.0400001E-02	4.116700
6.7500003E-02	4.037100
0.1179000	3.965100
0.1800000	3.903000
0.2655000	3.845100
0.4019000	3.758100
0.5274000	3.653900
0.6432000	3.539000
0.7515000	3.417000
0.8538000	3.289000
0.9511000	3.159000
1.044400	3.025100
1.134200	2.888900
1.221100	2.750900
1.305400	2.611300
1.387400	2.470400
1.467500	2.328500
1.545600	2.185500
1.622100	2.041700
1.697000	1.897100
1.770100	1.751900
1.842400	1.606000
1.913100	1.459700
1.982600	1.312800
2.050800	1.165300
2.117800	1.017500

2.183700	0.8693000
2.248500	0.7207000
2.312100	0.5717000
2.374600	0.4224000
2.436000	0.2727000
2.496400	0.1228000
2.555600	-2.7000001E-02
2.572200	-5.2299999E-02
2.599200	-6.9499999E-02
2.630900	-7.3700003E-02
2.661500	-6.4099997E-02
2.685100	-4.2399999E-02
2.697300	-1.2800000E-02

0.5 2.0 1.0

Mark II Vane Cascade ADPAC08 Standard Input File
(Transitional Flow)
Mesh Dependence Study Mesh #5

ADPAC Input File Generated by Ed Hall

JOB TITLE

Planar 2-D Mark II Cascade Mesh #5
Cartesian 2-d Geometry
RUN 15, UNCOOLED - MACH=0.89 - Re=1.55E6
Tu=8.3%, Tw/Tg=0.70

INPUT DATA

VARNAME	= VARIABLE VALUE	COMMENT
CASENAME	= mesh5	This is the Case Name
FTOTSM	= 1.0	Multigrid Smoothing (0-off, 1-on)
EPSTOT	= 0.30	Global multigrid smoothing coefficient
FCART	= 1.0	Cartesian Trigger (0-cylindrical, 1-Cartesian)
RMACH	= 0.200000	Initial Flow Mach Number (Axial)
FINVVI	= 1.000000	Viscous Flow Trigger (0-inviscid, 1-viscous)
GAMMA	= 1.400000	Specific Heat Ratio
PREF	= 5519.52	Reference Pressure (lbs-f/ft**2)
TREF	= 1389.000	Reference Temperature (deg R)
RGAS	= 1716.260000	Gas Constant
DIAM	= 0.224883	Reference Length - Mark II 2.6986 inches
EPSX	= 1.000000	Residual Smoothing Coefficient (X)
EPSY	= 1.000000	Residual Smoothing Coefficient (Y)
EPSZ	= 1.000000	Residual Smoothing Coefficient (Z)
VIS2	= 0.500000	2nd order damping coefficient
VIS4	= 0.015625	4th order damping coefficient
CFL	= -5.000000	Time Step Multiplier (-, steady state)
FNCMAX	= 300.000000	Number of fine mesh iterations

FTIMEI	=	1.000000	Iteration Interval between time step update
FTURBI	=	1.000000	Iteration Interval between turbulence update
FTURBF	=	350.000000	Iteration number to freeze turbulence model
FTURBB	=	1.000000	Iteration number to begin turbulence model
PRNO	=	0.690000	Prandtl Number
PRNO	=	0.900000	Turbulent Prandtl Number
FSOLVE	=	1.000000	Solution Type (0-4stage,1-4stage w/smooth)
FVTSFAC	=	2.5	Viscous time step multiplier for stability
FFILT	=	1.000000	Dissipation Trigger (0-off,1-on)
FRESID	=	1.000000	Rseidual Smoothing Trigger (0-off,1-on)
FREST	=	0.000000	Solution Restart Trigger (0-cold start,1-restart)
FMULTI	=	3.000000	Number of Multigrid Levels (1-no multigrid)
FSUBIT	=	3.000000	Number of multigrid subiterations
FFULMG	=	1.000000	Full Multigrid Trigger (0-off,1-on)
FCOAG1	=	3.000000	Full multigrid starting mesh level
FCOAG2	=	2.000000	Full multigrid ending mesh level
FITFMG	=	100.000000	Number of full mutligrid iterations
CMUTSS	=	14.0	Suction surface Baldwin-Lomax transition parameter
CMUTPS	=	14.0	Pressure surface Baldwin-Lomax transitionparameter
XTRANS	=	0.5	Suction surface geometric transition parameter
XTRANPS	=	0.0	Pressure surface geometric transition parameter
FTURBCHT(1)	=	1.00	C-Grid Turbulence model trigger
FWALLF	=	0.0	Wall Function Trigger (0-off, 1-on)
RPM(1)	=	0.000000	Rotational Speed (=0.0 for vane)

Mark II Vane Cascade ADPAC08 Boundary Data File
(Transitional Flow)
Mesh Dependence Study Mesh #5

```

#
# Created by hand by Ed Hall
#
# RUN 4321 OF THE MARK II VANE
# UNCOOLED - MACH=0.89 - Re=1.55E6
# Tu =8.3%, Tw/Tg=0.70
#
#-----
#
#----> Patch the periodic boundary for the 2-d grid
#
PATCH 1 1 J J M M I J 65 65 1 185 1 2 385 201 1 2
PATCH 1 1 J J M M I J 65 65 201 385 1 2 185 1 1 2
#
#----> Now set the blade surfaces
#
SS2DVI 1 1 J J P P S S 1 1 129 321 1 2 129 321 1 2
RPMLOC TWALL
0.0 0.70
#
#----> Now set the inlet boundary
#
INLETG 1 1 J J M M S S 65 65 185 201 1 2 185 201 1 2
PTOT TTOT
1.0 1.0
#
#----> Now set the lower exit boundary
#
EXITG 1 1 I I P P S S 1 1 1 65 1 2 1 65 1 2
PEXIT
0.59787
#

```

#---> Now set the upper exit boundary

#

EXITG 1 1 I I M M S S 385 385 1 65 1 2 1 65 1 2

PEXIT

0.59787

#

#---> Now set the lower wake cut

#

TRAF 1 1 J J P P S S 1 1 1 129 1 2 321 385 1 2

#

#---> Now set the upper wake cut

#

TRAF 1 1 J J P P S S 1 1 321 385 1 2 1 129 1 2

#

ENDDATA

Appendix B

C3X Vane Cascade Mesh Generation and ADPAC08 Input File Listing

C3X Vane Cascade *JERRYC* Mesh Generation *datajc* Input File
Mesh Dependence Study Mesh #5

*** file DATAJC ***

```
*-- rot --- gap--*
  0.0   1.50615
*-- gal --- galf--- ga2 ---*
  90.   90.   15.
*-- xin --- xout--- ispl ---*
  0.5   1.0   1
*-- d0x --- d1x --- dsn --- jfix-- istrss-- istrps--(r+c+r=1,r+c=2,r+r=3)
  .010  .010  0.010  12   1   1
*-- rnsr---rnse ---*
  3.    1.
*-- nr --- nss --- nps --- nin-- ny --- inl ---*
  48    144   72    16   24   2
*-- omega -- dampb -- dampe -- itmax -
```

169

PRECEDING PAGE BLANK NOT FILMED

PAGE 168 INTENTIONALLY BLANK

```
.01      .5      1.      500
*- ilet  -* (read from file=1)
  0
*- iwake -- xwake -- ywake --
  1      1.      1.
*- xshock *- n1 ----*
  .45    44
*- iannu --(0=prismatic, 1=annular)
  0
```

**C3X Vane Cascade JERRYC Mesh Generation *airfoil.dat* Input File
Mesh Dependence Study Mesh #5**

0.0

184

-0.8503435	-0.2113152E-01	0.4768372E-06
-0.8503269	-0.1876569E-01	-0.2384186E-06
-0.8502638	-0.1639986E-01	0.2384186E-06
-0.8501548	-0.1403677E-01	0.2384186E-06
-0.8500136	-0.1167536E-01	0.2384186E-06
-0.8498576	-0.9314775E-02	0.0000000E+00
-0.8497047	-0.6953716E-02	0.2384186E-06
-0.8495624	-0.4592896E-02	0.2384186E-06
-0.8494225	-0.2231121E-02	0.4768372E-06
-0.8492831	0.1296997E-03	0.0000000E+00
-0.8491411	0.2491713E-02	0.2384186E-06
-0.8489990	0.4853010E-02	-0.2384186E-06
-0.8487656	0.7342100E-02	0.4768372E-06
-0.8484385	0.1080787E-01	0.0000000E+00
-0.8479946	0.1553774E-01	0.7152557E-06
-0.8474393	0.2181184E-01	0.2384186E-06
-0.8466598	0.2980661E-01	0.4768372E-06
-0.8454475	0.3950083E-01	0.2384186E-06
-0.8440130	0.5062366E-01	0.2384186E-06
-0.8420173	0.6248617E-01	0.0000000E+00
-0.8395965	0.7428372E-01	0.2384186E-06
-0.8371067	0.8521318E-01	0.2384186E-06
-0.8346531	0.9467101E-01	0.0000000E+00
-0.8326366	0.1024483	0.2384186E-06
-0.8310156	0.1085312	0.7152557E-06
-0.8297770	0.1131177	0.2384186E-06
-0.8288705	0.1164799	0.0000000E+00
-0.8282200	0.1188939	0.2384186E-06
-0.8275299	0.1214904	0.0000000E+00
-0.8268430	0.1240888	0.2384186E-06
-0.8261462	0.1266727	0.9536743E-06

-0.8253567	0.1292219	0.4768372E-06
-0.8244731	0.1317540	0.7152557E-06
-0.8235750	0.1342809	0.2384186E-06
-0.8226759	0.1368090	0.0000000E+00
-0.8217750	0.1393346	0.2384186E-06
-0.8208760	0.1418602	0.4768372E-06
-0.8199744	0.1443849	0.2384186E-06
-0.8190663	0.1469064	0.0000000E+00
-0.8181396	0.1494229	0.4768372E-06
-0.8171858	0.1519289	0.4768372E-06
-0.8161595	0.1543405	0.0000000E+00
-0.8150036	0.1566857	0.0000000E+00
-0.8138143	0.1590955	0.0000000E+00
-0.8127274	0.1612952	0.0000000E+00
-0.8115568	0.1636613	0.0000000E+00
-0.8102946	0.1662092	0.0000000E+00
-0.8089364	0.1689471	0.0000000E+00
-0.8074714	0.1718958	0.0000000E+00
-0.8058913	0.1750709	0.0000000E+00
-0.8041861	0.1784912	0.0000000E+00
-0.8023457	0.1821758	0.0000000E+00
-0.8003641	0.1861349	0.0000000E+00
-0.7982350	0.1903795	0.0000000E+00
-0.7959470	0.1949302	0.0000000E+00
-0.7934872	0.1998105	0.0000000E+00
-0.7908448	0.2050393	0.0000000E+00
-0.7880097	0.2106337	0.0000000E+00
-0.7849640	0.2166257	0.0000000E+00
-0.7816887	0.2230492	0.0000000E+00
-0.7781715	0.2299239	0.0000000E+00
-0.7744005	0.2372685	0.0000000E+00
-0.7703412	0.2451449	0.0000000E+00
-0.7659765	0.2535804	0.0000000E+00
-0.7613040	0.2625730	0.0000000E+00
-0.7562451	0.2722666	0.0000000E+00
-0.7508348	0.2825855	0.0000000E+00
-0.7449768	0.2937043	0.0000000E+00

-0.7386930	0.3055711	0.0000000E+00
-0.7318816	0.3183663	0.0000000E+00
-0.7245727	0.3320211	0.0000000E+00
-0.7166013	0.3468294	0.0000000E+00
-0.7080284	0.3626626	0.0000000E+00
-0.6986908	0.3798057	0.0000000E+00
-0.6886111	0.3976789	0.0000000E+00
-0.6777089	0.4155577	0.0000000E+00
-0.6659530	0.4335242	0.0000000E+00
-0.6532367	0.4517534	0.0000000E+00
-0.6395168	0.4702970	0.0000000E+00
-0.6245990	0.4893830	0.0000000E+00
-0.6085304	0.5089085	0.0000000E+00
-0.5910546	0.5291324	0.0000000E+00
-0.5721794	0.5499824	0.0000000E+00
-0.5517677	0.5715471	0.0000000E+00
-0.5296940	0.5932899	0.0000000E+00
-0.5061355	0.6141747	0.0000000E+00
-0.4808524	0.6345311	0.0000000E+00
-0.4538445	0.6543210	0.0000000E+00
-0.4251218	0.6731620	0.0000000E+00
-0.3945598	0.6907467	0.0000000E+00
-0.3622622	0.7066501	0.0000000E+00
-0.3284237	0.7204539	0.0000000E+00
-0.2931721	0.7317632	0.0000000E+00
-0.2567927	0.7402783	0.0000000E+00
-0.2195242	0.7460162	0.0000000E+00
-0.1815696	0.7490003	0.0000000E+00
-0.1431976	0.7492337	0.0000000E+00
-0.1047192	0.7468412	0.0000000E+00
-0.6644078E-01	0.7419178	0.0000000E+00
-0.2867779E-01	0.7346342	0.0000000E+00
0.8365643E-02	0.7250878	0.0000000E+00
0.4448613E-01	0.7133373	0.0000000E+00
0.7947456E-01	0.6996126	0.0000000E+00
0.1132675	0.6841420	0.0000000E+00
0.1457146	0.6671873	0.0000000E+00

0.1765886	0.6490904	0.0000000E+00
0.2059018	0.6301268	0.0000000E+00
0.2336831	0.6105611	0.0000000E+00
0.2597292	0.5908181	0.0000000E+00
0.2840771	0.5711082	0.0000000E+00
0.3073878	0.5510698	0.0000000E+00
0.3398996	0.5211544	0.0000000E+00
0.3717093	0.4896633	0.0000000E+00
0.4024529	0.4571042	0.0000000E+00
0.4333721	0.4221632	0.0000000E+00
0.4642093	0.3850020	0.0000000E+00
0.4939390	0.3469336	0.0000000E+00
0.5222397	0.3086895	0.0000000E+00
0.5494987	0.2699772	0.0000000E+00
0.5760936	0.2304206	0.0000000E+00
0.6018567	0.1905146	0.0000000E+00
0.6267536	0.1505387	0.0000000E+00
0.6510149	0.1102040	0.0000000E+00
0.6749514	0.6901693E-01	0.0000000E+00
0.6986184	0.2686283E-01	0.0000000E+00
0.7218922	-0.1601974E-01	0.0000000E+00
0.7446451	-0.5929260E-01	0.0000000E+00
0.7668765	-0.1028507	0.0000000E+00
0.7886448	-0.1467848	0.0000000E+00
0.8100320	-0.1912252	0.0000000E+00
0.8311171	-0.2362971	0.0000000E+00
0.8519033	-0.2819202	0.0000000E+00
0.8723653	-0.3279585	0.0000000E+00
0.8924960	-0.3743130	0.0000000E+00
0.9123098	-0.4209788	0.0000000E+00
0.9318312	-0.4678490	0.0000000E+00
0.9510201	-0.5146129	0.0000000E+00
0.9698415	-0.5610776	0.0000000E+00
0.9884402	-0.6075802	0.0000000E+00
1.006759	-0.6538965	0.0000000E+00
1.026890	-0.7052840	0.0000000E+00
1.048748	-0.7615448	0.0000000E+00

1.072436	-0.8230521	0.0000000E+00
1.098062	-0.8902131	0.0000000E+00
1.125662	-0.9632655	0.0000000E+00
1.155252	-1.042415	0.0000000E+00
1.186830	-1.127822	0.0000000E+00
1.220361	-1.219579	0.0000000E+00
1.255785	-1.317671	0.0000000E+00
1.293039	-1.422048	0.0000000E+00
1.331995	-1.532499	0.0000000E+00
1.372506	-1.648620	0.0000000E+00
1.414382	-1.769919	0.0000000E+00
1.457400	-1.895753	0.0000000E+00
1.501305	-2.025173	0.0000000E+00
1.545799	-2.157010	0.0000000E+00
1.590574	-2.290617	0.0000000E+00
1.635327	-2.425135	0.0000000E+00
1.679668	-2.559144	0.0000000E+00
1.723220	-2.691577	0.0000000E+00
1.765681	-2.821604	0.0000000E+00
1.806753	-2.948484	0.0000000E+00
1.846124	-3.071684	0.0000000E+00
1.883580	-3.191852	0.1903580E-05
1.918974	-3.305335	0.1358246E-05
1.952179	-3.413130	0.1653119E-05
1.983041	-3.514931	0.1539569E-05
2.011562	-3.610518	0.1184508E-05
2.037753	-3.699794	0.1101842E-05
2.061696	-3.782752	0.1288405E-05
2.083477	-3.859481	0.2147401E-05
2.103197	-3.930142	0.8439010E-06
2.120972	-3.994961	0.1094460E-05
2.136953	-4.054197	0.3223423E-06
2.151295	-4.108145	0.1054545E-05
2.164153	-4.157122	0.6835817E-06
2.175800	-4.201425	0.7147956E-06
2.186393	-4.241382	0.6715061E-06
2.195822	-4.277388	0.4266357E-06

2.204079	-4.309798	0.7220024E-06
2.211196	-4.338942	0.2384186E-06
2.217276	-4.365115	0.0000000E+00
2.222741	-4.390125	0.7152557E-06
2.225596	-4.414248	0.4768372E-06
202		
-0.8503435	-2.1131519E-02	
-0.8503120	-2.3498060E-02	
-0.8502332	-2.5861019E-02	
-0.8501152	-2.8223280E-02	
-0.8499801	-3.0586360E-02	
-0.8498478	-3.2948490E-02	
-0.8497195	-3.5444502E-02	
-0.8495367	-3.8960218E-02	
-0.8492448	-4.3802500E-02	
-0.8487291	-5.0277948E-02	
-0.8479056	-5.8607101E-02	
-0.8468673	-6.8817973E-02	
-0.8454297	-8.0578327E-02	
-0.8436325	-9.3217850E-02	
-0.8415182	-0.1058046	
-0.8391119	-0.1174107	
-0.8368247	-0.1274161	
-0.8347721	-0.1355352	
-0.8330539	-0.1417917	
-0.8317131	-0.1464520	
-0.8307285	-0.1498353	
-0.8300338	-0.1522384	
-0.8291938	-0.1549525	
-0.8283594	-0.1576681	
-0.8275394	-0.1603897	
-0.8267182	-0.1631095	
-0.8258651	-0.1658202	
-0.8249546	-0.1685101	
-0.8239882	-0.1711822	
-0.8229856	-0.1738410	
-0.8219669	-0.1764941	

-0.8209407	-0.1791449
-0.8199121	-0.1817942
-0.8188763	-0.1844387
-0.8178322	-0.1870804
-0.8167819	-0.1897197
-0.8157284	-0.1923590
-0.8146734	-0.1949978
-0.8136958	-0.1972985
-0.8123481	-0.2004690
-0.8105330	-0.2047458
-0.8081439	-0.2103505
-0.8050418	-0.2173948
-0.8009601	-0.2257309
-0.7962791	-0.2352276
-0.7908976	-0.2451839
-0.7852581	-0.2550120
-0.7797520	-0.2640390
-0.7744857	-0.2716813
-0.7701128	-0.2780175
-0.7666214	-0.2830057
-0.7638197	-0.2867126
-0.7617322	-0.2894535
-0.7602206	-0.2914448
-0.7585067	-0.2937107
-0.7567942	-0.2959762
-0.7550800	-0.2982421
-0.7533655	-0.3005061
-0.7516427	-0.3027644
-0.7499099	-0.3050151
-0.7481757	-0.3072653
-0.7464430	-0.3095150
-0.7447093	-0.3117642
-0.7429744	-0.3140144
-0.7412415	-0.3162646
-0.7395080	-0.3185143
-0.7377408	-0.3207498
-0.7358676	-0.3229008

-0.7339766	-0.3250065
-0.7320926	-0.3271198
-0.7304083	-0.3289661
-0.7280506	-0.3315544
-0.7248378	-0.3351240
-0.7204874	-0.3398108
-0.7146188	-0.3455434
-0.7074124	-0.3525052
-0.6989050	-0.3602829
-0.6895660	-0.3684521
-0.6799896	-0.3763223
-0.6709285	-0.3834567
-0.6629969	-0.3895764
-0.6562784	-0.3942823
-0.6510340	-0.3979454
-0.6470966	-0.4006929
-0.6442261	-0.4026971
-0.6421758	-0.4041271
-0.6399193	-0.4055786
-0.6376626	-0.4070296
-0.6354061	-0.4084806
-0.6331494	-0.4099312
-0.6308925	-0.4113827
-0.6286364	-0.4128332
-0.6263793	-0.4142842
-0.6241224	-0.4157352
-0.6218661	-0.4171858
-0.6196648	-0.4187179
-0.6175027	-0.4203072
-0.6153400	-0.4218950
-0.6131785	-0.4234834
-0.6110156	-0.4250722
-0.6088538	-0.4266605
-0.6066916	-0.4282494
-0.6056080	-0.4293237
-0.6038585	-0.4306355
-0.6019473	-0.4320683

-0.5998585	-0.4336343
-0.5975757	-0.4353456
-0.5950822	-0.4372158
-0.5923574	-0.4392586
-0.5893811	-0.4414897
-0.5861299	-0.4439278
-0.5825803	-0.4465885
-0.5787048	-0.4494953
-0.5744739	-0.4526682
-0.5698566	-0.4561310
-0.5648162	-0.4599109
-0.5593147	-0.4640346
-0.5533108	-0.4685330
-0.5467589	-0.4734387
-0.5396174	-0.4787865
-0.5318441	-0.4846158
-0.5233974	-0.4909716
-0.5142312	-0.4979639
-0.5042839	-0.5056334
-0.4934834	-0.5140028
-0.4817472	-0.5231171
-0.4689895	-0.5330257
-0.4551237	-0.5437927
-0.4400508	-0.5554843
-0.4236861	-0.5681729
-0.4059761	-0.5819335
-0.3868835	-0.5969253
-0.3663556	-0.6134224
-0.3443651	-0.6315088
-0.3206997	-0.6512036
-0.2951511	-0.6724424
-0.2676010	-0.6953273
-0.2381136	-0.7202485
-0.2068570	-0.7475548
-0.1734368	-0.7770576
-0.1376376	-0.8087232
-9.9896006E-02	-0.8433228

-6.0000300E-02	-0.8807602
-1.7720340E-02	-0.9209964
2.6771899E-02	-0.9643795
7.3483348E-02	-1.011038
0.1223395	-1.061148
0.1733397	-1.114783
0.2262687	-1.172173
0.2814841	-1.232976
0.3383115	-1.297744
0.3967873	-1.366327
0.4568994	-1.438574
0.5179356	-1.514847
0.5804461	-1.594444
0.6432238	-1.677964
0.7070484	-1.764452
0.7706779	-1.854386
0.8346933	-1.946893
0.8982663	-2.042040
0.9614595	-2.139250
1.023867	-2.238230
1.085380	-2.338490
1.145680	-2.439640
1.204602	-2.541214
1.261995	-2.642740
1.317577	-2.743837
1.371500	-2.843910
1.423267	-2.942749
1.473176	-3.039757
1.520778	-3.134778
1.566484	-3.227253
1.609871	-3.317096
1.651270	-3.403901
1.690292	-3.487653
1.727319	-3.568028
1.762216	-3.644975
1.794956	-3.718459
1.825979	-3.788257

1.854649	-3.854667
1.881676	-3.917423
1.906978	-3.976644
1.930421	-4.032480
1.952413	-4.084885
1.972843	-4.134038
1.991634	-4.180120
2.009170	-4.223130
2.025508	-4.263210
2.040530	-4.300579
2.054365	-4.335348
2.067202	-4.367614
2.079095	-4.397523
2.090108	-4.425216
2.101564	-4.450262
2.118183	-4.469349
2.139040	-4.480016
2.160339	-4.482932
2.179970	-4.479840
2.197673	-4.470520
2.212416	-4.455792
2.222278	-4.436616
2.225596	-4.414248

0.5 0.0 36.6803

**C3X Vane Cascade ADPAC08 Standard Input File (Transitional
Flow)
Mesh Dependence Study Mesh #5**

ADPAC Input File Generated by Ed Hall

JOB TITLE

Planar 2-D Mark II Cascade mesh TRAF2D Mesh
Cartesian 2-d Geometry
RUN 15, UNCOOLED - MACH=0.89 - Re=1.55E6
Tu=8.3%, Tw/Tg=0.70

INPUT DATA

VARNAME	= VARIABLE VALUE	COMMENT
CASENAME	= mesh5	This is the Case Name
FTOTSM	= 1.0	Multigrid Smoothing (0-off, 1-on)
EPSTOT	= 0.30	Global multigrid smoothing coefficient
FCART	= 1.0	Cartesian Trigger (0-cylindrical, 1-Cartesian)
RMACH	= 0.200000	Initial Flow Mach Number (Axial)
FINVVI	= 1.000000	Viscous Flow Trigger (0-inviscid, 1-viscous)
GAMMA	= 1.365000	Specific Heat Ratio
PREF	= 6672.960	Inlet Total Pressure (psfa)
TREF	= 1415.000	Inlet Total Temperature (deg R)
RGAS	= 1716.260000	Gas Constant
DIAM	= 0.256400	Scaling Factor
EPSX	= 1.000000	Residual Smoothing Coefficient (X)
EPSY	= 1.000000	Residual Smoothing Coefficient (Y)
EPSZ	= 1.000000	Residual Smoothing Coefficient (Z)
VIS2	= 0.500000	2nd order damping coefficient
VIS4	= 0.015625	4th order damping coefficient
CFL	= -5.000000	Time Step Multiplier (-, steady state, +, time- dependent)
FNCMAX	= 300.000000	Number of fine mesh iterations

FTIMEI	=	1.000000	Iteration Interval between time step update
FTURBI	=	1.000000	Iteration Interval between turbulence update
FTURBF	=	9999.000000	Iteration number to freeze turbulence model
FTURBB	=	1.000000	Iteration number to begin turbulence model
PRNO	=	0.685000	Prandtl Number
PRTNO	=	0.900000	Turbulent Prandtl Number
FSOLVE	=	1.000000	Solution Type (0-4stage,1-4stage w/smooth)
FVTSFAC	=	2.5	Viscous time step multiplier for stability
FFILT	=	1.000000	Dissipation Trigger (0-off,1-on)
FRESID	=	1.000000	Rseidual Smoothing Trigger (0-off,1-on)
FREST	=	0.000000	Solution Restart Trigger (0-cold start,1-restart)
FMULTI	=	3.000000	Number of Multigrid Levels (1-no multigrid)
FSUBIT	=	3.000000	Number of multigri subiterations
FFULMG	=	1.000000	Full Multigrid Trigger (0-off,1-on)
FCOAG1	=	3.000000	Full multigrid starting mesh level
FCOAG2	=	2.000000	Full multigrid ending mesh level
FITFMG	=	100.000000	Number of full mutligrid iterations
CMUTSS	=	14.0	Suction surface Mayle transition parameter
CMUTPS	=	14.0	Pressure surface Mayle transition parameter
XTRANS	=	0.8	Suction surface geometric transition parameter
XTRANPS	=	0.0	Pressure surface geometric transition parameter
FTURBCHT(1)	=	1.00	C-Grid Turbulence model trigger
FWALLF	=	0.0	Wall Function Trigger (0-off, 1-on)
RPM(1)	=	0.000000	Rotational Speed (=0.0 for vane)

**C3X Vane Cascade ADPAC08 Boundary Data File (Transitional
Flow)
Mesh Dependence Study Mesh #5**

```

#
# Created by hand by Ed Hall
# March 30, 1993 @ 2:45 P.M.
# Revised by Scott McNulty
# 12/21/93
#
# Allison C3X Turbine Vane - Run 4411 with 385x97 C-Mesh
# Uncooled - Mach2=0.90 - Re=2.0E6
#
#-----
#---> Patch the periodic boundary for the 2-d grid
#
PATCH 1 1 J J M M I J 97 97 1 185 1 2 385 201 1 2
PATCH 1 1 J J M M I J 97 97 201 385 1 2 185 1 1 2
#
#---> Now set the blade surfaces
# Use the arc-length averaged Wall Temperature instead of the actual
# surface temperature distribution
SS2DVI 1 1 J J P P S S 1 1 121 337 1 2 121 337 1 2
RPMLOC TWALL
0.0 0.73
#
#---> Now set the inlet boundary
#
INLETG 1 1 J J M M S S 97 97 185 201 1 2 185 201 1 2
PTOT TTOT
1.0 1.0
#
#---> Now set the lower exit boundary
#
EXITG 1 1 I I P P S S 1 1 1 97 1 2 1 97 1 2
PEXIT

```

0.59768

#

#---> Now set the upper exit boundary

#

EXITG 1 1 I I M M S S 385 385 1 97 1 2 1 97 1 2

PEXIT

0.59768

#

#---> Now set the lower wake cut

#

TRAF 1 1 J J P P S S 1 1 1 121 1 2 337 385 1 2

#

#---> Now set the upper wake cut

#

TRAF 1 1 J J P P S S 1 1 337 385 1 2 1 121 1 2

#

ENDDATA



REPORT DOCUMENTATION PAGE

Form Approved
OMB No. 0704-0188

Public reporting burden for this collection of information is estimated to average 1 hour per response, including the time for reviewing instructions, searching existing data sources, gathering and maintaining the data needed, and completing and reviewing the collection of information. Send comments regarding this burden estimate or any other aspect of this collection of information, including suggestions for reducing this burden, to Washington Headquarters Services, Directorate for Information Operations and Reports, 1215 Jefferson Davis Highway, Suite 1204, Arlington, VA 22202-4302, and to the Office of Management and Budget, Paperwork Reduction Project (0704-0188), Washington, DC 20503.

1. AGENCY USE ONLY (Leave blank)		2. REPORT DATE September 1994	3. REPORT TYPE AND DATES COVERED Final Contractor Report	
4. TITLE AND SUBTITLE Investigation of Advanced Counterrotation Blade Configuration Concepts for High Speed Turboprop Systems Task 8-Cooling Flow/Heat Transfer Analysis Final Report			5. FUNDING NUMBERS WU-538-03-11 C-NAS3-25270	
6. AUTHOR(S) E.J. Hall, D.A. Topp, N.J. Heidegger, and R.A. Delaney				
7. PERFORMING ORGANIZATION NAME(S) AND ADDRESS(ES) Allison Engine Company P.O. Box 420 Indianapolis, Indiana 46206-0420			8. PERFORMING ORGANIZATION REPORT NUMBER E-9024	
9. SPONSORING/MONITORING AGENCY NAME(S) AND ADDRESS(ES) National Aeronautics and Space Administration Lewis Research Center Cleveland, Ohio 44135-3191			10. SPONSORING/MONITORING AGENCY REPORT NUMBER NASA CR-195359	
11. SUPPLEMENTARY NOTES Project Manager, Christopher J. Miller, Propulsion Systems Division, organization code 2770, (216) 433-6179.				
12a. DISTRIBUTION/AVAILABILITY STATEMENT Unclassified - Unlimited Subject Categories 07 and 34			12b. DISTRIBUTION CODE	
13. ABSTRACT (Maximum 200 words) The focus of this task was to validate the ADPAC code for heat transfer calculations. To accomplish this goal, the ADPAC code was modified to allow for a Cartesian coordinate system capability and to add boundary conditions to handle spanwise periodicity and transpiration boundaries. The primary validation case was the film cooled C3X vane. The cooling hole modeling included both a porous region and grid in each discrete hold. Predictions for these models as well as a smooth wall compared well with the experimental data.				
14. SUBJECT TERMS Turbomachinery; Fan; Duct; Navier-Stokes; Multiple block; ADPAC			15. NUMBER OF PAGES 199	
			16. PRICE CODE A09	
17. SECURITY CLASSIFICATION OF REPORT Unclassified	18. SECURITY CLASSIFICATION OF THIS PAGE Unclassified	19. SECURITY CLASSIFICATION OF ABSTRACT Unclassified	20. LIMITATION OF ABSTRACT	

END DATE OCT 31, 1994

